THE ANISOTROPIC REFLECTIVITY TECHNIQUE

by

David C. Booth

(B.Sc., Univ. of Dundee, M.Sc., Univ. of Durham)

Thesis submitted for degree of Ph.D.

University of Edinburgh, Department of Geophysics

July 1982

I hereby declare that this thesis was composed by myself and that the work described in it is entirely my own unless explicitly stated otherwise.

ABSTRACT

The reflectivity technique for the calculation of synthetic seismograms from a point source in horizontally-layered isotropic structures is extended to allow anisotropic layers. The response of the reflection-zone is expressed in terms of wave displacements rather than wave potentials, which have not yet been defined for anisotropic propagation. Coupling between the sagittal and transverse components of wave-motion increases the number of plane-wave reflection and transmission coefficients which must be computed for each problem. These coefficients are computed by extending the iterative approach of Kennett (1974) to stratified anisotropic media.

The displacement spectra are expressed in terms of single integrals over horizontal slowness by an approximation which assumes neglible deviation of wave-energy from the sagittal plane, and thereby restricts the application of the technique to weakly anisotropic media. This approximation is also used in the calculation of travel-times in stratified anisotropic structures. In transversely isotropic structures, exact travel times can be calculated, and these are used to illustrate the effect of anisotropy in the processing of common-depth-point gathers.

Simple model structures are used to assess the feasibility of detecting and analysing upper-mantle anisotropy from anomalous body-wave arrivals. Anomalous arrivals from incident P-waves are unlikely to be detected. The use of split shear-waves is more promising, though shear-wave amplitudes are shown to be crucially dependent on the velocity contrasts at the anisotropic layer boundaries.

Wave-motion in a cracked channel bounded by thin fluid-filled fractures is also investigated, in an attempt to explain observations of distinctive shear-wave motion in a geothermal reservoir in terms of trapped channel waves. Observed non-linear P-wave motion and possible

mislocation of events can be explained by theoretical P-wave seismograms. It has not been possible to replicate the observed shear wavetrain with the present formulation of the anisotropic reflectivity method, which does not permit a buried source. However, channel waves generated by a source outside the cracked channel appear on the synthetic seismograms, and they are shown to depend on the existence of the fluid-filled cracks.

ACKNOWLEDGEMENTS

It is a pleasure to acknowledge the considerable debt of gratitude which I owe to my supervisor, Dr.Stuart Crampin. This thesis could never have been conceived without Stuart's energetic and painstaking research into seismic anisotropy over many years. It would certainly never have been completed without his continual encouragement and limitless enthusiasm, his constructive criticisms, and above all, his unfailing readiness to discuss problems. I consider myself very lucky to have had Stuart as a supervisor.

I am also indebted to Karl Fuchs, Brian Kennett, Rainer Kind, and Gerhard Müller, who have freely supplied me with their computer programs and advice on reflectivity theory. I thank Brian in particular for his hospitality during my visits to Cambridge and for his personal assistance in the operation of his computer programs.

I am very grateful for the opportunity which this thesis gives me to record my thanks to my colleagues at the Global Seismology Unit, Edinburgh for their assistance, advice, and good humour during the past eight years. In particular, Bob McGonigle helped me many times with programming in the course of my thesis, and liaisoned on my behalf with the Edinburgh Regional Computing Centre, whose staff have also been of great assistance. The Natural Environment Research Council has provided financial support during this research work, and its assistance is gratefully acknowledged.

Last, but certainly not least, I thank my wife Catherine for typing the major part of this thesis, and above all for cheering me up during the days when I thought it would never be completed. Finally, my apologies to my children, Jennifer and Alan, for many absent evenings.

CONTENTS

CHAPTER 1

INTRODUCTION

1.1 Causes and significance of seismic anisotropy

A seismically anisotropic material possesses some kind of directional alignment in its elastic properties. Anisotropy in the Earth may arise in several different ways (Todd, Simmons & Baldridge 1973), but in general it can be attributed to layering, preferred mineral orientation, or alignment of pores or cracks in the rock matrix. We shall describe these three principal mechanisms in greater detail.

Repeated sequences of thin layers can display the seismic velocity characteristics of the particular type of anisotropy known as transverse isotropy (Postma 1955, Backus 1962). This phenomenon will occur when measurements are made at wavelengths which are large compared to the layer thicknesses. However there appear to be no field observations of transverse isotropy which can be uniquely attributed to fine layering.

Preferred alignment of mineral grains may occur on a macroscopic or microscopic scale. The transverse isotropy displayed by certain types of sedimentary rock such as shales (Kaarsberg 1968) is an example of macroscopic alignment due to bedding in the presence of a lithostatic stress-field. On the microscopic scale, the anisotropy of many igneous rocks is caused by a preferred orientation of individual mineral crystals, particularly olivine. The most important mechanisms which produce preferred mineral orientations are crystal settling in magma chambers, and plastic flow and recrystallization in the presence of a tectonic stress-field. The dominant mechanism will depend on the ambient physical

conditions, particularly the temperature and strain-rate (Ave'Lallemant & Carter 1970). Ave'Lallemant & Carter show that upper-mantle anisotropy is most easily explained by the stress-induced recrystallisation of olivine crystals. Christensen (1982) has recently given an extensive bibliography of studies on the seismic velocities of rock samples.

The third possible cause of anisotropy is an aligned distribution of pores or cracks in a homogeneous rock. At the top of the crust these cracks may be large scale joints and fractures (Bamford & Nunn 1979). Large cracks will not exist deeper than a few kilometres due to the large confining pressures. However, at all depths in the crust there are microcracks in the rock grains and along their boundaries. These microcracks may differentially open or close, depending on the applied non-lithostatic stresses and the ambient pore-pressure, and thus display an alignment. Crack anisotropy will become less significant with increasing depth below the lower crust, due to the increasing confining pressure.

There are many potentially important applications for the analysis of anisotropy by wave propagation methods. In oil exploration work, optimum seismic reflection data processing may require that account be taken of the transversely isotropic properties of overlying sedimentary strata. Also, the study of upper mantle anisotropy could assist in establishing the tectonic history of the lithosphere (Crampin 1977b, Meissner & Flüh 1979). These examples will be discussed further in chapters 4 and 5 of this thesis.

The most important potential application for crack anisotropy studies is in the field of dilatancy and earthquake prediction. Dilatant rocks in the stressed region of an earthquake preparation zone will contain systems of aligned cracks, and thus the zone will be anisotropic (Crampin 1978, Crampin, Evans & Atkinson 1982). Wave propagation phenomena which are characteristic of anisotropy have already been observed in data from field

experiments in seismically active regions (Yegorkina, Rakitov, Garetovskaya & Yegorova 1977, Crampin et al.1980). In principle, analysis of the dilatancy-anisotropy offers a means of monitoring the density, distribution and saturation of the cracks, which are critical physical parameters associated with the eventual failure of the stressed region.

1.2 Synthetic seismograms

It will be necessary to obtain a full understanding of wave propagation in anisotropic media, if observed data is to be analysed and interpreted in terms of anisotropy in the earth. Wave propagation in anisotropic media is substantially different from propagation in isotropic media, and many anomalies of propagation may occur. The most obvious anomaly is a directional variation of the seismic velocities. However, the effects of seismic anisotropy are often subtle and difficult to detect on observed seismograms. A full investigation into the seismic effects of an anisotropic structure will almost invariably require the use of synthetic seismograms.

Synthetic seismograms for plane wave propagation in anisotropic media have been calculated by Keith & Crampin (1977c) and Crampin (1978). However, the most potentially useful seismic experiments involve the use of curved wavefronts from local or regional sources in studies of the crust and upper mantle. The group velocity and phase velocity vectors generally diverge in anisotropic media (Crampin 1977a) with the result that there are fundamental differences in behaviour between waves with plane and curved wavefronts (Crampin & McGonigle 1981).

Several techniques are available for obtaining solutions for the propagation of a curved wavefront in the form of synthetic seismograms. The most commonly-used techniques are the generalised ray or ray-

theoretical technique (Müller 1968a,b, 1970, Wiggins & Helmberger 1974), the asymptotic ray technique (Červený & Ravindra 1971, Hron & Kanasewich 1971, Hron, Kanasewich & Alpaslan 1974), and the reflectivity technique (Fuchs & Müller 1971). In its original formulation, the reflectivity technique yields an exact solution for a laterally homogeneous sequence of plane horizontal isotropic layers.

In the present work, we shall adapt the reflectivity technique so that we may obtain approximate expressions for the displacements of curved wavefronts through a structure consisting of plane horizontal anisotropic layers. It will be shown that the approximate expressions are valid for weakly anisotropic layered media at distances which are large when compared to the wavelength of the source field. The reflectivity technique is particularly suitable for extension to anisotropic media since it makes use of matrix formulations which have already been extended to anisotropic media by Crampin (1970) and Keith & Crampin (1977a,b).

1.3 An outline of the work in this thesis

In chapter 2 we review the application of the reflectivity technique to studies of wave propagation in plane-layered isotropic media, and we present the theory of the technique in a way which facilitates the extension of the technique to anisotropic media. The extension to anisotropic media is described in chapter 3. It involves the calculation of the plane wave displacement response of a multilayered anisotropic structure, in an iterative scheme which is based on that of Kennett (1974). The computational procedure which leads to the construction of the synthetic seismograms is described in detail.

When theoretical or observed seismograms are being interpreted, it is very useful to know the travel-times of the various arrivals which are

expected to be present. The calculation of travel-times in anisotropic structures is not as straight-forward as it is in isotropic structures, for reasons which will be explained later. In chapter 4, we describe how travel-times may be calculated in stratified anisotropic structures. The effect of anisotropy on travel-times is illustrated with reference to two examples of transversely isotropic structures of the type which are frequently encountered in oil exploration studies. We examine the effect of anisotropy on the processing of common-depth-point gathers.

Two applications of the anisotropic reflectivity technique are described in chapters 5 and 6. In common with its isotropic equivalent, the anisotropic reflectivity technique was originally developed in order to investigate the dynamic characteristics of wave propagation through the crust and upper-mantle. There is much evidence to suggest that the top of the upper-mantle is anisotropic over many regions of the earth. In chapter 5, we use synthetic seismograms to examine the feasibility of investigating upper-mantle anisotropy by the detection and analysis of anomalous body-wave arrivals from local and regional sources.

A quite different application is discussed in chapter 6. In this case, the theoretical model is derived from the crack-geometry of a geothermal reservoir in hot dry rock, which has been artificially fractured to provide a circulation path for fluids. The crack-geometry, and observational evidence from recorded seismograms, suggests the existence of a waveguide which is anisotropic due to the presence of aligned microcracks. The anisotropic reflectivity technique provides a means of modelling wave propagation in such a waveguide with allowance for its anisotropy.

Finally, in chapter 7 we present some suggestions for future work, which are based on the work in this thesis.

CHAPTER 2

THE REFLECTIVITY TECHNIQUE FOR ISOTROPIC MEDIA

2.1 Introduction

At present, the reflectivity technique is probably the most commonly used technique for generating exact synthetic seismograms for curved wavefronts in horizontally-stratified isotropic media. The technique was originally developed by Fuchs (1968a,b, 1971) and Fuchs & Müller (1971) from the matrix formulations of Haskell (1953). In the first applications of the method, seismograms were calculated for P-waves from an explosive point source, reflected from a laterally homogeneous, multilayered, isotropic reflection-zone situated below source and receiver.

The method has since been adapted and extended by many different workers. Fuchs (1975) presented synthetic seismograms for PS reflections. Kennett (1975a) made provision for a type of laterally varying structure, where the layering above the reflection-zone was allowed to differ beneath source and receiver. Kind & Müller (1975) used a double-couple point-source to examine reflected SV-waves in models of the earth's crust and the whole earth. Kennett (1975b) examined the effects of attenuation by using complex velocities in the description of the layered structure. Stephen (1977) computed seismograms for the case where the receiver is located within the reflection-zone, with the aid of an algorithm devised by Kennett (1974).

Kind (1978), Kennett & Kerry (1979) and Kennett (1980) extended the technique further to allow the seismic source to lie within the reflection-zone. This development permitted the calculation of complete seismograms of surface-waves, leaking modes, and all body-wave phases,

including depth phases like pP. Kind (1979) has shown how time-aliasing effects may be eliminated. In another recent theoretical development, Fryer (1980) has reformulated the reflectivity technique so that intermediate results obtained during the computation can be used to assist the interpretation of the final seismograms.

The reflectivity technique permits examination of the dynamic characteristics of arrivals on exact seismograms for many different horizontally-stratified structures (Fuchs 1968a, 1970, 1975). The technique was originally developed in order to aid the interpretation of data from long range seismic profiles, and its use for this purpose is now widespread. The earliest applications of the technique include those of Fuchs & Müller (1971), Hirn, Steinmetz, Kind & Fuchs (1973), Edel, Fuchs, Gelbke & Prodehl (1975), and Kennett (1975a). Braile & Smith (1975) have given a good selection of synthetic seismograms as a guide to the interpretation of crustal refraction profiles. Fertig & Müller (1978), and Kennett (1979) have shown how the method may aid reflection seismology in prospecting for coal and oil, respectively.

All previous theoretical formulations of the reflectivity technique have assumed the existence of a plane-layered, homogeneous and isotropic reflection-zone. In the present work we shall extend the formulation of the method to a plane-layered, homogeneous anisotropic reflection-zone.

It must be kept in mind that numerical calculations are usually substantially more complex, and therefore expensive in computer time, when they are performed in anisotropic media rather than in isotropic media (Bamford & Crampin 1977). The isotropic reflectivity technique itself requires long computing times. Even if there are few conceptual difficulties in adapting the most sophisticated developments of the

original reflectivity technique for anisotropic media (Kennett & Kerry 1979), computing restrictions make it impracticable for us to do this at the present time. Therefore in adapting the reflectivity technique for anisotropic media we shall not use the general method of Kennett & Kerry (1979), which provides for a general type of source (including a buried source), and a free surface above source and receiver. We shall restrict ourselves to adapting for anisotropic media the reflectivity technique of Fuchs & Müller (1971), using the later modification by Stephen (1977) which allows the receiver to lie in the reflection-zone.

The remainder of this chapter is used to outline the theory of the reflectivity method for an isotropic reflection-zone, largely following Fuchs (1971), and to point to how the method may be adapted for an anisotropic reflection-zone. First, we describe the plane-layered model to which the method is applied. We then show that the wave potential spectrum of a curved wavefront from a point source can be written as an integral of plane wave potentials. Plane wave propagation through a plane isotropic reflection-zone, with given boundary conditions, is described by matrix formulations which give the plane wave potentials for each wave in each layer in terms of potential excitation factors.

In anisotropic media it is more convenient to describe wave propagation in terms of displacements. We shall conclude this chapter by showing how the integral over plane wave potentials may be rewritten as an integral over plane wave displacements, involving component polarization vectors and displacement excitation factors. The resulting expression gives the component displacement spectra for waves from a point source. In the following chapter we show how the reflectivity technique may be extended to anisotropic media by substituting anisotropic plane wave displacements into the integral expressions.

2.2 Description of the theoretical model

A point source of elastic energy S is located at the origin of a cylindrical coordinate system (r,θ,z) where z is taken as positive downward, and a cartesian coordinate system (x_1,x_2,x_3). The point source lies immediately below the surface of a plane layered halfspace, as illustrated in Fig.2.1. The receiver may be located at any point in the layered halfspace, and we shall refer to the vertical plane containing both source and receiver as the sagittal plane.

The interface $z = 0$ may represent the free surface, and we can allow for reflections from the free surface at a receiver immediately beneath the interface by using the methods of Červený & Ravindra (1971) or Fuchs & Müller (1971). Alternatively, we can ignore the free surface effect by taking the upper halfspace to be solid and of the same material as the top layer.

The layered halfspace comprises an isotropic top layer above a multilayered transition-zone (layers 1 to (n-1)) and halfspace ('layer' n). The transition-zone and halfspace together form the reflection-zone. The layers which constitute the reflection-zone are assumed to be isotropic, in the original formulation of the method. In the next chapter we shall introduce the modifications to the reflectivity method which will allow them to become anisotropic.

An arbitrary depth-dependent distribution of elastic moduli and density can thus be approximated by n sufficiently thin homogeneous layers above a halfspace. Each isotropic medium may be characterised by its P- and S-wave velocity α_m and β_m respectively, its density ρ_m, and the depths d_m , d_{m+1} of the interfaces m, m+1, which form its boundaries.

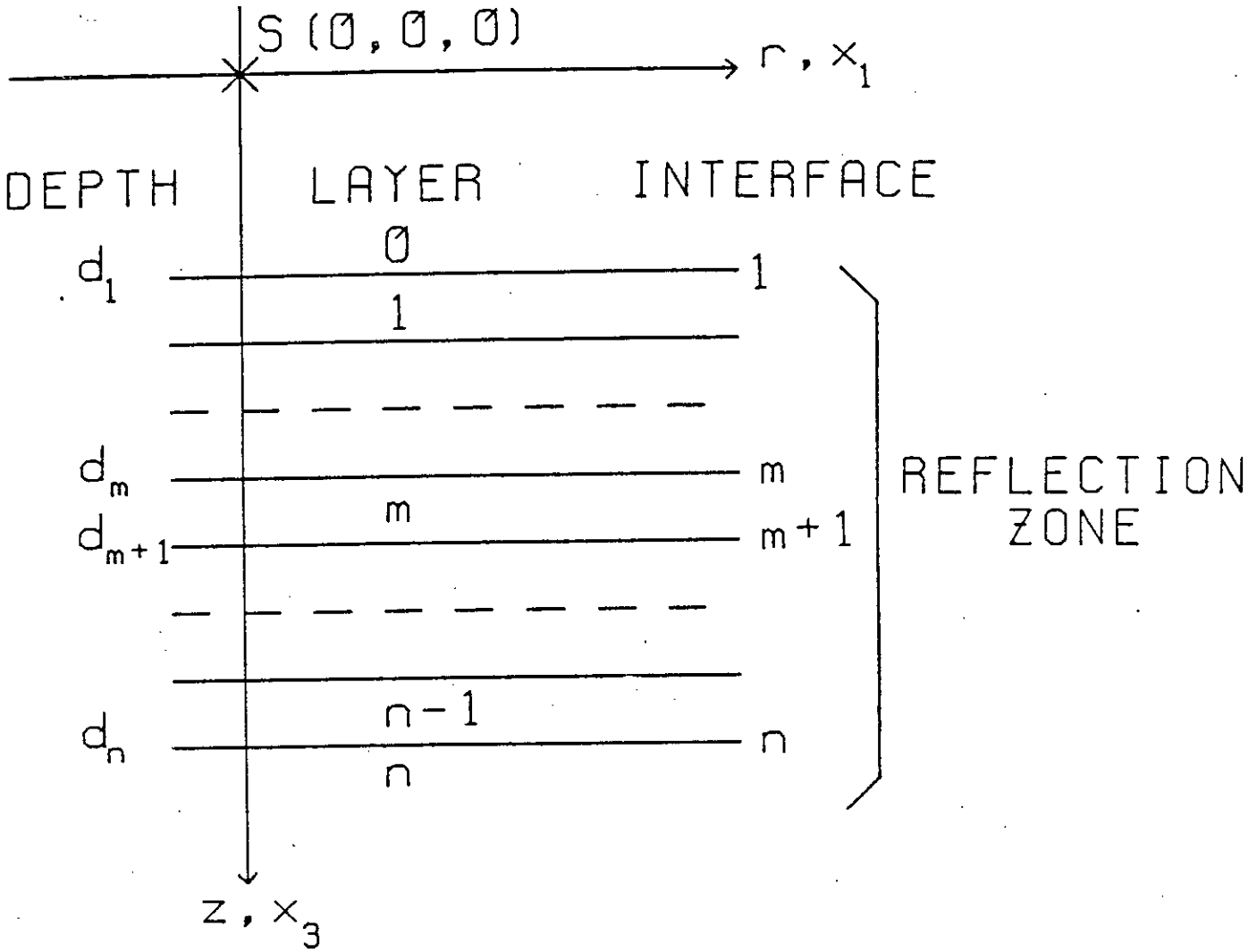

Figure 2.1 Configuration of the reflection zone.

2.3 Solution of the isotropic wave equations for a curved wavefront from a point source

In an isotropic medium, wave propagation can be described in terms of three scalar potentials ϕ, ψ and X corresponding to P-, SV- and SH-wave propagation. The potentials are solutions of the wave equations

$$\nabla^2\phi = \frac{1}{\alpha^2}\frac{\partial^2\phi}{\partial t^2}, \quad \nabla^2\psi = \frac{1}{\beta^2}\frac{\partial^2\psi}{\partial t^2}, \quad \nabla^2 X = \frac{1}{\beta^2}\frac{\partial^2 X}{\partial t^2} \tag{2.3.1}$$

and the displacements in the radial, transverse and vertical directions in cylindrical coordinates are:

$$u_r = \frac{\partial\phi}{\partial r} + \frac{\partial^2\psi}{\partial r\,\partial z}$$

$$u_\theta = -\frac{\partial X}{\partial r} \tag{2.3.2}$$

$$u_z = \frac{\partial\phi}{\partial z} + \frac{\partial^2\psi}{\partial z^2} - \frac{1}{\beta^2}\frac{\partial^2\psi}{\partial t^2}$$

where the potentials are as defined in Müller (1969), and α and β are the P- and S-wave velocities respectively.

Solutions of (2.3.2) for monochromatic spherical waves radiating from the origin, and satisfying the radiation criterion at infinity, are potentials of the form

$$\Omega_j = (A_j/R).\exp[i(\omega t - k_j R)], \quad j=1,2,3 \tag{2.3.3}$$

where $\Omega_j = \phi, \psi$ and X, and $k_j = \omega/\alpha$, ω/β and ω/β for j=1,2,3 respectively. A_j is the excitation constant of the wave, and $R = (r^2 + z^2)^{1/2}$.

The Fourier transformed potential of a spherical wave from a point source may be expressed as an integral of cylindrical-wave potentials by

the use of Sommerfeld's integral. For a source wave potential of type j, the solutions in layer m are

$$\bar{\Omega}_j^m(p) = \int_0^\infty J_o(kr).g_j^m(p).\exp[-i\omega q_p^m(z-d_m)].k/(i\omega q_j^0).dk \ , \ p = 1,2,..,6, \quad (2.3.4)$$

where J_o is the zero order Bessel function of the first kind. The variable of integration k is the horizontal wavenumber ω/c, where c is the horizontal apparent velocity. The potentials $\bar{\Omega}_j^m(p)$, p=1,2,3 represent downward travelling P-, SV- and SH-waves respectively, and $\bar{\Omega}_j^m(p)$, p=4,5,6 represent the corresponding upward travelling waves. The factors $g_j^m(p)$ are complex functions of k,ω and the layer parameters. They give the relative contribution of each wave-potential to the overall wave motion, and are termed 'potential excitation factors'. The vertical slownesses q_p^m are given by

$$\begin{aligned} q_j^m &= [(k_j^m)^2 - k^2]^{\frac{1}{2}}/\omega \ , \ k<k_j^m \\ &= -i[k^2 - (k_j^m)^2]^{\frac{1}{2}}/\omega \ , \ k>k_j^m \end{aligned} \quad (2.3.5)$$

$$q_{j+3}^m = -q_j^m \ , \ \text{for } j = 1,2,3 \ ,$$

and the integration can be restricted to a range of apparent velocities covering the principal wave arrivals of interest (Fuchs & Müller 1971).

Each of the first three terms of the integrand provides path dependent phasing of the arrivals at the receiver at (r,0,z) from the source at (0,0,0). J_o applies the horizontal phasing to distance r, $g_j^m(p)$ gives the vertical phasing to the top of layer m at depth d_m, and the exponential term phases the solution down to depth z. In the sagittal plane, the cylindrical-wave potential

$$\bar{\Phi}_j^m(p) = J_o.g_j^m(p).\exp[-i\omega q_p^m(z-d_m)] \quad (2.3.6)$$

represents a plane-wave potential solution for a wave of type p due to a source wave of type j.

Hudson (1969) has shown that the potentials and displacements due to excitation by a general point source are summations of Bessel functions $J_m(kr)$ for $m \leq 2$. The calculation of the excitation factors for five different angular orders in anisotropic media would pose a problem, due to the excessive computer time required. However Müller (1969) shows that the expressions for the potentials and displacements due to point sources commonly used for seismic propagation, such as explosions, single and double couples, and (Pilant 1979) linear doublets, asymptotically involve only zero and first order Bessel functions.

In the present work we shall limit ourselves to the calculation of far field displacements, where

$$J_1(x) \sim iJ_o(x) \text{ , for large } x \qquad (2.3.7)$$

and so we can write the general expression for the far-field potential spectrum in layer m in the form

$$\bar{\Omega}_j^m(p) = F\int_0^\infty S_j . J_o . g_j^m(p) . \exp[-i\omega q_p^m (z-d_m)] . dk \text{ , for } p = 1,2,..,6. \qquad (2.3.8)$$

where $F(\omega)$ is the source spectrum and $S_j(k)$ is a function depending on the type of source. For an explosive source in layer 0, which generates a spherical compressional wave, we have

$$S_1 = k/(i\omega q_1^0)$$

from equation (2.3.4).

Integral expressions which give the displacements in each component direction are obtained for each wave-type by differentiation of (2.3.8) according to the equations (2.3.2). In order to obtain the synthetic

seismogram for a given component at a given distance range, the displacement integrals must be evaluated for a range of frequencies covering the dominant frequencies of the source spectrum. Then a Fourier transform of the displacement spectrum into the time domain gives the synthetic seismogram.

The expression of the curved wavefront solutions (2.3.4) and (2.3.8) in terms of plane wave solutions allows us to use matrix formulations to describe the propagation through a multilayered structure, in terms of the potential excitation factors $g_j^m(p)$. These formulations were originally developed by Thomson (1950) and Haskell (1953) and have since been generalised and improved (Gilbert & Backus 1966; Kennett 1974; Kennett & Kerry 1979).

2.4 Plane wave propagation through an isotropic reflection-zone

We define a stress-displacement vector

$$\underline{V} = (u_1, u_2, u_3, \sigma_{13}, \sigma_{23}, \sigma_{33})^T, \qquad (2.4.1)$$

whose elements are the component displacements and the vertical components of the stresses, respectively. $\underline{V}$ is continuous across any horizontal interface. The stress-displacement vectors at the top and bottom interfaces m and n of any plane isotropic sequence of layers are related by

$$\underline{V}^m = P\,\underline{V}^n \qquad (2.4.2)$$

where P is the 6 x 6 propagator matrix for the particular layer sequence (Gilbert & Backus 1966). Since the media are isotropic, there is no transformation of energy between the sagittal and transverse components of

the wave motion, and thus the corresponding elements of the transform matrix P are zero-valued.

The stress-displacement vector $\underline{V}$ is given in terms of the vector of plane wave potentials in layer m by

$$\underline{V}^m = \mathbf{T}^m \underline{\Phi}^m , \qquad (2.4.3)$$

where $\underline{\Phi}^m$ is the vector of plane wave potentials $(\Phi_j^m(1), \Phi_j^m(2), \Phi_j^m(3))^T$ for downward and upward propagating waves. The 6 x 6 operator matrix $\mathbf{T}$ performs differentiations on the potentials to give the displacements and stresses. For example, the displacements are given by equation (2.3.2). The elements of $\mathbf{T}$ for the sagittal plane are given by Fuchs (1971), and in the transverse direction the elements are given by Kind (1976).

To solve (2.4.2) and (2.4.3) for the plane wave potentials in a layer, for substitution in the equation (2.3.6), we need to apply the appropriate boundary conditions according to the type of source wave, and the radiation conditions at infinity. We assume no energy is radiated upwards from the lower halfspace. This gives

$$\Phi_j^n(4) = \Phi_j^n(5) = \Phi_j^n(6) = 0 \qquad (2.4.4)$$

If we consider a plane P-wave incident on the upper boundary of the reflection-zone, we have

$$\Phi_1^0(2) = \Phi_1^0(3) = 0 \qquad (2.4.5)$$

The excitation factor for the source wave incident downward on the reflection-zone may be set at an arbitrary value; we normalise it to unity. From equation (2.3.4), at the top of layer 0, at depth $d_0 = 0$, we can

define the plane wave potential vector

$$\underline{\Phi}_0(0) = (1 , 0 , 0 , g_1^0(4) , g_1^0(5) , g_1^0(6))^T \qquad (2.4.6)$$

while in the lower halfspace at depth d_n,

$$\underline{\Phi}_n(d_n) = (g_1^n(1) , g_1^n(2) , g_1^n(3) , 0 , 0 , 0)^T \qquad (2.4.7)$$

The equations (2.4.2) and (2.4.3), coupled with the boundary conditions (2.4.6) and (2.4.7), may be solved to give the excitation factors and wave potentials generated at any point in layer m by the incident plane P-wave. The potentials due to SV and SH incident waves may also be calculated by a similar procedure with the appropriate boundary conditions. For each wave-type in each layer, the excitation factors give the response due to wave propagation through the whole layer sequence, including all multiples and interconversions.

The potential excitation factors described above correspond to the reflection and trasnsmission coefficients used by Fuchs (1971), Kennett (1974) and others. For example, $g_1^n(1)$ is the transmission coefficient T_{PP} through the entire layer sequence, and $g_1^0(5)$ is the reflection coefficient R_{PSV} for SV-waves converted from P-waves incident on the reflection-zone.

The excitation factors corresponding to P,SV->SH and SH->P,SV wave conversions are zero for isotropic media, due to the decoupling of the sagittal and transverse wave motions. The decoupling of the wave motions enables each 6 x 6 matrix P and T in equations (2.4.2) and (2.4.3) to be split into two matrices of dimensions 4 x 4 and 2 x 2, corresponding to sagittal and transverse wave motion respectively. The matrix multiplications involved in the calculation of the propagator matrix and

the solution for the potential excitation factors are then greatly reduced.

In practice it can be difficult to obtain the excitation factors by the Gilbert-Backus method as outlined above, due to loss of precision in the computations. Kind (1976) constructed a fast computer program for the calculation of excitation factors in an isotropic layer sequence. He overcame the inaccuracy problem by using a technique which employed reduced matrices in the matrix computations, following earlier work by Dunkin (1965) and Watson (1970).

Kennett (1974) devised a convenient iterative technique for the calculation of excitation factors, which also avoided the inaccuracy problem. This technique is easily adapted for anisotropic propagation, as we shall see in section 3.6 of the following chapter, where it is described in detail.

The calculation of the plane wave excitation factors for the given reflection-zone is the fundamental operation in the reflectivity method, and the most time-consuming. The factors must be calculated for a range of horizontal apparent velocities (or slownesses) covering the principal wave arrivals, and this must be done for each frequency of interest in the source spectrum. Each range of values must be closely spaced to minimise aliasing problems.

The excitation factors $g_j^m(p)$ which have been used in this section are defined in terms of plane wave solutions of the equations of motion (2.3.1) for wave potentials. In anisotropic media it is more convenient to describe wave motion in terms of plane wave displacements. In the following section we show how the displacements due to a curved wavefront may be written as an integral of plane wave displacements, involving excitation factors defined in terms of displacement amplitudes. We shall see in chapter 3 that the reflectivity method can be extended to weakly anisotropic layered structures by substituting anisotropic plane wave

displacements for the isotropic plane wave displacements in the expression for the curved wavefront displacements.

2.5 Curved wavefront displacements reformulated for anisotropic media

In anisotropic media the sagittal and transverse wave motions do not decouple and it is no longer convenient to describe wave motion in terms of potentials. Wave displacements are used to describe wave motion in anisotropic media. In this section we shall express the displacements of a curved wavefront in an isotropic medium in terms of an integral of plane wave displacements.

In the sagittal plane we have the equivalences $x_1 = r$, $x_3 = z$. A general plane harmonic solution of the wave equations for the component displacements u_i , i=1,2,3 in the mth layer, which may be isotropic, or anisotropic, may be written:

$$u_i = \sum_{p=1}^{6} f^m(p).a_i^m(p).\exp\{i\omega[t-x_1/c-q_p^m(x_3-d_m)]\} \qquad (2.5.1)$$

(Keith & Crampin 1977a).

The $f^m(p)$ are excitation factors which give the relative wave displacement amplitude of each wave-type p in the direction of its unit displacement vector $\underline{a}^m(p)$. The orientation of the unit displacement vectors $\underline{a}^m(p)$ in isotropic media are defined in Fig.2.2 for p=1,2,3, corresponding to downward P-, SV- and SH-waves respectively and p=4,5,6, corresponding to upward P-, SV- and SH-waves respectively. Each component of the displacement is obtained by multiplication of the $f^m(p)$ with the appropriate direction cosine of $\underline{a}^m(p)$. In isotropic media, these projections of $\underline{a}^m(p)$ along the three component directions, $a_i^m(p)$, are easily written in terms of the wavenumbers k, k_j and ωq_j^m, where j = 1,2,3,

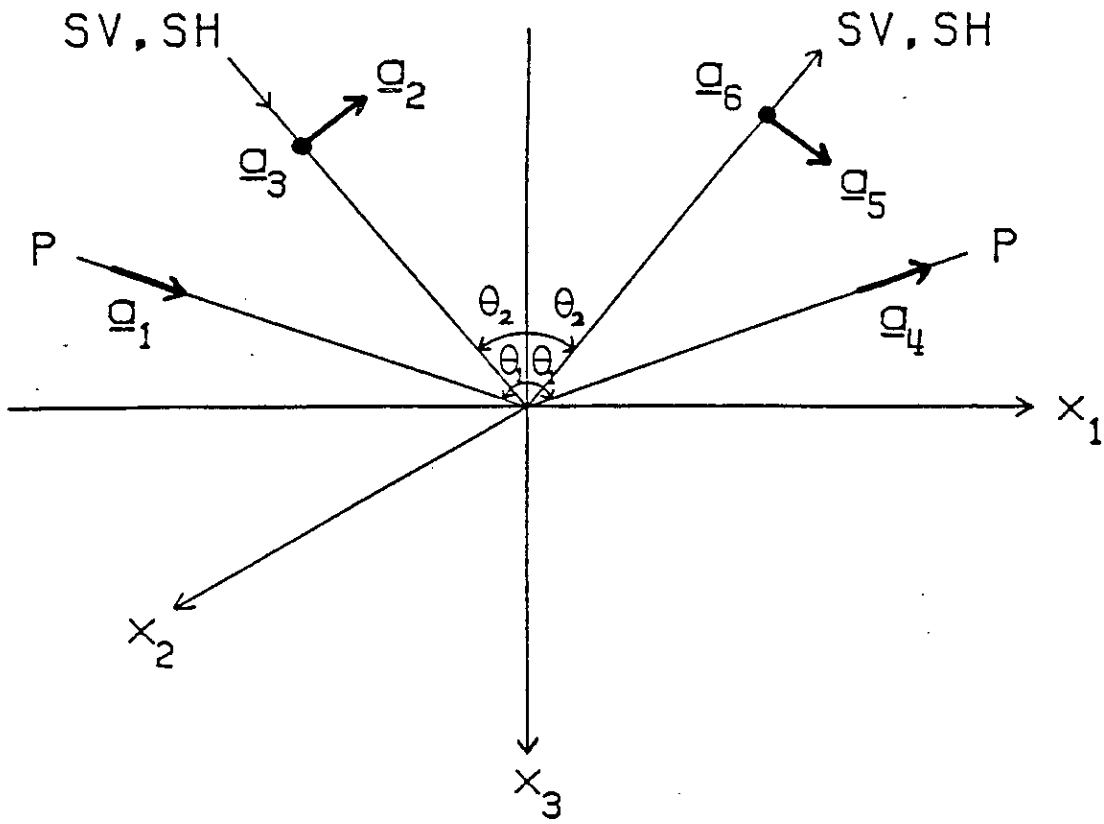

Figure 2.2 Unit polarization vectors $\underline{a}_p$, p = 1,2,..6 of the downward and upward waves. The $\underline{a}_3$ and $\underline{a}_6$ vectors for the SH-waves are directed in the x_2 direction, orthogonal to the x_1 and x_3 axes and out of the paper.

and they are given in Table 2.1.

We have seen in section 2.3 that the far-field wave potential spectrum of a curved wavefront in isotropic media can be written as an integral of simple plane wave potentials for simple seismic source types (equation 2.3.8). The component displacements of the wavefront are obtained by differentiating the wave potential according to (2.3.2). The expressions for the potentials and the displacements involve wave potential excitation factors. In isotropic media we can obtain relationships between the potential excitation factors $g_j^m(p)$ and the displacement excitation factors $f_j^m(p)$. These relationships are derived in Appendix 1.

By using the relation between the displacement and potential excitation factors, we can write the expressions for the curved wavefront displacements as integrals of plane wave displacements of the type (2.5.1), multiplied by a source term S_j. This operation is performed in Appendix 2 for the displacements due to an explosive source, as an example. The resulting expression for the spectra of the total displacement components u_i, for i=1,2,3, at the point (x_1, x_3) in layer m is:

$$u_i(\omega) = F(\omega)\sum_{j=1}^{3}\sum_{p=1}^{6}\int_0^{\infty} S_j . f_j^m(p) . a_i^m(p) . J_o(kx_1) . \exp[-i\omega q_p^m(x_3 - d_m)] . dk \qquad (2.5.2)$$

where j=1,2,3 refers to the three possible source waves P, SV, SH respectively; p=1,2,..,6 refers to the six possible wave-types in each layer; $F(\omega)$ is the source spectrum. The form of S_j depends on the type of source and the amplitude directivity of the source wave type j. The P- and SV-wave directivity patterns for four types of point source are illustrated in Fig.2.3, with the corresponding functions S_j for each source type in Table 2.2. Note that the S_j in equation (2.5.2) involving $f_j^m(p)$ is not the same as the S_j in equation (2.3.8) involving $g_j^m(p)$.

We have derived an expression for the component displacements of waves

Table 2.1 Relative values of $a_i(p)$ for an isotropic layer in terms of wavenumbers k, k_1, k_2, ν_1, and ν_2, where $\nu_i = \omega q_i$, and the angles θ_1 and θ_2 which are shown in Fig.2.2.

i	p=1	p=2	p=3	p=4	p=5	p=6
1	k/k_1 $(\sin\theta_1)$	ν_2/k_2 $(\cos\theta_2)$	0	k/k_1 $(\sin\theta_1)$	ν_2/k_2 $(\cos\theta_2)$	0
2	0	0	1	0	0	1
3	ν_1/k_1 $(\cos\theta_1)$	$-k/k_2$ $(-\sin\theta_2)$	0	$-\nu_1/k_1$ $(-\cos\theta_1)$	k/k_2 $(\sin\theta_2)$	0

Table 2.2 Values of S_j for each wave-type for the point sources in Fig.2.3. The couples may be rotated by θ about the x_3 axis, and the doublet by ϕ about the x_1 axis to generate SH motion. $D = -1/4\pi\rho\omega^2$

Source type	P: j=1	SV: j=2	SH: j=3
Explosion (Fuchs & Müller 1971)	$\frac{-k\,k_1}{\nu_1}$	0	0
Single couple (Müller 1969)	$D\,\frac{k\,k_1^3}{\nu_1}\left(\frac{k\,\nu_1}{k_1^2}\right)\cos\theta$	$D\,\frac{k\,k_2^3}{\nu_2}\left(\frac{\nu_2}{k_2}\right)^2\cos\theta$	$D\,\frac{k\,k_2^3}{\nu_2}\left(\frac{\nu_2}{k_2}\right)\sin\theta$
Double couple (Kind & Müller 1975)	$D\,\frac{k\,k_1^3}{\nu_1}\left(\frac{2k\,\nu_1}{k_1^2}\right)\cos\theta$	$D\,\frac{k\,k_2^3}{\nu_2}\left(\frac{\nu_2^2-k^2}{k_2^2}\right)\cos\theta$	$D\,\frac{k\,k_2^3}{\nu_2}\left(\frac{\nu_2}{k_2}\right)\sin\theta$
Linear doublet (Pilant 1979)	$D\,\frac{k\,k_1^3}{\nu_1}\left(\frac{\nu_1}{k_1}\right)^2\cos^2\phi$	$-D\,\frac{k\,k_2^3}{\nu_2}\left(\frac{k\,\nu_2}{k_2^2}\right)\cos^2\phi$	$D\,\frac{k\,k_2^3}{\nu_2}\left(\frac{\nu_2}{k_2}\right)\sin\phi\cos\phi$

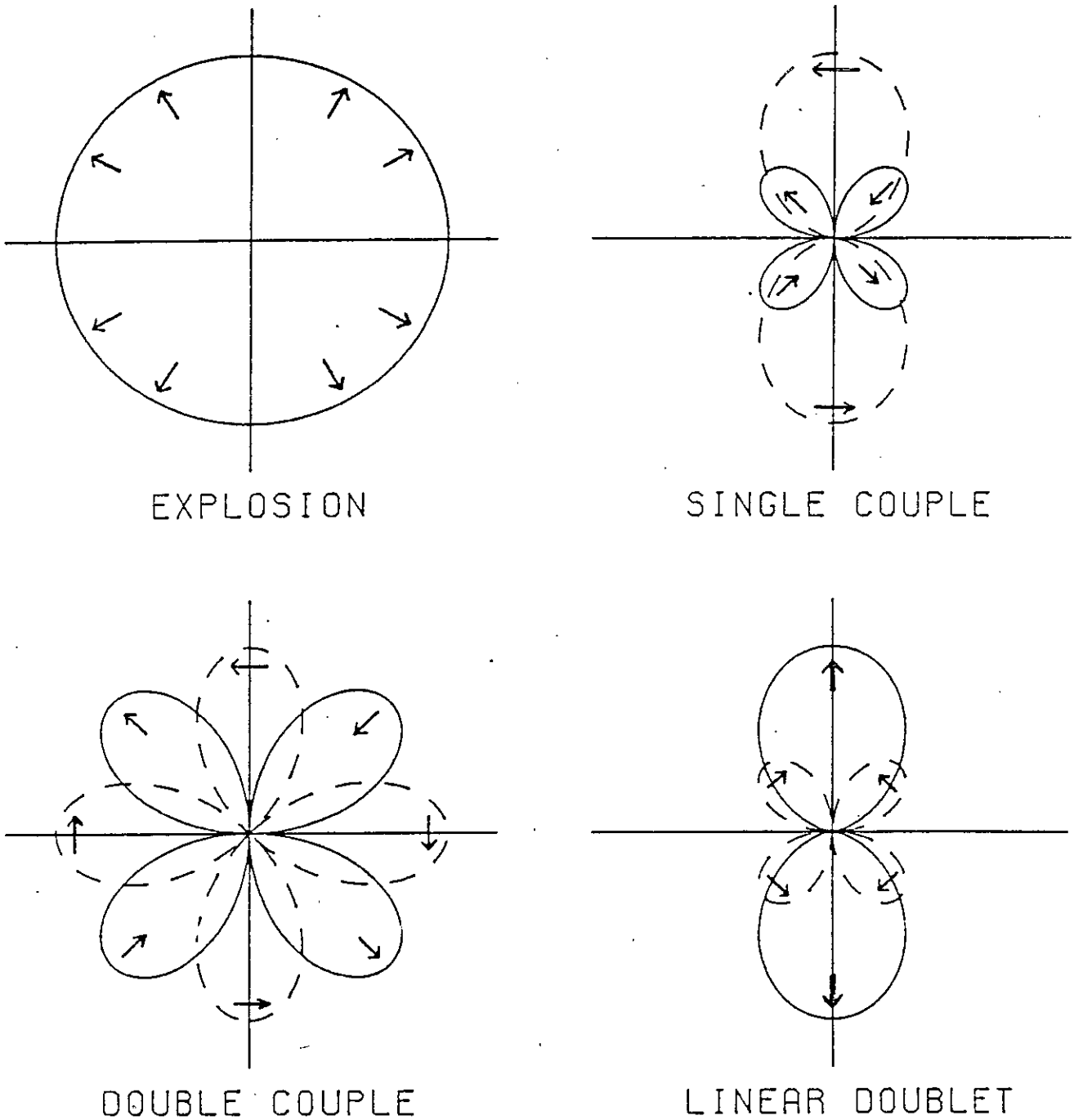

Figure 2.3 Amplitude directivity patterns for P- and SV-waves (solid and dashed lines, respectively) generated by an explosion, a single-couple, a double-couple, and a linear doublet. The force systems of the couple and doublet sources lie in the plane which is formed by the two co-ordinate axes.

in an isotropic medium from a point source which is also in an isotropic medium. The expression is an integral of plane wave component displacements, which are multiplied by a source function. To obtain a reasonable approximation to the component displacements in a weakly anisotropic medium, we shall substitute plane wave displacements which are solutions of the anisotropic equations of motion and which can be expressed in the form of equation (2.5.1).

In the following chapter we show how the anisotropic plane wave solutions are obtained, and we describe some of the characteristic differences between anisotropic and isotropic propagation. The iterative technique of Kennett (1974) is extended to the calculation of anisotropic displacement excitation factors, and we describe the computational procedure which is used to generate synthetic seismograms for anisotropic reflection-zones.

CHAPTER 3

THE REFLECTIVITY TECHNIQUE APPLIED TO ANISOTROPIC MEDIA

3.1 Introduction

In this chapter we extend the reflectivity technique to a plane layered anisotropic reflection-zone under an isotropic top layer containing the source. We start by showing how an anisotropic medium may be characterised by its elastic constants. Then we obtain solutions to the anisotropic equations of motion for the component displacements of plane waves, which may be written in terms of anisotropic polarization vectors and displacement excitation factors. We describe some characteristic features of plane wave propagation in anisotropic media which do not appear in isotropic media. These features will be described as anomalous with respect to isotropic propagation. The component displacements due to a curved wavefront in an anisotropic medium are then expressed as an integral of plane wave solutions. When we make the assumption that the anisotropic media are weakly anisotropic, this integral may be expressed in the same form as the equivalent expression for isotropic media which was given in chapter 2.

The reflectivity technique is quite easily adapted to anisotropic media since it makes use of propagator matrices (Gilbert & Backus 1966) to describe plane wave propagation in a sequence of plane horizontal layers. A formulation for the calculation of propagator matrices for anisotropic structures has been developed by Crampin (1970). Application of the propagator matrices, with the appropriate boundary conditions, permits the plane wave propagation in each layer to be described in terms of displacement excitation factors for each wave-type.

As in the isotropic case, direct use of the propagator matrices can lead to numerical inaccuracies in the matrix computations. In order to avoid this problem, Kennett's iterative technique for the calculation of excitation factors (Kennett 1974) is extended to an anisotropic reflection-zone.

The computational procedure for the generation of synthetic seismograms by computer will be described for two different applications of the anisotropic reflectivity technique. We shall consider the case where the receiver is located in the layer above the reflection-zone (Fig.2.1), and also the case where the receiver is within the reflection-zone.

The computational procedure is then tested against an independent computational method. We conclude the chapter with a description of the approximation which is involved in the generation of anisotropic synthetic seismograms for a point source by this formulation of the reflectivity technique.

3.2 Elastic constants for anisotropic media

Any material exhibiting seismic anisotropy may be characterised by the effective elastic constant tensor $\{c_{jkmn}\}$ where the constants are ordered in some form of crystalline symmetry (Crampin 1977a). Following Crampin (1970), the equations of motion in an anisotropic medium may be written

$$\rho . \partial^2 u_j / \partial t^2 = p_{jk,k} \qquad j=1,2,3 \tag{3.2.1}$$

where p_{jk} is the stress given by $p_{jk} = c_{jkmn} . u_{m,n}$, and $u_{m,n} = \partial u_m / \partial x_n$. The fourth rank tensor c_{jkmn}, where $j,k,m,n = 1,2,3$, has 81 elements, which are reduced to 21 independent elements by the symmetry relations

$$c_{jkmn} = c_{kjmn} = c_{mnjk} \tag{3.2.2}$$

The number of independent elements is further reduced by any material symmetry. For an isotropic material the c_{jkmn} are linear combinations of two independent constants λ and μ (Lamé's constants).

In Appendix 3 we describe methods for obtaining the elastic constants of materials which exhibit crystalline or crack-anisotropy.

3.3 Plane wave propagation in anisotropic media

We wish to obtain plane wave solutions to the anisotropic equations of motion for the displacements in the multilayered structure illustrated in Fig.2.1. The plane wave solutions will be substituted in the integral expression (2.5.2) to yield the displacement spectra of a curved wavefront in the layer containing the receiver. In this section we describe plane wave propagation in one of the anisotropic layers, and in sections 3.5 and 3.6 we shall consider propagation through a sequence of layers.

Without loss of generality, we take the plane waves in an anisotropic medium to propagate in the x_1 direction, rotating the tensor of elastic constants c_{jkmn} if necessary to preserve this direction of propagation. We assume that plane wave solutions for the displacements are of the form

$$u_j = a_j . \exp[i\omega(t - q_k . x_k)], \qquad j,k = 1,2,3 \tag{3.3.1}$$

where $\underline{a}$ is the polarization vector and ω the angular frequency. The components q_1 , q_2 of the slowness vector $\underline{q}$ are $1/c$, 0 respectively, where c is the apparent phase velocity along the x_1 axis.

When we substitute (3.3.1) in the anisotropic equations of motion (3.2.1) we obtain three equations

$$\rho . a_j = c_{jkmn} . q_k . q_n . a_m , \qquad j = 1,2,3 \tag{3.3.2}$$

The requirement for a non-trivial solution to (3.3.2) yields a sextic polynomial in q_3 with real coefficients (Crampin 1970, Keith and Crampin 1977a). Solutions for q (dropping the subscript 3) are either real, corresponding to propagating waves, or in complex conjugate pairs. The complex solutions correspond to evanescent waves tied to the interface on which the wave energy is incident. Three roots correspond to upward, and three to downward propagating waves. Thus three body-waves will propagate in any given direction in an anisotropic medium: a quasi-P wave, qP, and two quasi-shear waves, qS1 and qS2. We order the six roots q_p, p=1,2,..,6 so that p = 1,2,3 correspond to downward (positive x_3 direction) qP-, qS1- and qS2-waves respectively, and p = 4,5,6 to upward travelling qP-, qS1-, and qS2-waves, respectively.

The polarization vector $\underline{a}(p)$ for each wave-type is obtained by substitution of the corresponding q_p in the equations (3.3.2) and solving for each component of $\underline{a}(p)$. Unlike its isotropic equivalent (Table 2.1), $\underline{a}(p)$ cannot easily be written in explicit form. In an equivalent but more general formulation, Taylor and Crampin (1978) treat the solution for q_p and $\underline{a}(p)$ as a linear eigenvalue problem. The eigenvalues are the squares of the velocities, and the corresponding eigenvectors are the polarizations.

A general solution to (3.2.1) in the anisotropic mth layer for a source wave type j is

$$u_i^m = \sum_{p=1}^{6} f_j^m(p).a_i^m(p).\exp\{i\omega[t - x_1/c - q_p^m(x_3 - d_m)]\}, \quad i=1,2,3 \qquad (3.3.3)$$

where the $f_j^m(p)$ are the relative excitation factors of each wave-type in the anisotropic layer. In the next section we express the spectra of the components of displacement of a curved wavefront as an integral of plane wave displacements. We close this section with a short description of the

properties of the plane wave solution and the anomalous characteristics of body-wave propagation in anisotropic structures. These characteristics are discussed in more detail in Crampin (1977a,1981), Keith & Crampin (1977a,b,c) and Crampin, Stephen & McGonigle (1982).

We have seen that for propagation in any direction in an anisotropic medium there always exists three body-waves, and their velocities and polarizations will vary with the direction of propagation. However, for any given orientation of the propagation vector, the polarizations will be orthogonal and fixed in the material with respect to the propagation direction (Crampin 1977a).

The polarizations of qS1 and qS2 will only be parallel to SV and SH for propagation in particular symmetry directions in the anisotropic material. In general the orthogonal particle motions are not coincident with the dynamic axes formed by the propagation vector and plane of constant phase. Thus the propagation of energy at the group-velocity diverges from the propagation vector, when the propagation vector is not aligned along a symmetry direction. This is equivalent to stating that, in general, the group-velocity vector diverges from the phase-velocity or propagation vector. The phase-velocity is the velocity which appears in the equations of motion and in most other theoretical expressions, while it is the group-velocity which is measured in most observations.

The divergence of the velocity vectors results in fundamental differences in the propagation characteristics of plane and spherical wavefronts (Crampin & McGonigle 1981). Two orthogonally-polarized <u>plane</u> shear-waves propagate at the phase-velocity in any given direction in an anisotropic medium. Their wavefronts will be parallel, and normal to the propagation vector. In observational seismology, it is more appropriate to consider <u>spherical</u> waves, for which the energy propagates at the group-

velocity along a ray in a direction which is not, in general, normal to the wavefront. If there are no cusps in the group-velocity surface, two shear-waves will propagate along a ray (Crampin & Yedlin 1980). They will not, in general, have orthogonal polarizations, since they will be associated with different propagation vectors.

The divergence of the group and phase velocity vectors, which is discussed further in chapter 4, gives rise to other anomalies of wave propagation in anisotropic structures. Away from symmetry directions, each type of wave which is incident from an isotropic medium on to an interface with an anisotropic medium will generate qP-, qS1- and qS2-waves in the anisotropic medium,and P-,SV- and SH-waves in the isotropic medium. This is due to the anomalous polarizations in the anisotropic medium and the condition of continuity of stresses and displacements at (horizontal) interfaces. Thus anomalous converted phases such as P->SH, SH->P, SV->SH, SH->SV will occur.

The amplitudes of SH- and qSH-waves generated by incident P-waves are small, since the qP-waves have small transverse components and most of the energy is converted to qP. However, since the relative amplitudes of the qS1- and qS2-waves are fixed by the anisotropy, there may be strong cross-coupling between SV- and SH-wave energy for an incident shear wave. For some orientations, incident SV- or SH-waves can convert into qS1- and qS2-waves with approximately equal amplitudes.

The two orthogonally-polarized quasi-shear waves will propagate through the anisotropic solid with different velocities. On entering an isotropic medium again the two quasi-shear waves generate two separate and anomalous shear-waves in the isotropic material, with orthogonal polarizations. The separation of these two waves depends on the relative time delays of the two quasi-shear waves in the anisotropic material.

This anomalous phenomenon is known as <u>shear-wave splitting</u>. The

presence on recorded seismograms of two closely-separated shear-wave arrivals, with orthogonal or near-orthogonal polarizations, strongly suggests the presence of anisotropy. This anomaly of anisotropic propagation is particularly significant since it depends on the orientation and path length of the quasi-shear waves in the anisotropic material rather than the degree of anisotropy (Crampin 1977a).

3.4 Displacements due to a curved wavefront in an anisotropic medium

The components of displacement on a curved wavefront in anisotropic media can also be written as an integral of plane wave displacements. In cartesian coordinates, the double integral expression

$$\bar{u}_i(\omega) = F(\omega)\sum_{j=1}^{3}\sum_{p=1}^{6}\int_0^{\infty}\int_0^{\infty} S_j . f_j^m(p) . a_i^m(p) . \exp[-i\omega q_p^m(x_3 - d_m)] . \exp(ik_1 x_1) . dk_1 dk_2 \qquad (3.4.1)$$

gives the component displacement spectra $\bar{u}_i(\omega)$ at the point $(x_1, 0, x_3)$ due to a point source at the origin of coordinates. In this expression k_1 and k_2 are the radial and transverse components, respectively, of the horizontal wavenumber vector. The terms S_j, $f_j^m(p)$, $a_i^m(p)$, and q_p^m represent the same parameters as the equivalent terms in section 2, but in an anisotropic medium they possess an azimuthal dependence and are thus functions of k_1 and k_2. In isotropic media the first part of the integral is a function of k_1 only.

If we make the assumption that the azimuthal variation of the first part of the integration is small, then the expression (2.5.2) becomes a reasonable approximation to (3.4.1). Thus we can allow each layer in the reflection-zone to be anisotropic, provided that we restrict the application of the technique to weakly anisotropic media. In order to

avoid difficulties in the mathematical representation of the source in anisotropic media, we assume the layer containing the source is isotropic. Thus the source function S_j, the source spectrum $F(\omega)$, and the use of the Bessel function J_o will remain the same as for an isotropic structure. A physical representation of the approximation which has been applied here is given in section 3.10. In the following two sections, we describe two methods for the calculation of the plane wave displacement excitation factors $f_j^m(p)$ in an anisotropic stratified structure.

3.5 Plane wave propagation through anisotropic layers: I - The direct method

The excitation factors in each layer of the anisotropic layer sequence may be found by direct application of the appropriate anisotropic propagator matrices (Crampin 1970), according to the appropriate boundary conditions. In section 2.4 we described an equivalent operation to find the potential excitation factors in an isotropic layer sequence.

In anisotropic media the stress/displacement vector V is related at interfaces m and (m+1) by the anisotropic propagator matrix A^m for layer m:

$$\underline{V}^{m+1} = A^m \underline{V}^m \qquad (3.5.1)$$

Also, the displacement excitation factor vector in layer m,

$$\underline{f}^m = (f^m(1), f^m(2), \ldots, f^m(6))^T,$$

is related to the stress/displacement vector $\underline{V}^m$ by

$$\underline{V}^m = E^m \underline{f}^m \quad . \qquad (3.5.2)$$

The 6 x 6 matrices A^m and E^m are complex functions of the anisotropic elastic constants, slownesses and polarization vectors.

However, as in the isotropic case, there is a loss-of-precision problem associated with the direct computation of the propagator matrices. The problem arises when the vertical slowness q in a layer becomes complex for any wave-type, corresponding to an evanescent wave in the layer. Then the argument of the exponential phasing term in the propagator matrix becomes real, and it is difficult to maintain sufficient accuracy in the computations, particularly at high frequencies. Keith & Crampin (1977b,c) did not use incident plane waves which could give rise to evanescent waves in their models, and so avoided this problem.

We have seen in section 2.4 that the problem can be overcome in isotropic media by the use of a reduced matrix technique (Kind 1976). The elements of the reduced matrices are formed from all the possible 2 x 2 subdeterminants of a 4 x 4 isotropic propagator matrix for wave motion in the sagittal plane, allowing for redundancy in the subdeterminants. However, this technique is not suitable for adaptation to anisotropic media, where a full 6 x 6 propagator matrix is required to describe the wave propagation in each layer. It would be computationally inefficient to calculate and manipulate all the possible subdeterminants of a 6 x 6 propagator matrix for each layer.

Kennett (1974) adapted the Gilbert-Backus propagator method to produce a convenient iterative method of solution for the excitation factors on either side of a stratified isotropic reflection-zone. The technique avoids the inaccuracy problem and is capable of easy physical interpretation. There is also a facility whereby the response in each layer may be truncated to that of the direct waves, or direct waves plus first multiples only. For the purposes of the present work, the technique has the additional advantage that it can easily be extended to wave

propagation through anisotropic media. A description of Kennett's technique, and the means by which it may be extended to anisotropic media, follows in the next section.

3.6 Plane wave propagation through anisotropic layers: II - The iterative method

In Kennett's scheme, we shall use excitation factors phased to the top and bottom of the layers. Factors $\underline{f}^m$ in (3.5.2) are phased with respect to the top of layer m, and we define $\underline{\tilde{f}}^m$ as phased with respect to the bottom. Then by equating the stresses and displacements at the top of layer m and the bottom of layer (m-1) we have

$$\underline{f}^m = (E^m)^{-1} E^{m-1} \underline{\tilde{f}}^{m-1} \qquad (3.6.1)$$

from (3.5.2). Also, from (3.3.3) we have

$$\underline{\tilde{f}}^m = D^m \underline{f}^m , \qquad (3.6.2)$$

where $D^m = \mathrm{diag}[-i\omega q_p^m.(d_{m+1} - d_m)]$ for p = 1,2,...6. We partition the D^m matrix into 3 x 3 Upward and Downward propagating components

$$D^m = \begin{pmatrix} D_D^m & 0 \\ 0 & D_U^m \end{pmatrix} ,$$

and we can write $\underline{f}^m = (\underline{f}_D^m , \underline{f}_U^m)^T$.

Kennett redefines the propagator matrices for a sequence of layers in terms of submatrices R_U, R_D, T_U, and T_D for each interface, whose elements are Reflection and Transmission coefficients for Upward and

Downward incident-waves respectively. Interface coefficients may be found for interface m by allowing layers (m-1) and m to extend to infinity upwards and downwards respectively. The boundary conditions at interface m for a wave incident from the (m-1)th layer are then:

$$\underset{\sim}{f}_U^{m-1} = R_D^m \, \underset{\sim}{f}_D^{m-1} \quad , \quad \text{and}$$
$$\underset{\sim}{f}_D^{m} = T_D^m \, \underset{\sim}{f}_D^{m-1} \quad , \tag{3.6.3}$$

where

$$R_D^m = \begin{pmatrix} r_{PP} & r_{1P} & r_{2P} \\ r_{P1} & r_{11} & r_{21} \\ r_{P2} & r_{12} & r_{22} \end{pmatrix}_D^m \quad \text{and} \quad T_D^m = \begin{pmatrix} t_{PP} & t_{1P} & t_{2P} \\ t_{P1} & t_{11} & t_{21} \\ t_{P2} & t_{12} & t_{22} \end{pmatrix}_D^m ,$$

and $(r_{1P})_D^m$, for example, is the interface coefficient for a reflected qP-wave from a qS1-wave incident Downwards on interface m and phased with respect to the bottom of the (m-1)th layer. There are similar relationships for upward propagating incident waves on interface m phased with respect to the top of layer m:

$$\underset{\sim}{f}_D^{m} = R_U^m \, \underset{\sim}{f}_U^{m} \quad , \text{ and}$$
$$\underset{\sim}{f}_U^{m-1} = T_U^m \, \underset{\sim}{f}_U^{m} \quad . \tag{3.6.4}$$

The interface coefficients are independent of frequency when expressed in this way with the phase of the excitation factors related to the interface where the transformation takes place. They are obtained by solving (3.6.1)

with the appropriate boundary conditions (3.6.3) and (3.6.4) for each incident wave-type. The reflection and transmission coefficients correspond to the appropriate upward and downward excitation factors for an incident wave of unit amplitude.

The various R and T matrices are the coefficients for individual interfaces. We write the overall reflection coefficient matrix for the sequence of layers from m to n for Downward propagating incident-waves as ${}^{m}\mathcal{R}_{D}^{n}$, where the first superscript refers to the layer containing the incident wave-field, and ${}^{m}\tilde{\mathcal{R}}_{D}^{n}$ is phased with respect to the bottom of layer m. Thus at the bottom of layer m, we have the relationship

$$\underline{\tilde{f}}_{U}^{m} = {}^{m}\tilde{\mathcal{R}}_{D}^{n}\,\underline{\tilde{f}}_{D}^{m} \,. \tag{3.6.5}$$

Phasing the excitation factors with respect to the top of layer m, we have

$$\begin{aligned} \underline{f}_{U}^{m} &= (D_{U}^{m})^{-1}\,{}^{m}\tilde{\mathcal{R}}_{D}^{n}\;D_{D}^{m}\,\underline{f}_{D}^{m} \quad , \text{ and} \\ {}^{m}\mathcal{R}_{D}^{n} &= (D_{U}^{m})^{-1}\,{}^{m}\tilde{\mathcal{R}}_{D}^{n}\;D_{D}^{m} \quad , \end{aligned} \tag{3.6.6}$$

and similar expressions for ${}^{n}\mathcal{R}_{U}^{m}$, ${}^{m}\mathcal{T}_{D}^{n}$, and ${}^{n}\mathcal{T}_{U}^{m}$.

Kennett's (1974) iterative scheme for calculating the excitation factors layer by layer through a sequence of isotropic layers involved 2 x 2 submatrices of 4 x 4 isotropic propagator matrices for P- and SV-waves. In order to extend the technique to anisotropic layers and 6 x 6 propagator matrices, we substitute 3 x 3 coefficient matrices of the type used in (3.6.3) to (3.6.6) into the iterative equations (30) and (31) of Kennett (1974). Thus the iterative equation for the overall reflection

coefficient at the top of layer (m-1) is

$$ {}^{m-1}\mathcal{R}_D^n = (D_U^{m-1})^{-1}\left[R_D^m + T_U^m\, {}^m\mathcal{R}_D^n \left(I - R_U^m\, {}^m\mathcal{R}_D^n\right)^{-1} T_D^m \right] D_D^{m-1} , \qquad (3.6.7) $$

with similar expressions for the other overall reflection and transmission coefficients.

All reverberations and associated mode-conversions in the iterative schemes are contained in the 3 x 3 matrix terms of the form $(I - X)^{-1}$. We may calculate the complete response of a sequence of layers by evaluating (3.6.7) with matrix inversions, or obtain only the response for the direct waves, or the direct waves and the first reverberations by expanding $(I - X)^{-1}$ and truncating the series expansion (Kennett 1974). This facility allows the reflectivity technique to be used for a wide range of applications, where, for example, propagation in a non-attenuative structure with a wave-guide would result in a long train of reverberations and lead to time-aliasing problems unless the number of reverberations is truncated in this way.

These iterative equations are applied successively until we have the response ${}^0\mathcal{R}_D^n$ for the whole layered sequence for a source in layer 0. The appropriate excitation factors to evaluate (2.5.2) at a receiver at the surface from a surface source are then

$$ \underline{f}_U^0 = {}^0\mathcal{R}_D^n\, \underline{f}_D^0 \qquad (3.6.8) $$

When we wish to calculate seismograms at a receiver which is located in a layer within the reflection zone, the excitation factors for upward and downward waves must be calculated. Stephen (1977) obtained the following expressions for the excitation factors of upward and downward propagating waves in layer m within the reflection-zone:

$$\underline{f}_U^m = {}^m\mathcal{R}_D^n \left(I - {}^m\mathcal{R}_U^0 \, {}^m\mathcal{R}_D^n\right)^{-1} {}^0\mathcal{T}_D^m \, \underline{f}_D^0 \quad , \quad \text{and}$$

$$\underline{f}_D^m = \left(I - {}^m\mathcal{R}_U^0 \, {}^m\mathcal{R}_D^n\right)^{-1} {}^0\mathcal{T}_D^m \, \underline{f}_D^0 \quad . \tag{3.6.9}$$

These expressions (3.6.9) are also valid for an anisotropic reflection-zone when 3 x 3 coefficient submatrices and three-component excitation-factor vectors are used. The expressions contain an inverse matrix of the same form as that in (3.6.7), and its series expansion may be similarly truncated to give the response for direct waves only, or direct waves and the first reverberations. Kennett (1974) and Kennett & Kerry (1979) show how the expansion of the inverse term gives a physical representation of all the possible ray paths through the layer sequence.

Kennett & Kerry (1979) have extended Kennett's (1974) technique to the calculation of the complete response of a stratified halfspace, in terms of the reflection and transmission properties above and below the source. The free-surface effect may be accounted for above source and receiver, both of which may be buried in the halfspace. Kennett (1980) has applied the extended technique to the calculation of synthetic seismograms for local and regional events, which include surface-wave arrivals. Kerry (1981) has used the technique to calculate dispersion curves and synthetic seismograms for crustal and channel Rayleigh-wave modes. As stated by Kennett & Kerry (1980), the extended technique could also be adapted for anisotropic media, although this has not been attempted so far.

The anisotropic excitation factors are calculated for a range of horizontal slownesses covering the principal arrivals of interest on the seismogram (Fuchs & Müller 1971), and this is done for each frequency of interest in the source spectrum. The displacement spectra are obtained by substitution of the appropriate $f_j^m(p)$ in the layer containing the receiver into the equation (2.5.2). If the layer containing the receiver is

anisotropic, we cannot use the explicit expressions for $a_i^m(p)$ and q_j^m, in Table (2.1) and equation (2.3.6) respectively, which apply to isotropic media. We must calculate the $a_i^m(p)$ and q_j^m numerically from the elastic constants of the anisotropic medium, for each horizontal slowness value.

Fourier transformation of the displacement spectra gives the required synthetic seismograms. In the following section we describe the stages of the computational procedure which we use in practice to generate the synthetic seismograms, following the theory described above.

3.7 Computational procedure:

I - The receiver outside the reflection-zone

In the previous sections we have described how the isotropic reflectivity technique may be extended to anisotropic structures. The theory has been developed for the model illustrated in Fig.2.1, where the seismic source is located at the top of an isotropic layer overlying an anisotropic horizontally-layered reflection-zone. The computational procedure varies slightly, depending on whether the receiver is located above, or within the reflection-zone. We shall first describe the procedure for the case where the receiver lies in the isotropic top layer above the reflection-zone.

(a) Preliminary details

It is assumed that we are given an anisotropic layered model, of the type illustrated in Fig.2.1, and a number of receiver positions at differing horizontal distances from the source. It is also assumed that we have the physical parameters which are necessary to characterise each anisotropic layer, viz. density, elastic constants, and the orientation in

space of the sagittal plane with respect to the symmetry planes.

The equation which yields the displacement spectra (2.5.2) is an integral over horizontal wavenumber k. We change the variable of integration to the horizontal slowness (1/c), where c is the horizontal apparent velocity. Henceforth we shall use "slowness" when referring to horizontal slowness, unless otherwise stated. The limits of integration are chosen to be the slownesses which correspond to the minimum and maximum horizontal apparent velocities of the waves of interest (Fuchs & Müller 1971). Except where otherwise stated, we have used 320 slowness increments to span the integration window.

We have stated before that the response of the layered structure must be calculated at each slowness value for each frequency of interest in the source spectrum. The number of frequencies which are required will also be related to the time window for which each seismogram is to be computed. In the present work the number of frequencies is fixed at 256 and the principal frequency of the source function is fixed by the interval which is chosen for the time window. Following Kind & Müller (1975) we take the source spectrum to be

$$F(\omega) = 0.5\ (1 + \cos \pi\omega / \omega_o) \quad , \quad -\omega_o < \omega < \omega_o \qquad (3.7.1)$$

where ω_o is the circular cutoff frequency. The far field displacement is proportional to the derivative of the source function. It is approximately one sine period with a duration $T \simeq 15/\omega_o$. The acausality of this pulse is removed by a time shift (Kind & Müller 1975). The form of the source pulse is shown in Fig.3.1 for f_o ($= \omega_o/2\pi$) = 5.33 Hz, T = 0.45 sec.

(b) Computation of the interface coefficients

The basic elements of the iterative procedure described in section 3.6 are the matrices of upward and downward reflection and transmission

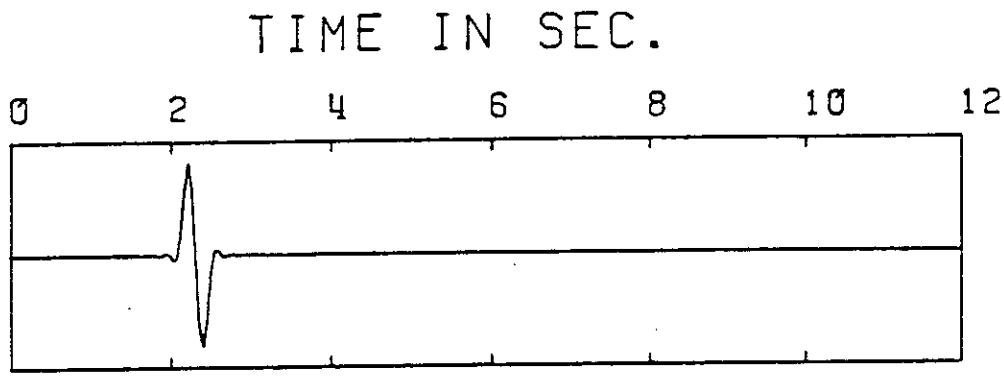

Figure 3.1 The waveform of the source pulse.

interface coefficients R_D, R_U, T_D, and T_U. The method which is used for their calculation is described in section 3.6. In the course of the calculation of R_D, R_U, T_D, and T_U for each interface between two media we also calculate the vertical slownesses q_p and the amplitude polarisation vectors $\underline{a}(p)$ for p = 1,2,..6, in each medium. The p = 1,2,3 correspond to the three possible downward waves qP, qS1, qS2, and p = 4,5,6 correspond to the upward propagating qP-, qS1- and qS2-waves respectively in each medium.

For each interface these calculations may be preceded by a rotation of the tensor of elastic constants for each anisotropic medium, depending on the orientation of the symmetry axes with respect to the sagittal plane. The calculations must be performed for each slowness value in the range of integration. For each slowness value we store the interface coefficient matrices and the $\underline{a}(p)$ and q_p for the medium on the lower side of the interface. The q_p are required for the vertical phasing factors in the iteration procedure, and the $\underline{a}(p)$ for a medium will be required in the computation of the displacements if the receiver is located in that medium. Storage of the $\underline{a}(p)$ for an anisotropic medium saves another lengthy calculation immediately before the integration step.

Interface coefficients for interface m, and the q_p^m and $\underline{a}^m(p)$ for layer m, are obtained and stored for each interface m = 1,2,..n in Fig.2.1.

(c) Iteration procedure

The next step is to perform the iteration procedure according to equation (3.6.7), in order to obtain the excitation factors given by (3.6.8) for the isotropic top layer above the reflection-zone.

The iteration procedure involves a frequency and path-dependent phasing of the cumulative response through the layered model. At this stage we set the time window of the required seismograms and thereby we

define the frequency spectrum of the source, for which the response for each slowness value is to be found. For each layer in the reflection-zone, we define its thickness and set a three-valued reverberation code. The three possible options for the layer reverberation response are:

(1) direct waves only

(2) direct waves and first multiples only

(3) complete response: direct waves and all multiples

In the present work, the complete response is obtained in each layer, unless otherwise stated.

It is convenient to perform the iteration procedure over all frequency values, for one slowness value, before moving on to the next slowness value. Nine upward excitation factors in layer 0, given by the matrix $^{0}\mathcal{R}_{D}^{n}$, are found by repeatedly substituting the interface coefficient matrices into equation (3.6.8), which is applied upward through the layer sequence. In this equation the frequency-dependent diagonal phasing matrices D_D and D_U for each layer involve the layer thickness, and the appropriate vertical slownesses q_p, p = 1,2,..6.

In practice, we calculate and store the matrix $^{0}\tilde{\mathcal{R}}_{D}^{n}$ for each combination of frequency and slowness values, rather than $^{0}\mathcal{R}_{D}^{n}$ which is phased to the top of layer 0. Very little computer time is involved in phasing the response $^{0}\tilde{\mathcal{R}}_{D}^{n}$ to the top of layer 0, by application of D_D^0 and D_U^0, when compared to the calculation of $^{0}\tilde{\mathcal{R}}_{D}^{n}$ by iteration over several anisotropic layers. We prefer to postpone this phasing to the next stage of the synthetic seismogram computation, since we then have the capability of altering the thickness of layer 0 without repeating the lengthy iteration procedure.

The iteration procedure is the most expensive part of the synthetic seismogram computation in terms of computer time. This is due to the large number of operations which must be performed on the complex elements of the

3 x 3 matrices which are described in section (3.6). These operations must be performed for each layer in the sequence of layers constituting the model. They must also be performed for each slowness value and for each frequency value in the range for which the response of the structure, as represented by ${}^{0}\mathcal{R}_{D}^{n}$, is calculated. Only simple structures which involve two or three layers above a halfspace are used at present, since structures involving a larger number of layers are too expensive for repeated computer runs.

(d) Construction and re-ordering of the plane wave component displacements

In this stage of the computation we construct the integrand in (2.5.2) with $m = 0$ for specified values of $j = 1,2,3$ and $p = 4,5,6$. That is, for a specified type of source, generating a specified type of wave, we calculate the integrands for waves of a specified type reflected upwards to the receiver in the top layer. Multiplication by the distance-dependent Bessel function in the integrand is deferred until immediately before the integration, which is performed in the next stage of computation.

For the iteration procedure, it was found convenient to calculate the excitation factors for all frequencies and slownesses in the order (frequency, slowness). The integration procedure will require the integrand terms in the order (slowness, frequency), so the integrand terms are re-ordered as they are calculated from the excitation factors which form the input to this stage. The source function S_j in (2.5.2) has been given in Table 2.2 for the three possible wave-types generated by various types of source.

For a receiver located at $(x_1, 0, 0)$ in Fig.2.1, immediately beneath the surface of the top layer, we have the option of considering or neglecting reflections at the free surface. If we neglect the free-surface

effect, the components $a_i(p)$ of the polarization vector for the specified upward wave at the receiver are given by the appropriate values in Table 2.1. Free-surface reflections at the receiver are included if we substitute the appropriate conversion vectors given by Červený & Ravindra (1971), p.67, for the $a_i(p)$ in (2.5.2). It is possible, of course, to calculate the integrands in (2.5.2) for all combinations of source and received wave-types, and to sum and store them in a single pass through this computational stage. Then the composite seismograms of all arrivals can be produced by a single integration and Fourier transformation for each component. In these early stages of the development of the anisotropic reflectivity technique we have found it easier to identify anomalous arrivals by forming separate seismograms for each type of source and receiver wave-type. The composite seismogram for each component is then obtained by summing the individual seismograms.

(e) Integration, transformation and plotting

We perform this stage for each required component of the received wave displacements, according to (2.5.2). The integrands which were formed in the previous stage are multiplied by the Bessel function $J_o(kx_1)$ at each slowness value. In this formulation we use the far field approximation:

$$J_o(kx_1) \simeq 1/(2\pi kx_1)^{\frac{1}{2}}.\exp\,[-i(kx_1 - \pi/4)] \quad \text{for } kx_1 >> 0 \qquad (3.7.2)$$

The numerical integration over slowness is performed by the trapezoidal rule, for each frequency value. The resulting response spectrum is convolved with the source spectrum in (3.7.1), and a Fast Fourier transformation to the time domain yields the seismogram. The integration and transformation procedure is performed for each horizontal distance

range at which a seismogram is required. The seismograms for a range of distances are usually plotted in the form of reduced time-distance seismic sections, over the time window which was defined in the iteration step. Many examples of such seismic sections will be given in chapters 5 and 6.

When the difference in travel-time of the fastest and slowest arrivals is larger than the time window for which the seismograms have been computed, one or both of these arrivals will be folded round the ends of the time window. This effect is known as time-aliasing. It may be mitigated to some extent by a careful choice of reducing velocity. Kind (1979) has shown how time-aliasing may be eliminated if the plane wave responses are calculated with a variable frequency spacing. However, in that case the usual fast Fourier methods cannot be used to transform the spectrum into the time domain.

(f) Construction of composite seismograms

Once we have constructed all the individual seismograms which contain all the arrivals of interest for a particular receiver component, it is a simple step to sum them within the appropriate overall time window. Travel time curves may be calculated for specified wave arrivals for any model, according to methods described in chapter 4. When drawn on individual or composite seismograms, these curves aid the identification of particular phases, and their use will be illustrated in chapter 5.

3.8 Computational procedure:
II - The receiver within the reflection-zone

When the receiver lies within the reflection-zone, rather than outside it, the calculation procedure becomes more complicated. For example, we must

also consider downward waves, as well as upward waves, incident on the receiver. From equations (3.6.9), which give the upward and downward excitation factors in the receiver layer m, it is clear that three 3 x 3 matrices ${}^{m}\mathcal{R}_{D}^{n}$, ${}^{m}\mathcal{R}_{U}^{0}$, and ${}^{0}\mathcal{T}_{D}^{m}$ must be calculated for each combination of slowness and frequency values. This involves three separate iteration procedures, and will be extremely time-consuming, even for only a few layers on either side of the receiver layer.

The iteration procedure can be simplified and considerably shortened in computer time if we use a simple symmetrical structure such as that shown in Fig.3.2. In this model the same solid isotropic material comprises the upper and lower halfspaces, and the receiver is located in the central anisotropic layer. The layers 1 and 3 on either side of the anisotropic layer are formed of an identical isotropic medium which is different to that constituting the halfspaces. It is easily seen that the symmetry gives

$${}^{2}\tilde{\mathcal{R}}_{D}^{4} = {}^{2}\mathcal{R}_{U}^{0}.$$

In this case it is only necessary to perform two iteration procedures instead of three, for once ${}^{2}\mathcal{R}_{U}^{0}$ has been calculated, ${}^{2}\mathcal{R}_{D}^{4}$ is quickly given by application of equation (3.6.6). An application of this simple model is described in chapter 6, where we calculate synthetic seismograms at a receiver located in cracked channel.

When the receiver lies within an anisotropic reflection-zone, problems arise with the calculation and storage of the terms which are required to form the integrand in equation (2.5.2). When the receiver lay in an isotropic medium, the vertical slownesses q_{p}^{m} and the amplitude polarization factors $a_{i}^{m}(p)$ could be given by simple expressions. However when the receiver lies in an anisotropic medium, the q_{p}^{m} and $a_{i}^{m}(p)$ must be

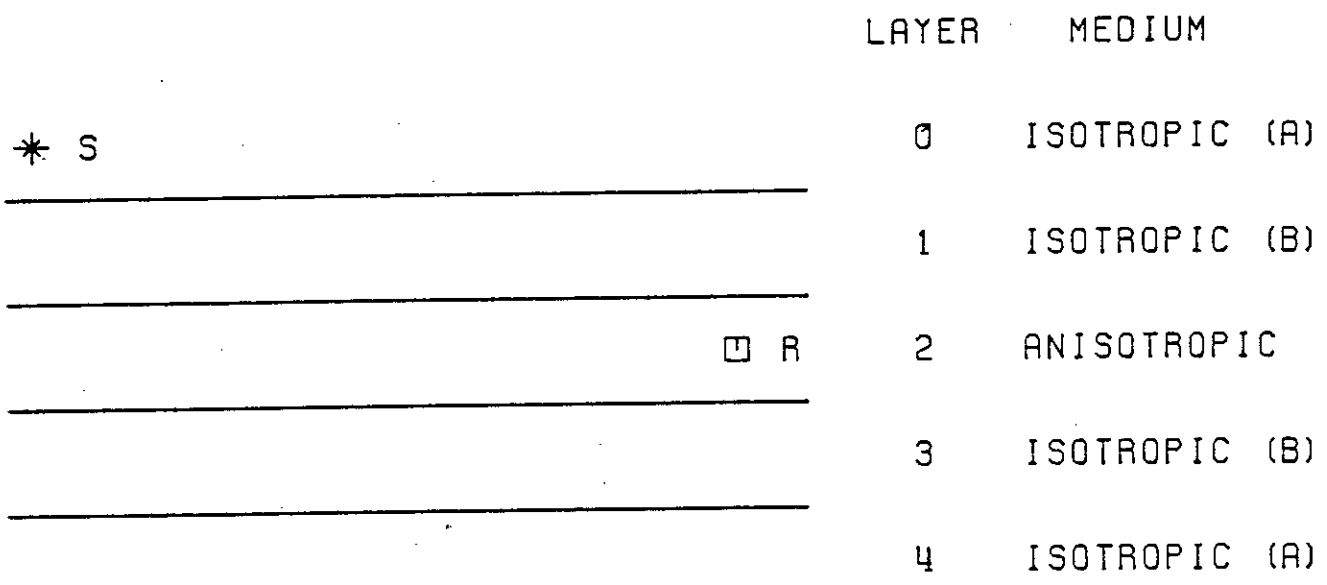

Figure 3.2 The configuration of the reflection zone for a simple three-layer model which is symmetrical about the layer containing the receiver.

calculated numerically. They are calculated and stored in the computation of the interface coefficients, as noted in section 3.7(b).

When the receiver lay outwith the reflection-zone, only three (upward) excitation factors for each of the three possible source wave-types and each slowness/frequency combination had to be stored. For a receiver within the reflection-zone, we must calculate six excitation factors, which correspond to the six possible waves in the receiver layer - ie qP, qS1 and qS2 propagating upwards and downwards.

In order to minimise storage and tape handling in the computer operations, the calculation of the three components of total plane wave displacement for each of the three possible received wave-types is performed in the same step as the calculation of the excitation factors. When the receiver lay outside the reflection-zone, the plane wave displacements were calculated in a subsequent step when the integrand in equation (2.5.2) was formed and re-ordered with respect to slowness and frequency, as in section 3.7(d).

Each plane wave displacement component which is formed is given by the product

$$P = f_j^m(p).a_i^m(p).\exp[-i\omega q_p^m(x_3 - d_m)]$$

in the integrand of (2.5.2). It is seen from this expression that we must define the source wave-type j (j = 1,2,3 corresponding to P-, SV- and SH-waves respectively) and the depth of the receiver in the receiver layer, $(x_3 - d_m)$, at this stage of the computation.

Thus at the conclusion of this computational step we store the sum of the upward and downward plane wave displacements for each component and for each of the three possible received wave-types, for each slowness/frequency combination. The storage requirement remains the same as at end of the

iteration procedure in section 3.7(c). However, in the above procedure, the excitation coefficients and the plane wave displacement components must be re-calculated for a different type of source wave, or if the receiver is moved to a different depth in the reflection-zone.

After the calculation and storage of the plane wave displacement components, we calculate the integrand in (2.5.2) for a specified type of received wave and a specified type of source. The source function S_j is given in Table 2.2. Multiplication by the distance-dependent Bessel function in the integrand is deferred to the integration step. As in section 3.7(d) the integrands are re-ordered with respect to slowness and frequency, before they are stored prior to the integration step.

Integration over slowness, Fourier transformation, and plotting of the synthetic seismograms is performed in the same step as that described in section 3.7(e). Seismograms of different wave arrivals may also be summed, as described in 3.7(f).

3.9 A test of the computational method

After the computer programs for the anisotropic reflectivity technique had been written, the computational procedure required testing. Although all previous reflectivity programs assumed that the model structure was isotropic, it was still possible to arrange a comparison with an independent computational procedure. This was done by constructing a structure which included a transversely isotropic medium with a horizontal axis of symmetry - model 1A in Fig.5.1(a).

For the purposes of this section it is sufficient to state that when the axis of symmetry is rotated 90° about the vertical axis, the resulting model 1A-90 becomes effectively isotropic and it is equivalent to the isotropic model 1A-ISOT which is parameterised in Table 3.1. A standard

Table 3.1 Velocity,density-depth distribution for isotropic model 1A-ISOT

Depth (km.)	P velocity (km/s)	SV velocity (km/s)	SH velocity (km/s)	Density (g/cm^3)
0	6.0	3.464	3.464	2.8
25	6.0	3.464	3.464	2.8
25	7.731	4.445	4.522	3.324
40	7.731	4.445	4.522	3.324
40	8.2	4.734	4.734	3.324

isotropic reflectivity program may be used to construct synthetic seismograms for the isotropic model; in this work we used a program kindly supplied by Prof. Karl Fuchs, which employs the computational methods of Kind (1976). This program did not include an option for the free surface effect, and therefore the effect was neglected in the computations.

Synthetic seismograms were constructed for P- and SV-wave arrivals at the receiver R from an explosive source located at S (Fig.5.1). In Fig.3.3 we present profiles of vertical and radial component seismograms which have been computed by the anisotropic reflectivity technique for model 1A-90, and by the isotropic reflectivity technique for model 1A-ISOT. It is easily seen that for each component, the profiles for models 1A-90 and 1A-ISOT are identical, although they have been generated by different computational methods. This provides a simple check on the computational procedure of the anisotropic reflectivity technique.

There is an approximation involved in the calculation of synthetic seismograms for anisotropic layered media by the formulation described in chapters 2 and 3. The approximation applies when the sagittal plane does not lie in a plane of crystal symmetry. We use the final section of this chapter to describe this approximation.

3.10 The approximation involved in anisotropic reflectivity theory

Waves propagating in anisotropic media may have a component of the energy propagating parallel to the surface of constant phase. This means that in a horizontally stratified halfspace containing isotropic and anisotropic layers, a ray of seismic energy may deviate from the vertical plane of incidence during propagation through an anisotropic layer, but will return to a path parallel to the original incidence plane on entering an isotropic layer. This happens because the reaction at an interface is controlled by

Figure 3.3 A comparison of seismograms generated by the anisotropic reflectivity technique and an independent isotropic reflectivity technique, for models 1A-90 and 1A-ISOT respectively. These models, which are described in the text, are equivalent for the given orientation of the anisotropic material in model 1A-90. Vertical (Z) and radial (R) component seismograms are shown.

(a) anisotropic reflectivity technique, model 1A-90

(b) isotropic reflectivity technique, model 1A-ISOT

It is seen that the seismograms for the corresponding components for each model are identical.

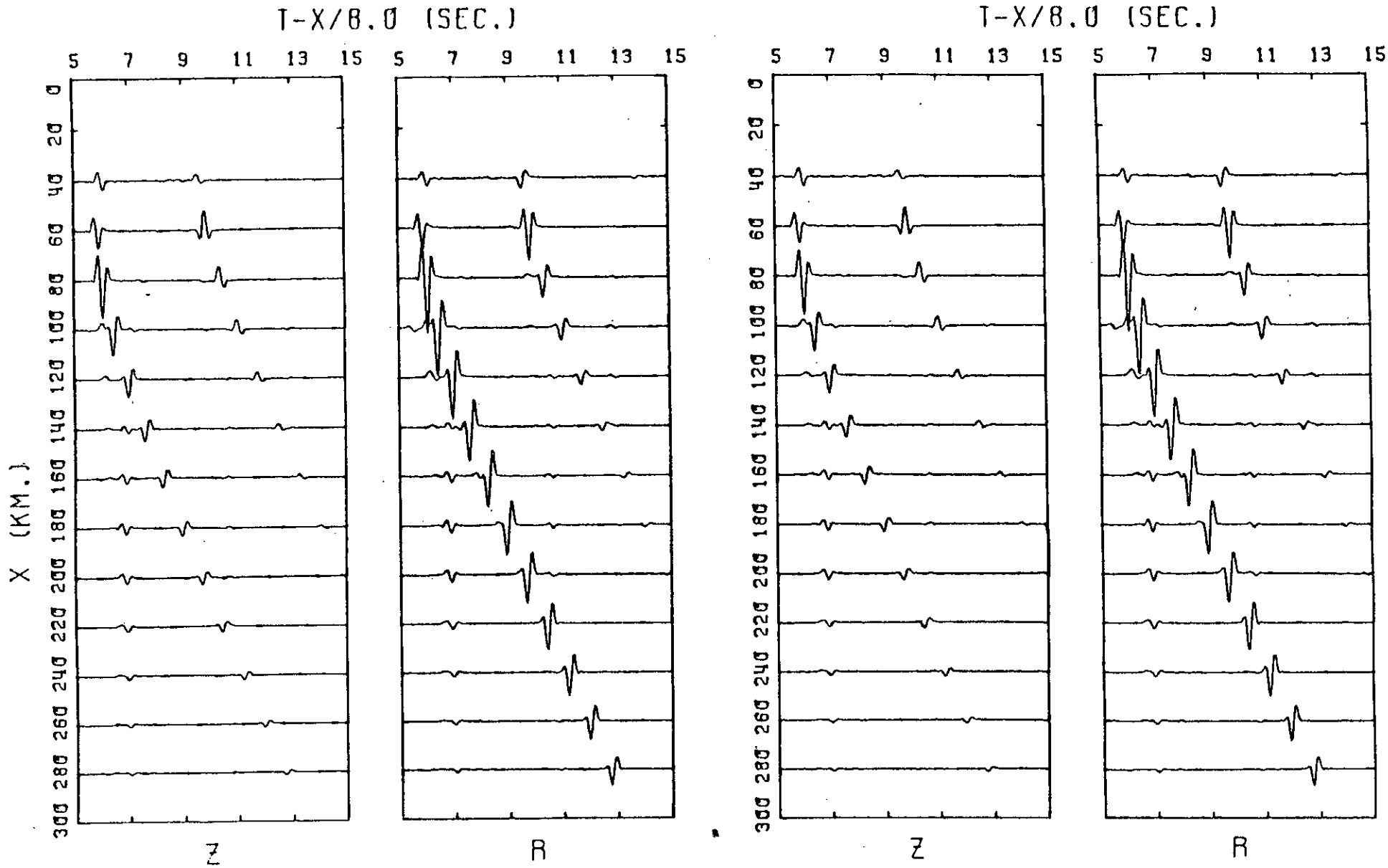
T-X/8.0 (SEC.)
5 7 9 11 13 15
X (KM.)
0 20 40 60 80 100 120 140 160 180 200 220 240 260 280 300
Z
R
(a)
T-X/8.0 (SEC.)
5 7 9 11 13 15
0 20 40 60 80 100 120 140 160 180 200 220 240 260 280 300
Z
R
(b)

the lines of constant phase and the phase velocity, whereas the energy is controlled by the group velocity, which may deviate up to 30° in direction for some directions of propagation in some very strongly anisotropic solids (Crampin et al. 1982), although usually the deviation is much less. This phenomenon of anisotropic propagation will be discussed further in the following chapter.

The reflectivity technique, as set out above, determines synthetic seismograms only from waves propagating from the source in a vertical section of the focal sphere, and assumes all the energy travels in the sagittal plane. A real seismogram in an anisotropic structure will be generated by waves which may leave the source in directions tracing out a wavy line on the focal sphere. The wavy line may have multiple points. The only occasion when real seismograms would be derived from waves leaving the focal sphere in a vertical section (ie. the sagittal plane) is when propagation is in a transversely isotropic layered structure. In this thesis, a medium is deemed to be transversely isotropic if it possesses hexagonal anisotropic symmetry with a vertical axis of symmetry.

A reflectivity technique for the generation of true seismograms in stratified generally-anisotropic media would require an extremely complex integration of the displacements of plane waves propagating in three dimensions. In particular, the horizontal wavenumber would become a vector quantity, and the source function, excitation factors, polarization factors and vertical slownesses would all become functions of this vector quantity. In principle, the real seismogram may be calculated by a further integration over the transverse component of the wavenumber vector. This has not yet been done because it would greatly increase the computing time of an already lengthy computation. We restrict the use of the technique to weakly anisotropic media and we expect only minor differences from the real seismograms.

3.11 Conclusion

When seismic waves propagate through anisotropic media, the propagation will possess anomalous characteristics which do not occur for propagation through isotropic media. Synthetic seismograms probably provide the most effective means of investigating the dynamic characteristics of the anomalous wave behaviour. Keith & Crampin (1977c) have constructed synthetic seismograms of plane waves propagating through a multilayered anisotropic structure with horizontal stratification. However, when applied to the interpretation of observed seismograms, plane wave seismograms can only aid the study of teleseismic arrivals. The investigation of most anisotropic regions of interest in the crust and upper-mantle requires the construction of seismograms of curved wavefronts from a point-source.

The original reflectivity technique, as developed by Fuchs & Müller (1971), permits the calculation of synthetic seismograms of waves from a point-source which have been reflected from a horizontally-stratified, isotropic halfspace. In chapters 2 and 3 we have shown how this technique can be extended to permit the inclusion of weakly anisotropic layers in the reflecting halfspace.

We have not attempted to derive a rigorous expression for the displacement of a curved wavefront in a horizontally-stratified anisotropic halfspace. The expression which has been derived is an approximation which applies to weakly anisotropic media, at distances from the source which are large compared with the wavelength of the source pulse. With these assumptions, it is possible to substitute anisotropic plane wave displacements in the integration over plane wave displacements which yields

the displacement of a curved wavefront. Calculation of the plane wave displacement responses for anisotropic media is not a problem, since the computation can be performed by propagator matrix methods which Crampin (1970) has extended to anisotropic media. Direct calculation of the propagator matrices can lead to numerical inaccuracy. Kennett (1974) developed a convenient iteration technique which was based on the propagator matrix technique, and which avoids the inaccuracy problem. The technique efficiently computes the responses in multilayered isotropic media. In the present work, we have extended this iterative technique to multilayered anisotropic media.

We have shown how the synthetic seismograms are computed, using two particular configurations of source and receiver position with respect to the multi-layered anisotropic reflection-zone. In each case, we have avoided difficulties associated with the description of the source function in an anisotropic reflection-zone by placing the source outside the reflection-zone and in an isotropic medium. In the first case we considered, the receiver lay outside the reflection-zone and in the same layer as the source. The free surface effect could be included at a receiver immediately below the free surface, but not at the source. This configuration will be used in anisotropic upper-mantle studies in chapter 5. We also showed how synthetic seismograms could be calculated at a receiver located inside the reflection-zone. Expressions for the plane-wave response in an anisotropic layer within the reflection-zone were obtained by extending the work of Stephen (1977) to anisotropic media. A practical application of these expressions will be described in chapter 6.

CHAPTER 4

CALCULATION OF TRAVEL-TIMES IN ANISOTROPIC LAYERED MEDIA

4.1 Introduction

In the construction and interpretation of synthetic seismograms, it is very useful to have a means of computing the arrival time of each possible wave arrival at the receiver for a specified distance range. Before a seismic section of synthetic seismograms is constructed, the arrival times of the principal waves expected at the receiver are required in order to set the time window of the seismic section. At the interpretation stage it is often difficult to identify all the observed arrivals. This is due to the large number of possible multiples and converted waves which may propagate, even in a comparatively simple layered structure. Interpretation is simplified if travel-time curves corresponding to the expected wave arrivals are available.

The calculation of wave travel-times in a horizontally layered structure composed of isotropic media is quite straightforward. Many workers have developed computer programs for the calculation and plotting of travel time-distance graphs for specified ray paths in isotropic structures. The technique which is most often used is based on the calculation of the travel-time and horizontal distance travelled for each layer segment of the overall ray path for a particular propagation vector in the source layer. Each propagation vector is characterised by its horizontal phase velocity. The times and horizontal distances corresponding to each segment are summed over the whole ray path, which gives a point on the time-distance graph. The complete travel-time graph

is obtained by performing this procedure for a range of horizontal phase velocity values. The maximum value in the range usually corresponds to vertical incidence, while the minimum value approaches the minimum wave-velocity for the given ray path. A line joining a sufficient number of time-distance co-ordinates defines a smooth travel-time curve.

In anisotropic media, the phase velocity, which governs the reflection and transmission characteristics at an interface, is not in general identical to the group velocity, which governs the velocity of energy propagation and therefore the travel-time (Crampin 1977a). An additional step is required in the travel-time calculation, involving the calculation of the group velocity equivalent to a given propagation vector in each anisotropic layer.

In this chapter we show how seismic wave travel-times may be calculated for stratified structures with different anisotropic symmetries. We describe how the group velocities for a given propagation vector are calculated, and the approximations involved. We then outline the computational procedure. The technique is used in later chapters to aid the interpretation of synthetic seismograms.

In the final section of this chapter we describe a different application of this technique, with relevance to the processing of common-depth-point reflection data. This type of data is routinely obtained in the course of seismic prospecting for oil over sedimentary beds which are frequently transversely isotropic. The detection of potential oil reservoirs depends on very careful processing of the observed data, in which account should be taken of any anisotropy in the beds. We shall construct travel-time curves which correspond to common depth point gathers for two different transversely isotropic sedimentary structures, in order to illustrate the effect of the anisotropy.

4.2 Phase and group velocities in anisotropic media

The kinematic group velocity $\underline{u}$ is given by the gradient of the frequency with respect to the wavenumber, in the expression

$$\underline{u} = (\partial\omega/\partial k_1, \partial\omega/\partial k_2, \partial\omega/\partial k_3)^T \quad , \tag{4.2.1}$$

(Crampin 1977a). For plane wave propagation in the x_1 direction we have $\omega = ck_1$, where c is the horizontal apparent velocity. The group velocity in an anisotropic medium is then

$$\underline{u} = (c, \partial\omega/\partial k_2, \partial\omega/\partial k_3)^T . \tag{4.2.2}$$

In addition to the component along the propagation vector $\underline{x}_1$, it is seen that there is also a component perpendicular to the propagation vector. The absolute value of the group velocity will always be greater or equal to the phase velocity.

The relationship between the phase velocity vector $\underline{v}_p$ and the group velocity vector $\underline{v}_g$ in an anisotropic medium is shown in Fig.4.1. The propagation vector incident on the anisotropic medium lies in the plane $x_2 = 0$, in the direction of $\underline{v}_p$. The angle ϕ measures the deviation of the group velocity direction from the plane of propagation. Keith and Crampin (1977a) and Crampin *et al.*(1982) have computed the phase and group velocity vectors for a number of anisotropic media. Crampin *et al.* found that the propagation of energy may diverge out of the incident plane by as much as 30^o for some directions of propagation in some very strongly anisotropic materials.

We now consider a wave propagating through a horizontally layered structure consisting of isotropic and anisotropic media. While the

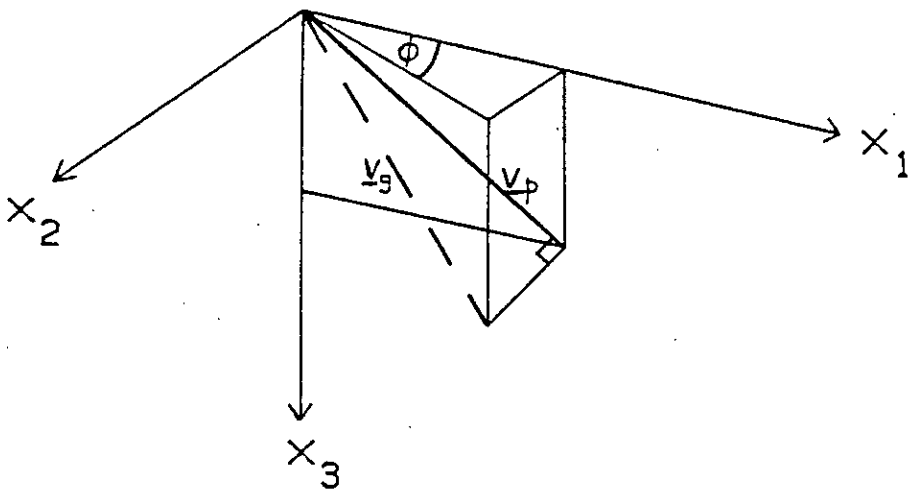

Figure 4.1 Schematic representation of the relationship between the phase-velocity vector $\underline{v}_p$ and the group-velocity vector $\underline{v}_g$. The angle ϕ gives the direction of the projection of $\underline{v}_g$ on the plane $x_3 = 0$.

propagation characteristics at interfaces are determined by the phase velocity, the propagation of energy through a layer is described by the group velocity. The propagation of energy at the group velocity diverges from the propagation vector in each anisotropic medium. The divergence may be not only in the vertical sagittal plane, for propagation in a symmetry plane, but also perpendicular to the sagittal plane for propagation at more general orientations.

Consider the propagation of a P-wave ray from a point A in an isotropic layer upward through an anisotropic layer to a point B in another isotropic layer (Fig.4.2(a)). We follow the description of the propagation given by Crampin (1977a) but consider only one of nine possible arrivals. The representation of a plane wave by a ray is not strictly realistic (Crampin 1977a), but it may be used to show the effect of the divergence of the energy propagation from the plane of incidence.

The plan view (Fig.4.2(b)) of the model in Fig.4.2(a) shows how incident energy in the sagittal plane deviates away from this plane in the anisotropic medium, but returns to propagating parallel to this plane on re-entering an isotropic medium . The wave-energy initially propagating in the incident plane does not propagate to B, but out of the incident plane to B'. We would need to consider an incident ray out of the sagittal plane in order to determine the travel-time of wave-energy from A to B, as shown in Fig.4.2(b). Thus the determination of exact travel-times for a general orientation of an anisotropic medium is rather complicated.

The deviation of wave-energy from the sagittal plane is significant for strongly anisotropic media such as olivine (Keith & Crampin 1977a). However, in the present work we shall only calculate travel-times for general orientations of an anisotropic material when the anisotropy is weak. Travel-times are calculated by using the component of the group velocity vector in the sagittal plane alone. In chapter 5 it will be seen

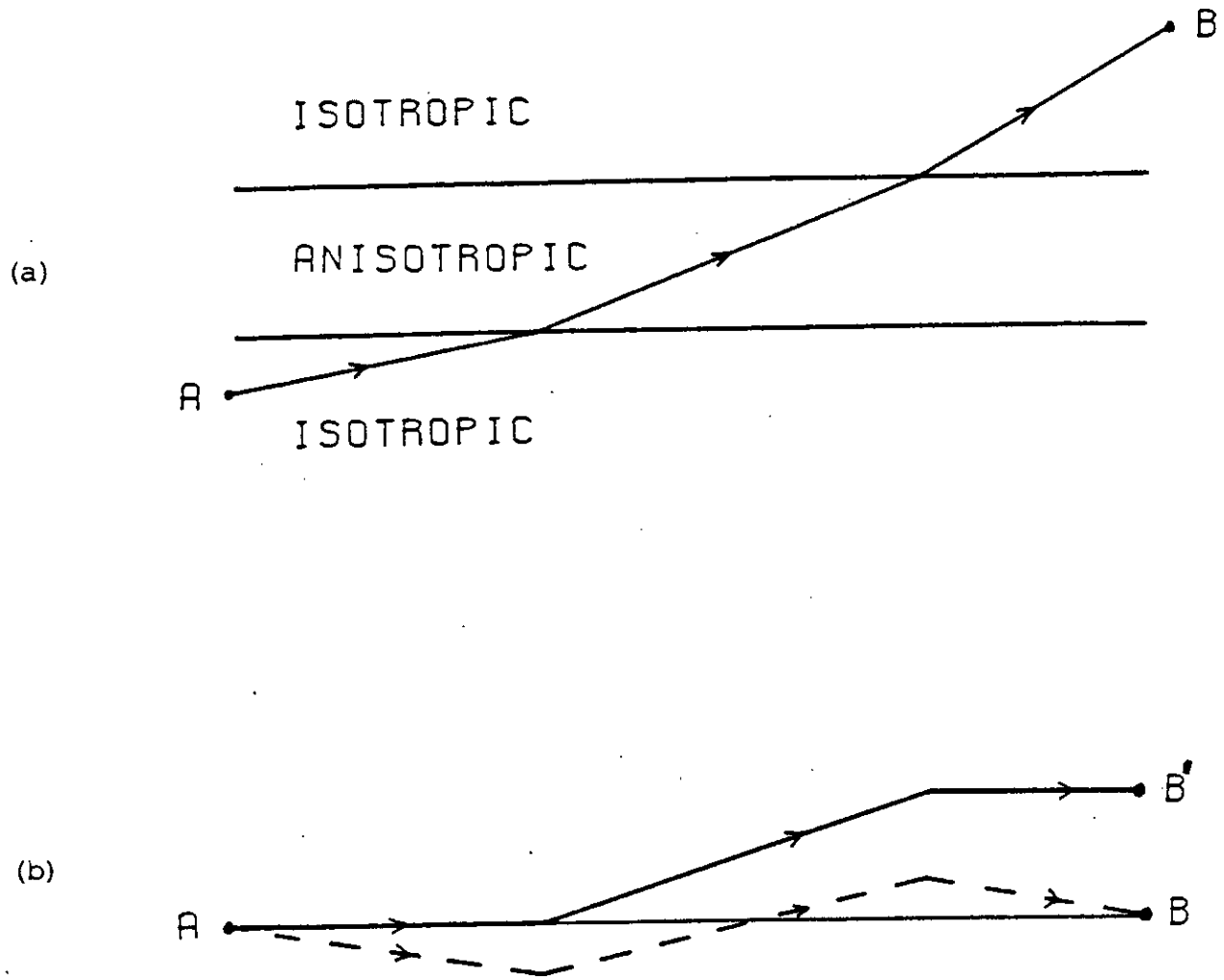

Figure 4.2 Schematic illustration of a ray path through a plane horizontal layer possessing general anisotropic symmetry, where the sagittal plane is not a plane of symmetry.

(a) Sectional view.

(b) Plan view.

In order that the wave-energy may propagate from A to B, rather than B', the propagation vector at A must diverge from the sagittal plane.

that these travel-times are sufficiently good approximations to aid the interpretation of the synthetic seismograms. No approximation is involved when the sagittal plane is a symmetry plane. Then the group velocity vector diverges from the propagation vector but remains in the sagittal plane. Thus exact travel-times can be calculated in transversely isotropic media.

4.3 Computational Procedure

Briefly, the method involves the calculation and summation of the travel-times and horizontal distance for each segment of the ray path over a range of horizontal apparent velocities which will cover the desired distance range.

The source and receiver may be positioned at any point within the horizontally layered structure. The media comprising the layers may be isotropic, or anisotropic, or they may have a constant velocity gradient between the values at the top and bottom of the layer. Each anisotropic medium is characterised by an index which refers to a particular set of phase velocity - group velocity tables. The structure of each set of tables is shown in Table 4.1 for a particular example of a transversely isotropic medium - Colorado oil shale. (This medium is used later in this chapter, when we calculate travel-times in anisotropic oil-bearing structures).

The first table in each set gives the phase velocities for each of the three possible wave-types qP, qS1, qS2 for a range of directions of the propagation vector in the sagittal plane from 0° to 90°, with respect to the vertical axis. The second table gives the amplitude and direction of the group velocity vector in the sagittal plane for each wave-type, for each propagation vector defined in the first part of the table. These

Table 4.1 Extract from phase velocity/group velocity tables which give the amplitude and direction of the group velocity vectors which correspond to a range of phase velocity (propagation) vectors.

COLORADO OIL SHALE: PHASE-VELOCITY SURFACE

GAM (Degrees)	QP km/s	QS2 km/s	QS1 km/s
0.000	4.235	2.541	2.541
2.000	4.235	2.541	2.542
4.000	4.237	2.543	2.544
6.000	4.239	2.545	2.549
8.000	4.243	2.548	2.554
10.000	4.248	2.552	2.562
12.000	4.254	2.557	2.570
14.000	4.261	2.562	2.579
16.000	4.269	2.568	2.589
⋮	⋮	⋮	⋮
76.000	4.956	2.864	2.566
78.000	4.970	2.869	2.559
80.000	4.982	2.873	2.554
82.000	4.992	2.877	2.549
84.000	5.000	2.880	2.546
86.000	5.006	2.882	2.543
88.000	5.009	2.883	2.541
90.000	5.011	2.883	2.541

COLORADO OIL SHALE: WAVE SURFACE (GROUP VELOCITY VALUES)

QP		QS2		QS1	
GAM	VEL.	GAM	VEL.	GAM	VEL.
0.00	4.235	0.00	2.541	0.00	2.541
2.39	4.235	2.57	2.541	3.12	2.542
4.79	4.237	5.14	2.543	6.22	2.546
7.20	4.240	7.71	2.546	9.24	2.553
9.63	4.245	10.26	2.550	12.18	2.561
12.07	4.250	12.79	2.555	15.00	2.571
14.53	4.258	15.31	2.561	17.69	2.583
17.02	4.267	17.80	2.568	20.22	2.595
19.53	4.278	20.26	2.576	22.59	2.607
⋮	⋮	⋮	⋮	⋮	⋮
81.07	4.975	79.04	2.868	71.70	2.573
82.39	4.985	80.63	2.872	74.19	2.565
83.68	4.993	82.20	2.875	76.74	2.558
84.97	4.999	83.77	2.878	79.33	2.552
86.24	5.004	85.33	2.880	81.96	2.547
87.50	5.008	86.89	2.882	84.62	2.544
88.75	5.010	88.45	2.883	87.31	2.542
90.00	5.011	90.00	2.883	90.00	2.541

tables may be calculated for symmetry planes of media with hexagonal symmetry from the exact equations of White (1965). In these planes the wave-types qS1 and qS2 will be exactly equivalent to SV- and SH-waves. McGonigle & Crampin (1982) have recently described a computational method for evaluating the phase and group velocity surfaces for more general anisotropic symmetries.

Each ray path is characterised by maximum and minimum horizontal apparent velocity values defining the range of apparent velocities for which travel-times are to be found. The velocity range is chosen so that arrivals corresponding to the specified ray path appear over the desired distance range. The ray path is described in terms of its constituent segments, starting with the segment in the source layer and ending with the segment in the receiver layer. The segments themselves are defined by their layer number, wave-type, and direction of propagation (up or down).

The following procedure is followed for each apparent velocity value for a given ray path:

Each segment is taken in turn, starting with the segment in the source layer. In an isotropic layer the horizontal distance travelled, d, and the travel-time, t, are easily calculated from the vertical distance travelled, h, the wave (group) velocity in the layer, v, and the horizontal apparent velocity, c. The wave-energy propagates at the angle of incidence θ, where $\sin\theta = v/c$. Then $t = h/(v\cos\theta)$ and $d = h.\tan\theta$. If the layer has a velocity gradient, then an algorithm given by Červený & Ravindra (1971), p.84, is used to calculate d and t.

For an anisotropic medium, the appropriate set of phase velocity - group velocity tables is used. In general the given apparent velocity value c will correspond to a propagation vector with an angle of incidence θ, which lies between two of the given angle values (θ_m, θ_{m+1}) in the

phase velocity table. These angle values correspond to the apparent velocities c_m, c_{m+1} respectively, where $c_{m+1} < c < c_m$. The group velocity and its angle of incidence corresponding to c is obtained by simple linear interpolation between the group velocities and angles of incidence defined by c_m and c_{m+1}. Strictly speaking, a non-linear interpolation should be used. However, if the tables are given for sufficiently small intervals of phase velocity angle of incidence, $\Delta\theta \leqslant 2^{\circ}$, then a good approximation is obtained. Once the group velocity and its angle of incidence has been found, then the values of d and t are found by the equations given above for the isotropic case.

The horizontal distances and the travel-times are summed over all segments of the ray path to give a point on the travel-time vs. distance curve for that arrival. Economies in computing are possible if the ray path is symmetrical about its central point, or if a ray crosses a layer more than once. Special procedures are invoked if a ray bottoms in a layer with a velocity gradient, or if a travel-time graph for a head-wave is desired, when only one apparent velocity value (that of the head-wave) is required to define the graph.

When followed for the complete range of specified apparent velocity values, the above procedure defines a series of points through which a travel-time curve may be drawn for the given ray path. The travel-time and distance coordinates for each ray path are plotted and/or stored for input to other programs. The travel-times are usually stored and plotted as reduced travel-time curves when they are used to aid interpretation of seismic sections formed from synthetic or recorded seismograms. Examples of reduced travel-time curves are given in later chapters.

We shall describe another practical use of the technique for the calculation of travel-times in anisotropic structures. Prospecting for oil

commonly takes place by seismic methods over sedimentary layered rock structures which are transversely isotropic. In the next section we show how the anisotropic travel-time calculation procedure may be applied to the processing and interpretation of the common-depth-point gathers which are commonly obtained in the course of such work.

4.4

CDP gather arrival times in transversely isotropic structures: introduction

When prospecting for oil, the common depth point (CDP) method is commonly used during the execution of seismic reflection surveys. The principles and procedures of the CDP method are well described in the literature, eg. Waters (1978), but a simple model will serve to illustrate them. Fig.4.3 illustrates the shot-receiver configuration or "spread" which allows the signals to be reflected from a common depth point. The travel time of each signal varies from record to record. The difference between the actual two-way travel time of each signal and the corresponding two-way vertical time under the centrepoint of the spread is termed the normal moveout (NMO). The NMO is obtained for each member of the set of signals, which is collectively termed a CDP "gather". After the observed travel-times have been corrected for the NMO, the signals are stacked to give an enhanced primary reflection which is applicable to the centrepoint of the spread. The improvement in quality of the reflection signal, which is the object of the CDP method, is thus very dependent on the accuracy of the NMO correction.

Computation of the NMO is fairly straightforward for homogeneous layered isotropic media. However it is common in oil prospecting for reflection surveys to take place over sedimentary beds which are transversely isotropic. There are two principal explanations for such

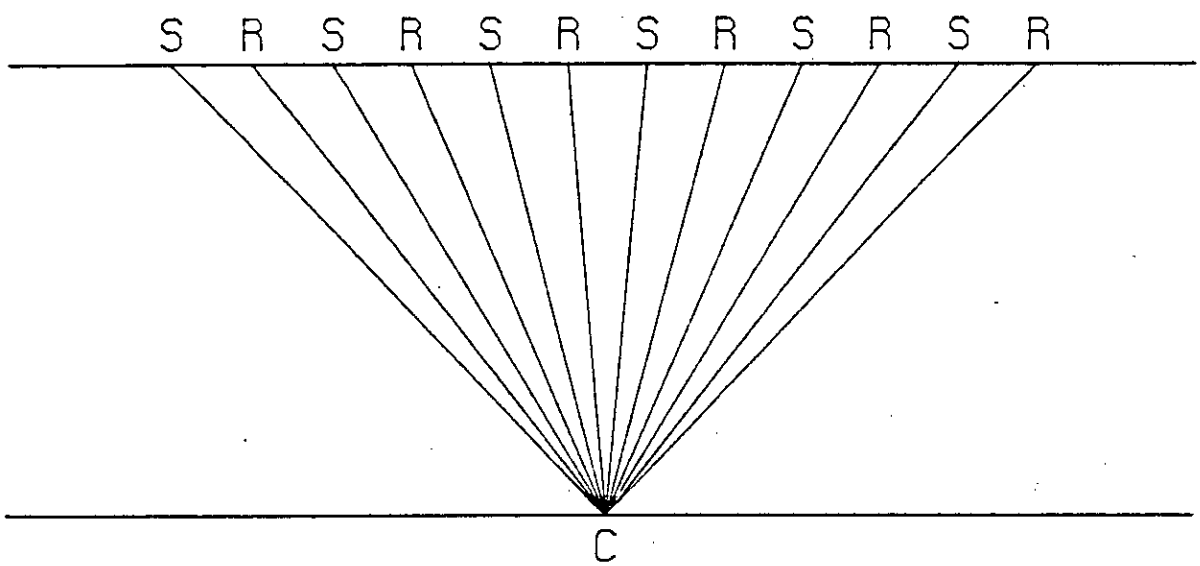

Figure 4.3 Ray paths of reflections at a common-depth-point C for a 12-point spread of shotpoints (S) and receivers (R).

anisotropy. It may be due to an intrinsic anisotropy of the media in the sedimentary sequence, or alternatively, a sequence of thin isotropic beds becomes equivalent to a homogeneous transversely isotropic medium for wavelengths which are much longer than the bed thicknesses (Postma 1955, Backus 1962).

The wave-velocities will vary between the different ray paths in Fig.4.3 and the CDP gather travel-time curves will no longer be the exact hyperbolae which they are in isotropic media. It is still possible to calculate the NMO for transversely isotropic layers, but the elastic properties of the anisotropic materials must be quantified as accurately as possible.

In a study on P-, SV- and SH-wave velocities in near surface formations, White & Sengbush (1953) showed that anisotropy is more apparent for shear-waves than for compressional-waves. The increasing use of shear-wave data in seismic prospecting will lead exploration geophysicists to pay more attention to the effect of anisotropy on the wave-velocities which are used to determine the NMO corrections.

The wave-velocity surface in a transversely isotropic medium has been approximated by an ellipsoid of revolution (Levin 1978), but by no means all transversely isotropic media can be treated in this way. Levin (1979) presents some numerical examples for which transverse isotropy does not imply an elliptical wave-surface, while Krey & Helbig (1956) and Lucas, O'Brien & Thomas (1980) illustrate some of the errors implicit in assuming the wave-surface to be an ellipsoid. If the elastic constants of the anisotropic material can be found, then the wave-velocity surfaces can be accurately calculated by the methods of McGonigle & Crampin (1982) or, for transversely isotropic media, by the exact equations of White (1965). Crampin & Radovich (1981) demonstrate a method for the estimation of the

elastic constants for transversely isotropic media from the P- and SH-wave arrival time curves on the CDP gathers.

4.5

CDP gather arrival times in transversely isotropic structures: calculations

Exact CDP gather arrival times can easily be determined through the methods of section 4.3 for any horizontally layered, transversely isotropic structure with a vertical direction of symmetry, provided the elastic constants of all the media are known. The NMO can then be calculated from the CDP arrival times.

We have calculated CDP gather arrival times for two such structures, in order to illustrate the effect of anisotropy. The two structures A and B (Tables 4.2(a),(b)) correspond to sedimentary sequences which are commonly encountered in oil exploration. The elastic constants of the anisotropic media, which are Colorado oil shale and a laminated limestone and shale material, have been determined by Kaarsberg (1968) and Levin (1979) respectively, and their values are given in Table 4.3. The angular velocity variations of each anisotropic material, measured in a vertical plane and away from the axis $x_3 = 0$, are illustrated in Fig.4.4.

The customary method for presenting CDP arrival time data is to plot it as two-way travel-time for each shot-receiver path. The origin of the distance axis is set at the centre of the spread and the axis length is determined by the number of shot/receiver stations on each side of the centre, usually 12, and the station spacing, usually 134 m.

In Figs.4.5(a) and (b) we present time-distance plots for the structures A and B respectively, which are described in Table 4.2. The travel-time curves correspond to phases which have been reflected at different interfaces in the anisotropic structures. Note that since the

Table 4.2 Models of sedimentary beds for which CDP travel times are calculated.

(a) Structure A

Layer	Thickness (m)	Material	Type	P velocity (km/s)	S velocity (km/s)	Density (gm/cm^3)
1	300	Sandstone	Isot.	3.353	1.844	2.30
2	300	Colorado Oil Shale	Anis.	(see Fig.4.4(a))		2.37
3	100	Porous Limestone	Isot.	3.658	2.012	2.40
4		Non-porous Limestone	Isot.	4.572	2.515	2.50

(b) Structure B

Layer	Thickness (m)	Material	Type	P velocity (km/s)	S velocity (km/s)	Density (gm/cm^3)
1	300	Sandstone	Isot.	3.353	1.844	2.30
2	300	Laminated Limestone/Shale	Anis.	(see Fig.4.4(b))		2.44
3	100	Porous Limestone	Isot.	3.658	2.012	2.40
4		Non-porous Limestone	Isot.	4.572	2.515	2.50

Table 4.3 Elastic constants of the transversely isotropic materials which constitutes the anisotropic layers in the sedimentary beds.

(a) Colorado Oil Shale (Kaarsberg 1968), density = 2.37 gm/cm^3.

c_{1111}	= 59.5	c_{2222}	= 59.5	c_{3333}	= 42.5
c_{1122}	= 20.1	c_{2233}	= 15.8	c_{3311}	= 15.8
c_{1212}	= 19.7	c_{2323}	= 15.3	c_{1313}	= 15.8

(b) Laminated Limestone/Shale (Levin 1979), density = 2.44 gm/cm^3.

c_{1111}	= 33.77	c_{2222}	= 33.77	c_{3333}	= 26.67
c_{1122}	= 12.54	c_{2233}	= 10.53	c_{3311}	= 10.53
c_{1212}	= 10.61	c_{2323}	= 8.07	c_{1313}	= 10.53

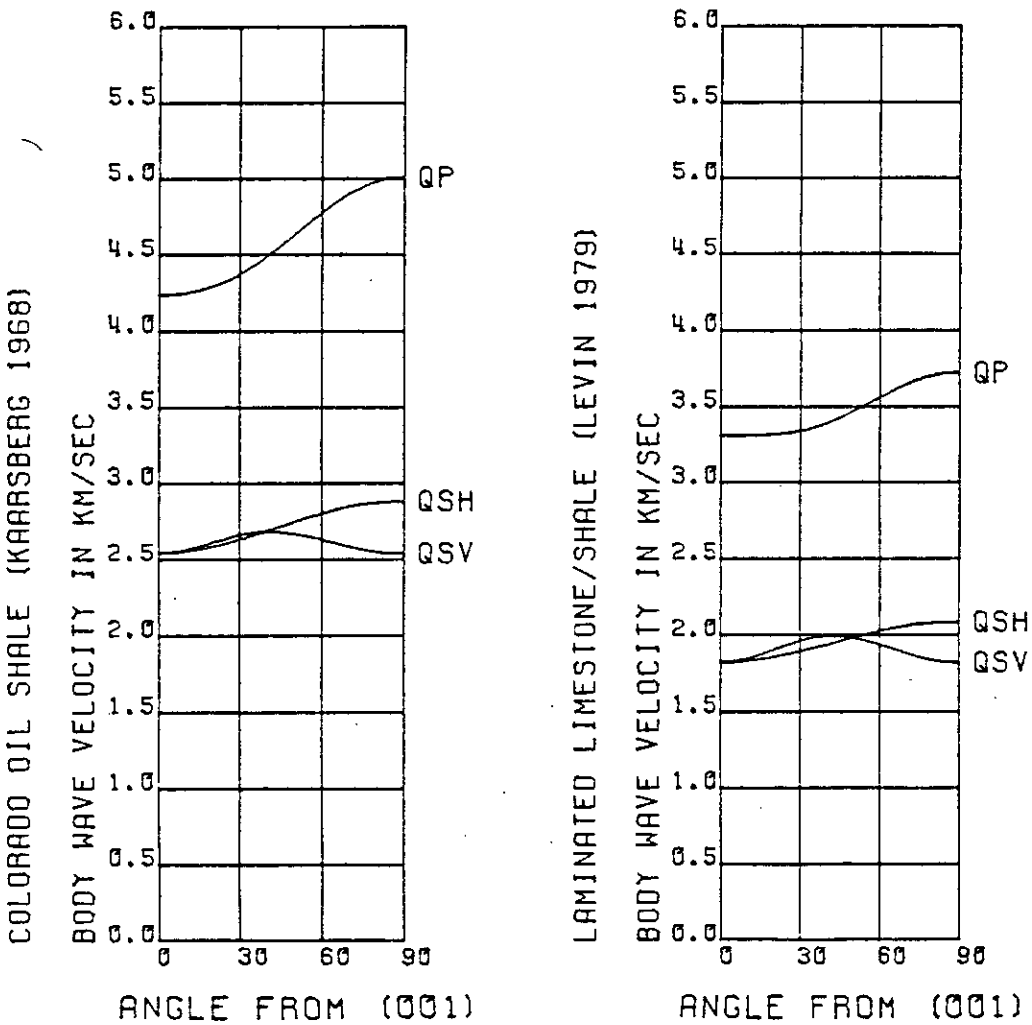

Figure 4.4 Angular velocity variations of the transversely isotropic media which are used in the models of the sedimentary beds. Their elastic constants are given in Table 4.3.

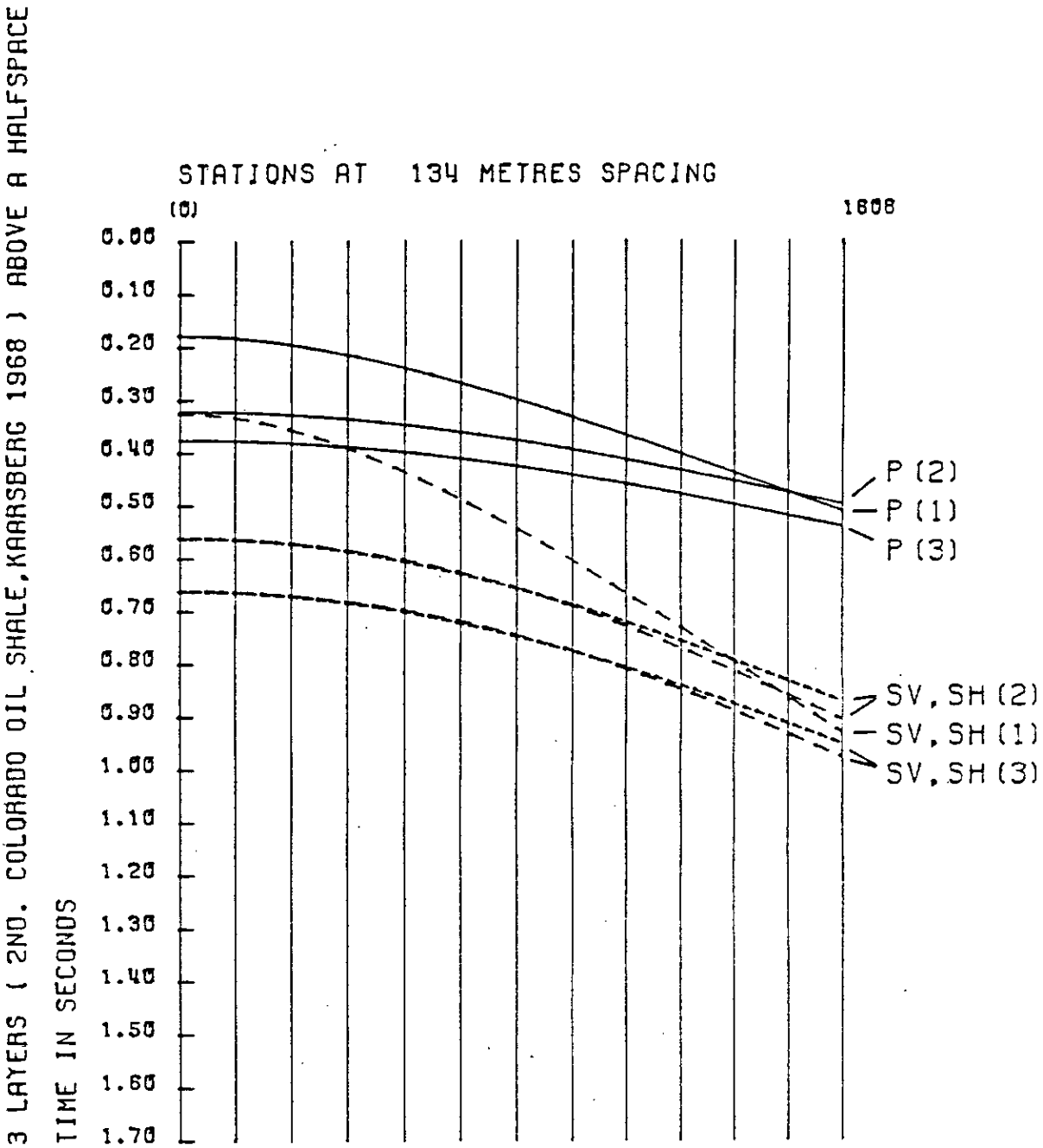

Figure 4.5(a) CDP gather arrival times of P,SV (long dash), and SH (short dash) reflections through the transversely isotropic structure A of Table 4.2. The anisotropic medium is Colorado oil shale, the elastic constants of which have been obtained by Kaarsberg (1968), and are given in Table 4.3(a). The bracketed numerals denote the interfaces at which the reflections occur, interface 1 being located at the bottom of layer 1.

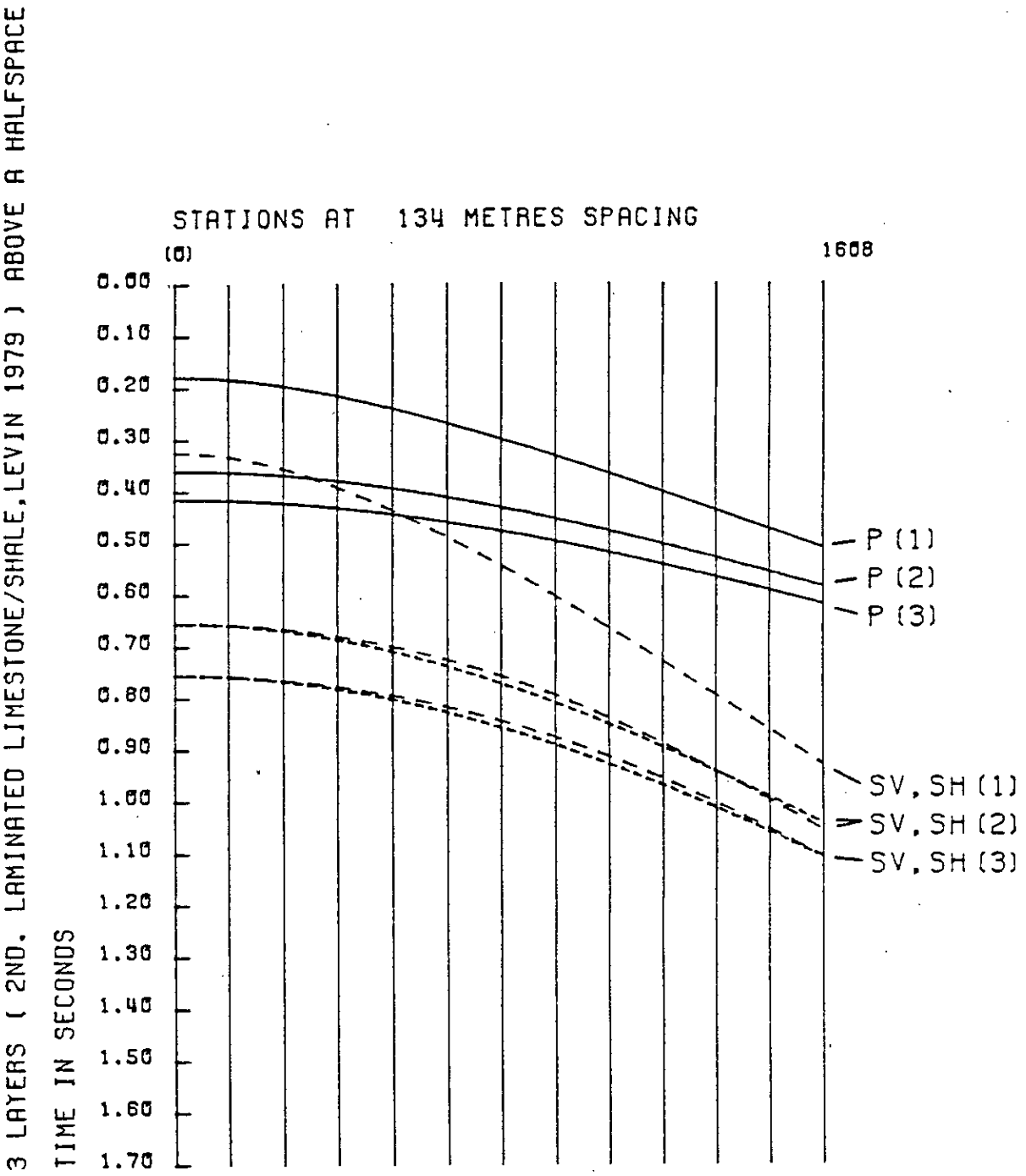

Figure 4.5(b) CDP gather arrival times of P,SV (long dash), and SH (short dash) reflections through the transversely isotropic structure B of Table 4.2. The anisotropic medium consists of interbedded equal-thickness layers of isotropic limestone and shale, as suggested by Levin (1979). The elastic constants of this medium are given in Table 4.3(b). The bracketed numerals denote the interfaces at which the reflections occur, interface 1 being located at the bottom of layer 1.

wave propagation is in the symmetry plane of the transversely isotropic structure, the shear-waves will possess the same polarizations as the SV- and SH-waves in the isotropic media.

For an isotropic layered structure, the arrival times of waves reflected from the structure form hyperbolae on a time-distance plot, and the arrival times of corresponding SV and SH-type reflected and refracted shear-waves are identical. However, for the anisotropic structures described above, these statements are no longer true for waves which have been reflected or refracted through the anisotropic material. In Figs.4.5(a) and (b) these phases are identified by the suffix (2) or (3). It is difficult to see that the travel-time curves for the reflected phases are not true hyperbolae without replotting the curves in the (t^2, x^2) plane, as suggested by Levin (1979) and Crampin & Radovich (1981), when hyperbolae become straight lines. However, it is clear that the arrival times of corresponding SV- and SH-waves differ for propagation away from the (vertical) direction of symmetry. Thus these CDP gather travel-time curves, which were calculated using the methods of section 4.3 and from which the NMO can be obtained, have been shown to display significant differences from their counterparts for isotropic media.

CHAPTER 5

ANOMALOUS REFLECTED ARRIVALS FROM AN ANISOTROPIC UPPER-MANTLE

5.1 Introduction

An increasing amount of evidence suggests that at least the top of the upper-mantle beneath many regions of the Earth is anisotropic. At upper-mantle depths, anisotropy which is caused by fine layering or aligned cracks is not likely to be significant, if it exists at all. The most probable mechanism for upper-mantle anisotropy is a preferred alignment of mineral grains, particularly those of olivine, which is strongly anisotropic. Olivine crystals are probably a major constituent of the upper-mantle lithosphere (Ahrens 1972, Kennedy & Higgins 1972), and thus upper-mantle anisotropy is likely to be due to the alignment, or partial alignment, of olivine crystals by their deformation due to creep or glide (Francis 1969) or syntectonic recrystallisation in a tectonic stress field (Ave'Lallemant & Carter 1970). Crampin (1977b) and Meissner & Flüh (1979) have discussed the implications of this hypothesis. They have suggested that anisotropic alignments in the upper-mantle could vary with depth, in some circumstances, and the alignments would then contain much valuable information on the tectonic history of the lithosphere.

Body-wave studies of upper-mantle anisotropy may involve the analysis of arrivals from local, regional, or teleseismic events. Teleseismic arrivals are approximately plane waves, and Keith & Crampin (1977c) constructed synthetic seismograms for plane waves which passed through various thicknesses of anisotropic material in the upper mantle. They showed that most of the usual seismic measurements would be unaffected even by the presence of quite large amounts of anisotropy, except for comparatively small variations in arrival times. However, Keith & Crampin demonstrated that anisotropy could be indicated by the presence of

anomalous arrivals which would not occur for propagation through isotropic media. Possible anomalous arrivals are P to SH (PSH), or SV to SH (SVSH) converted waves at plane horizontal interfaces with an anisotropic material. Another anomalous characteristic of seismic wave propagation through an anisotropic medium is the formation of split shear-waves with nearly orthogonal polarizations. This characteristic is particularly significant since it depends on the orientation and path length of the quasi-shear waves in the anisotropic medium, rather than the degree of anisotropy (Crampin 1977a). Singh (1982) has obtained evidence of upper-mantle anisotropy from the detection of anomalous teleseismic shear-wave arrivals.

So far, the principal observational evidence for body-wave anisotropy in the upper-mantle has come from experiments using local or regional sources. The experiments have involved the use of many long refraction-profiles, and have shown an azimuthal velocity variation of Pn arrivals, which indicates the presence of anisotropy in the upper-mantle immediately beneath the Moho. Such profiles are expensive, and it would be helpful if there were a method of detection which could be applied to individual three-component seismograms.

If anomalous arrivals were observable on seismograms from local or regional sources, they could provide a cheaper method of investigating anisotropy. However, observations of such arrivals have been rare, and so far it has not been possible to estimate the probable amplitude of these arrivals theoretically. Up to now, it has only been possible to describe seismic wave propagation in anisotropic media for a plane wavefront, rather than a curved wavefront from a local or regional source. The anisotropic reflectivity technique described in chapter 3 permits the construction of synthetic seismograms for arrivals from a point source for a weakly anisotropic stratified structure.

This chapter is devoted to a study of the dynamic properties of

anomalous body-wave arrivals on synthetic seismograms, using simple stratified models of an anisotropic continental upper-mantle. In particular we investigate anomalous arrivals from a layer with a realistic degree of anisotropy, located immediately beneath the Moho. The models are based on the structure and anisotropy beneath Western Germany, where Pn-wave velocity-anisotropy has been detected by Bamford (1973,1977). We shall examine the amplitudes of the anomalous arrivals and assess the likelihood of their detection on experimentally-observed seismograms.

5.2 Observational evidence for upper-mantle anisotropy

Observational evidence for upper-mantle anisotropy comes from both body-wave and surface-wave studies. A brief review of these observations is given here, which is largely based on more extensive reviews by Bamford & Crampin (1977), Keith (1975), and Kirkwood (1978).

1. Surface-wave observations

The presence of anisotropy beneath Eurasia has been suggested by the work of Crampin & King (1977), following earlier work by Crampin (1966,1967, 1975). They observed coupled transverse and sagittal plane motion for higher mode surface-waves for a number of paths across Eurasia from NORSAR records. This may be attributed to aligned anisotropy in the upper-mantle.

Forsyth (1975) studied dispersion curves of Rayleigh and Love waves across the NAZCA plate in the Pacific and he was able to resolve azimuthal anisotropy of the fundamental Rayleigh mode. Schlue & Knopoff (1976,1977) also used wave-paths across the Pacific. Their results could not resolve azimuthal anisotropy but showed that the SH-wave velocity was about 3%

greater than the SV-wave velocity in the upper mantle. From their inversion procedures, Forsyth and Schlue & Knopoff declared that the anisotropy extended to the top of the low-velocity zone. While not disputing the broad conclusions of their results, Crampin (1976) showed that the simplistic inversion procedures used by Forsyth (1975) and Schlue & Knopoff (1976,1977) could result in errors in the degree of anisotropy and its exact depth range.

Kirkwood & Crampin (1980) have found polarization anomalies of the fundamental Love mode across the Pacific, with an azimuthal variation. The variation is consistent with a hexagonally anisotropic upper-mantle with the axis of symmetry parallel to the direction of plate motion. However, it was not possible to define the exact depth range of the anisotropy with the data which was available.

2. Body-wave observations

Hess (1964) suggested the presence of Pn-wave velocity-anisotropy in the oceanic upper mantle after analysing a number of individual refraction-profiles which were carried out in the Pacific Ocean. Following Hess, a number of experiments specifically designed to investigate Pn velocity-anisotropy were made by Raitt, Shor, Francis & Morris (1969) and others. They used the time-term method of data analysis, and observed an azimuthal Pn velocity variation of up to 8%, with the direction of maximum velocity parallel to the spreading direction of the lithosphere. Later oceanic surface-wave studies, which have been described above, have shown that the anisotropy is not necessarily confined to the top few kilometres of the mantle.

Azimuthal coverage of Pn-wave arrivals is not too difficult in oceanic refraction studies, where profiles can easily be set up and the mantle is

overlain by a relatively thin and simple crustal structure which displays a high degree of lateral homogeneity. However, investigation of azimuthal variations of Pn-wave arrivals is much more difficult on continents, where profiles must be long (at least 150 km) with close station spacing to resolve and correct for a complex crustal velocity-structure. As a result of these difficulties, the most convincing evidence of continental upper-mantle anisotropy from refraction data is based on statistical analyses of time-term data from Western Germany (Bamford 1973,1977), and the Western United States (Bamford, Jentsch & Prodehl 1979). The data was obtained from a large number of seismic refraction profiles which were carried out over a period of some years. Although the profiles were not originally planned for an investigation of this type, they did give adequate azimuthal coverage.

Bamford (1973,1977) obtains a Pn-wave velocity anisotropy of 6-7% under Western Germany, with the direction of maximum velocity 15-20° East of North. Fuchs (1977) observes that this direction correlates with the direction of plate motion and the direction of maximum compression in the crust. Bamford et al.(1979) find up to 3% Pn-wave velocity anisotropy beneath the Western United States, with the direction of maximum velocity 70-80° East of North. This result is very similar to previous results obtained offshore in the Pacific ocean, and Bamford et al. suggest that the anisotropy is due to subduction of the lithosphere beneath the Western United States.

These Pn-wave velocity anisotropies which are detailed above should be examined more closely, in the light of recent work by Whitcombe & Rogers (1981). Whitcombe & Rogers demonstrate how non-iterative time-term solutions can give rise to erroneous refractor velocity anisotropies, if the topography of the refractor is strongly directional. They also show that a false velocity anisotropy can be deduced for the upper-mantle

refractor, if crustal velocity-anisotropy is present and is not taken account of in the time-term solution. Both effects are substantially larger for the continental upper-mantle than for the oceanic upper-mantle, due to the larger continental crustal thickness.

However, the observed Pn-wave velocity anisotropies appear to be too large to be explained in terms of realistic directional refractor topographies alone. In particular, Bamford (1973) employed an iterative technique in his time-term solution, which would lead to a true solution if the anisotropy was wholly due to refractor topography. The Pn-wave velocity anisotropy observed in the Western United States is small, but it correlates with results obtained in the nearby ocean, where the effects of topography and crustal anisotropy are much smaller.

Nevertheless, these effects may result in a perturbation of the time-term solution for the true upper-mantle anisotropy. Crampin & Bamford (1977) experienced some difficulty in inverting Bamford's (1973,1977) Pn-wave velocity observations in terms of a petrological model of the upper-mantle. Whitcombe & Rogers have pointed out that the difficulty may arise from a distortion of the true form of the azimuthal variation of Pn velocity, due to directional refractor topography and/or crustal anisotropy.

Pn velocity-variations can only demonstrate anisotropy in the upper-mantle immediately beneath the Moho. Over a wider range of lithospheric depths there are many other seismic observations which are indicative of anisotropy, but which provide only circumstantial evidence if taken individually (Hirn 1977). Nevertheless a consistent picture of an anisotropic lower lithosphere can be built up if the evidence is taken together (Fuchs 1977,1979; Meissner & Flüh 1979).

Fine structure and relatively high velocities of 8.2 - 8.7 km/s in the lower lithosphere to a depth of over 50 km are found on long refraction

profiles (Kind 1974; Faber 1978; Ansorge, Bonjer & Emter 1979; Asada & Shimamura 1979). Asada & Shimamura also report an azimuthal variation of velocities in the lower lithosphere, from their study of oceanic refraction profiles. Meissner & Flüh (1979) suggest that the fine structure may be caused by different alignments of crystalline anisotropy. Ando, Ishikawa & Wada (1980) have observed splitting of shear-wave arrivals from events located at a depth of 200 - 300 km beneath a group of recording stations on the Japanese island arc. This observation is attributed to a 50-100 km thick anisotropic region above the descending plate. Leven, Jackson & Ringwood (1981) have shown that it is difficult to account for a pronounced high-velocity zone at a depth of 200 - 250 km beneath northern Australia without invoking velocity anisotropy. They suggest that the anisotropy is stress-induced by the presence of a shear zone at 200 - 250 km, which is associated with the decoupling of the lithosphere from the underlying mantle.

We have shown that there is evidence for the presence of anisotropy in the upper mantle. We shall use the anisotropic reflectivity technique to study anomalous arrivals which are due to the passage of curved wavefronts through simple models of an anisotropic continental upper mantle. The nature and origin of these anomalous arrivals have been discussed in section 3.3.

5.3 Simple models of an anisotropic upper-mantle

We consider only upper-mantle anisotropy immediately beneath the Moho and we use simple velocity-depth models which are based on the structure and anisotropy under Western Germany. The Pn velocity-anisotropy detected there is the strongest continental anisotropy which has been found so far, for which approximate elastic-constants have been determined (Crampin &

Bamford 1977).

The models in Fig.5.1 consist of a one-layer crust (models 1A, 1B), or a two-layer crust (models 2A,2B,2C), below a free surface and above an anisotropic upper-mantle layer over an isotropic halfspace. Poisson's ratio is assumed to be 2.5 in the isotropic media. Models 1A, 1B, 2A, and 2C are very simple approximations to the velocity-depth structure believed to exist under Western Germany (Edel et al.1975). The P- and SV-wave velocities of the lower isotropic halfspace are larger in models 1B and 2C than in models 1A and 2A. Model 2B will be used to illustrate the effect of a lower velocity-contrast between the crustal layers. The layers have been assumed to be perfectly elastic, and free surface effects are accounted for at the receiver R, but not at the source S. The curvature of the Earth is not taken into account, due to the complexity of applying Müller's (1973) earth-flattening approximation to anisotropic media.

The models are necessarily very simple due to the long computing time involved in the iterative calculation of the response through the sequence of layers, as described in section 3.6(c). Nevertheless they should allow an assessment to be made of the likely amplitude of anomalous arrivals due to anisotropy. Also, there will be relatively few arrivals on the synthetic seismograms and these will be easily identified. This is an advantage in this preliminary study since we are looking for anomalous arrivals which are expected to be small.

The anisotropic material which forms the subcrustal layer is a mixture of 30.8% hexagonal olivine and 69.2% isotropic material. This mixed material displays a P-wave velocity-anisotropy of 7%. It is one of the four anisotropic materials with which Crampin & Bamford (1977) were able to obtain an approximate fit to Bamford's (1973) observed Pn velocity variations. This material was chosen as it was originally possible to calculate travel times in symmetry planes only for a material with

Figure 5.1 Simple models of an anisotropic upper-mantle with anisotropy made up of 30.8% hexagonal olivine with horizontal symmetry axis, and 69.2% isotropic material (elastic constants in Table 5.1).

(a) Two-layer models 1A, 1B and the radiation pattern for SV-waves from a vertical double-couple source inclined at 45° to the x_1 axis.

(b) Three-layer models 2A, 2B, 2C

(c) Alignment and velocity variations of the anisotropic material.

(a)

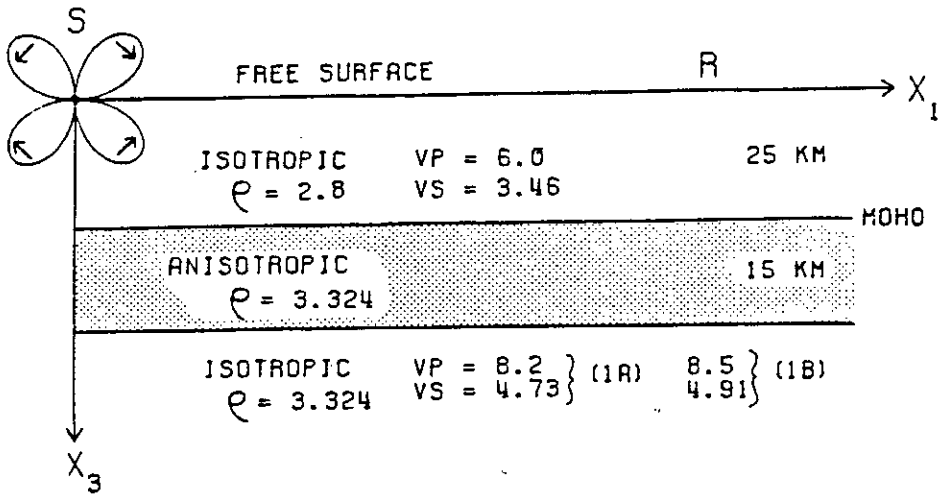
S
FREE SURFACE
R
X_1
ISOTROPIC
ρ = 2.8
VP = 6.0
VS = 3.46
25 KM
MOHO
ANISOTROPIC
ρ = 3.324
15 KM
ISOTROPIC
ρ = 3.324
VP = 8.2 } (1A)
VS = 4.73 }
8.5 } (1B)
4.91 }
X_3

(b)

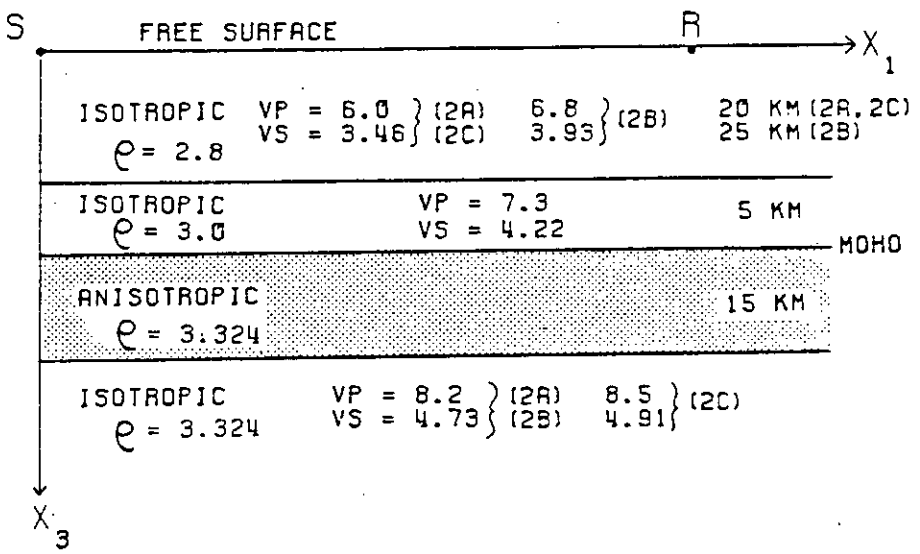
S
FREE SURFACE
R
X_1
ISOTROPIC
ρ = 2.8
VP = 6.0 } (2A)
VS = 3.46 } (2C)
6.8 } (2B)
3.93 }
20 KM (2A, 2C)
25 KM (2B)
ISOTROPIC
ρ = 3.0
VP = 7.3
VS = 4.22
5 KM
MOHO
ANISOTROPIC
ρ = 3.324
15 KM
ISOTROPIC
ρ = 3.324
VP = 8.2 } (2A)
VS = 4.73 } (2B)
8.5 } (2C)
4.91 }
X_3

(c)

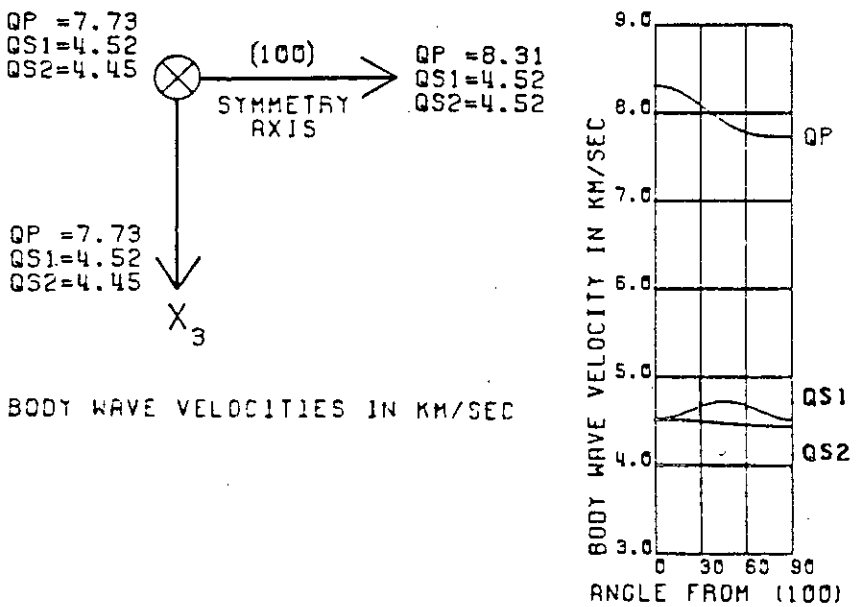
QP =7.73
QS1=4.52
QS2=4.45
(100)
SYMMETRY AXIS
QP =8.31
QS1=4.52
QS2=4.52
QP =7.73
QS1=4.52
QS2=4.45
X_3
BODY WAVE VELOCITIES IN KM/SEC
BODY WAVE VELOCITY IN KM/SEC
9.0
8.0
7.0
6.0
5.0
4.0
3.0
QP
QS1
QS2
0
30
60
90
ANGLE FROM (100)

hexagonal anisotropic symmetry. Later work by McGonigle & Crampin (1982) permits the calculation of travel times in non-symmetry planes, and in materials with orthorhombic symmetries. However, a hexagonal structure with a horizontal symmetry axis will lead to seismic effects which are almost indistinguishable from orthorhombic structures with similar velocity variations.

The velocity variations of the three possible seismic waves in the chosen material, and its alignment with respect to the vertical (x_3) axis, are illustrated in Fig.5.1(c). We initially align the x_1 axis in Figs. 5.1(a) and (b) parallel to the axis of symmetry of the material, and the elastic constants of the material are given in Table 5.1 for this alignment. We then rotate the sagittal plane about the x_3 axis in order to show the azimuthal variation of propagation characteristics. This involves a rotation of the elastic tensor (Keith & Crampin 1977a) prior to solving the wave equation for the vertical slownesses and amplitude vectors, as described in section 3.3.

In the following section we describe the slowness sheets and wave polarizations of the qP-, qS1- and qS2-waves, for different orientations of the anisotropic material. This will assist us later in the interpretation of the seismograms.

5.4 Wave slowness-sheets and polarizations in a medium with hexagonal symmetry

The hexagonally anisotropic material which is used in the models is aligned with its axis of symmetry in the horizontal plane. We define an orthogonal system of axes (q_1 ,q_2 ,q_3) which are fixed in the material, with q_1 along the axis of symmetry and q_3 vertically downwards.

Table 5.1 Elastic constants of the anisotropic material which constitutes the subcrustal layer: 30.8% hexagonal olivine, 69.2% isotropic material $\alpha = 7.513$, $\beta = 4.338$ km/s, $\rho = 3.324$ gm/cm^3 (Crampin & Bamford 1977). The x_3 axis is vertical and the symmetry axis x_1 is horizontal.

$c_{1111} = 229.63$	$c_{2222} = 198.67$	$c_{3333} = 198.67$
$c_{2233} = 67.30$	$c_{3311} = 64.53$	$c_{1122} = 64.53$
$c_{2323} = 65.68$	$c_{1313} = 67.96$	$c_{1212} = 67.96$

Each slowness vector of the three propagating body-waves traces out a three-dimensional slowness surface in slowness space. In Fig.5.2 we illustrate the intersection of the slowness surfaces with three orthogonal symmetry planes aligned normal to the axes q_1, q_2 and q_3. The two shear-wave slowness surfaces are analytically continuous and touch at a point on the positive q_1-axis, the axis of symmetry, as shown in Fig.5.2. A similar contact will occur on the negative q_1-axis. These contacts are singularities of the shear-wave slowness surface.

Crampin & Kirkwood (1981) and Crampin & Yedlin (1981) have shown that there are three types of shear-wave singularity and in the region of each there may be disturbances to shear-wave propagation. The singularity illustrated in Fig.5.2 is of the "kiss" type. For the type and orientation of the material with hexagonal symmetry which is used in the models, the variation of phase velocity near the singularity is insufficient to give rise to such disturbances.

The polarizations of the quasi-shear waves are illustrated for propagation along the three coordinate axes. If initially we take the sagittal plane as the plane $q_2=0$, then for a general angle of incidence the faster qS1-wave is polarized wholly in the sagittal plane. The particle-motion of the slower qS2-wave is wholly transverse to the sagittal plane. For propagation along the q_1 and q_3 axes the polarizations of qS1 and qS2 correspond to SV- and SH-polarization, respectively. The velocities of both qS1- and qS2-waves will vary for different directions of propagation between q_1 and q_3.

If we rotate the sagittal plane 90° about the q_3 axis so that the waves propagate in directions normal to the axis of symmetry, then the velocities of all the quasi-body waves are invariant with direction. In this plane of propagation it is the slower qS2-wave which is polarized in the sagittal plane and the faster qS1-wave is polarized in the transverse

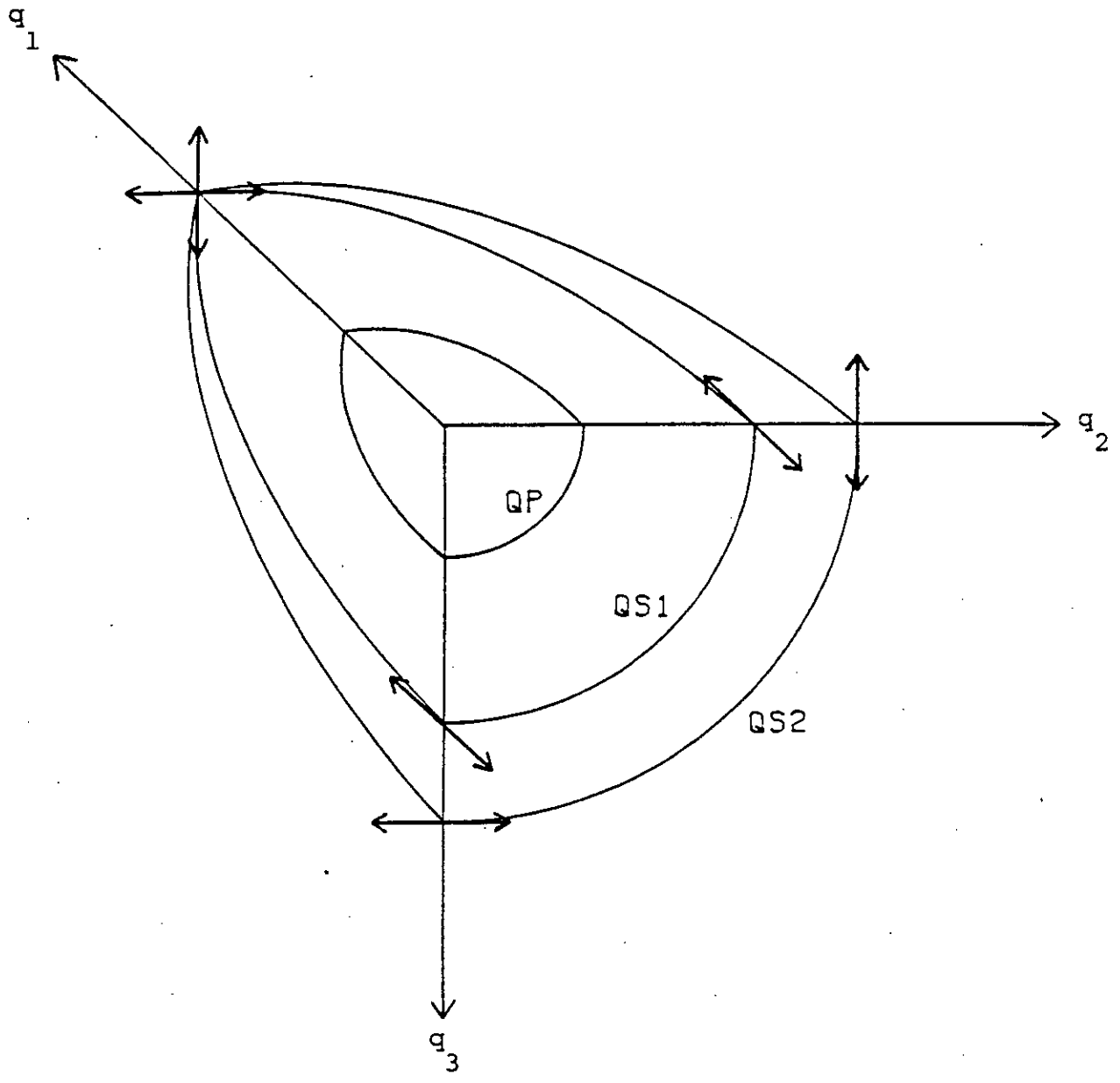

Figure 5.2 Configuration of the slowness-sheets of a material with hexagonal symmetry, with its axis of symmetry along the q_1 axis. The polarization directions of the quasi-shear waves which propagate along the co-ordinate axes are denoted by double-headed arrows.

direction. In every direction the polarizations of the qS1- and qS2-waves correspond to SH- and SV-polarization, respectively.

When the sagittal plane is vertically orientated at intermediate azimuths between q_1 and q_2, the polarizations of the qS1- and qS2-waves do not coincide with the dynamic axes. As the azimuth of the sagittal plane nears one or other of the planes of symmetry, so the polarization of the qS1- and qS2-waves becomes more nearly polarized parallel to, or transverse to, the symmetry plane.

5.5 General description of the seismograms

We describe in this section some general features of the synthetic seismograms which have been constructed using the anisotropic reflectivity technique and the anisotropic upper-mantle models which were illustrated in Fig.5.1 and discussed in section 5.3.

We form synthetic seismogram profiles at different azimuths with respect to the horizontal axis of symmetry. We take one profile with the vertical sagittal plane parallel to the axis of symmetry, and one with the vertical sagittal plane transverse to the axis of symmetry. Both these profiles are in directions of crystal symmetry, and so no anomalous phases are observed on these profiles. However, the character of the seismograms will differ because of the different velocity contrasts involved.

We also take at least one profile for each model at an azimuth which is intermediate between the symmetry directions (usually at 45° to the axis of symmetry). Anomalous converted phases will be observed on these profiles.

The synthetic seismograms are intended to simulate records from a refraction profile, or from a regional earthquake. We calculate the seismograms within a 12 s time window when an explosive source is used, as in a refraction profile. We use the signal spectrum given by equation

(3.7.1) with f_o (= $\omega_o/2\pi$) = 5.33, which gives a signal which is approximately one sine-wave pulse with a principal frequency of 2.24 Hz (Fig.3.1). The explosion source will generate anomalous PSH converted waves for propagation in non-symmetry directions, following the arguments of section 3.3.

For an earthquake, the largest anomalous phases are most likely to be generated by incident shear-waves. In this work we use a vertical double couple source to generate incident SV-polarized shear-waves. The double couple has been rotated 45° about the transverse axis so that possible anomalous phases are not obscured by nodes in the source radiation pattern. The radiation pattern for SV-waves from the rotated double-couple source is illustrated in Fig.5.1(a). We use the same signal spectrum as for the explosion source, but with a lower principal frequency (0.9 Hz) and a longer time window (30 s). In both cases, the direct waves from source to receiver in the top layer are omitted.

The number of data points in each seismogram is 256, and each integrated displacement spectrum has been formed by integration over 320 slowness values. The phase velocities which correspond to the limits of integration are 6.06 and 20.79 km/s for incident P-waves, and 3.5 and 12.0 km/s for incident SV-waves. Thus for both P- and SV-waves incident on the reflection-zone, the integration has been performed over the same range of angles of incidence, from 17° to 82°.

No normalization was applied to the seismograms, when forming the profiles and the relative amplitudes are correct across each seismic section. Travel time curves have been drawn for the principal arrivals on the seismograms, to assist identification of the phases. The travel-time curves have been calculated by the method described in chapter 4.

5.6 Anomalous reflected arrivals from incident P-waves

Seismic sections of vertical-component synthetic seismograms at azimuths 0°, 45° and 90° from an explosive source are illustrated in Fig.5.3(a), for the model 1A. There is a clear azimuthal variation in the character of the principal P-wave arrivals, numbered 1-4.

In particular, the velocity of the head-wave in the anisotropic layer is observed to vary between 8.31 km/s at 0° and 7.73 km/s at 90°, according to the velocity-variation graph in Fig.5.1(c). Also, the amplitude of the reflected P-wave (3) from the base of the anisotropic layer is observed to vary with azimuth. At 0° azimuth there is a negative velocity gradient over the interface between the anisotropic layer and the lower halfspace. Thus the wave arrival (3), which is reflected at this interface, possesses very little energy at this azimuth. As the azimuth is increased through 45° to 90°, the velocity gradient becomes positive and increasing, and there is a corresponding increase in amplitude of the reflected wave (3).

In Fig.5.3(b) we present the corresponding radial component seismograms and focus attention on the converted PSV arrivals which are identified in the figure. The variation in the character of these arrivals is less marked than for the reflected P-waves, but it is still perceptible. Shear-wave splitting will occur at azimuth 45° due to the converted phases (4) P->qP->qS1->SV and (5) P->qP->qS2->SV. However these arrivals are small and not well separated due to the short path length of the quasi-shear waves in the anisotropic layer.

Anomalous phases from an explosive source are most likely to be observed on the transverse component, at azimuths intermediate between symmetry directions. We present three-component seismic sections for the azimuth 45° in Fig.5.4. The largest anomalous arrival is the PSH converted phase at the Moho (arrival 1 on the transverse component). The amplitude

Figure 5.3 Sections of synthetic-seismograms from an explosive source for model 1A at azimuths 0°, 45°, and 90°, relative to the orientation of the anisotropy. Schematic descriptions of the arrivals identified by their travel-time curves are also shown, where M is Moho, and the anisotropic layer is shaded. The small-amplitude first arrival, which travels at the horizontal apparent velocity of 6.06 km/s and is visible at distances 40-100 km in Figures 5.3 to 5.6, is a numerical arrival which is associated with the lowest phase velocity used in the calculations.

(a) Vertical component seismograms.

(b) Radial component seismograms.

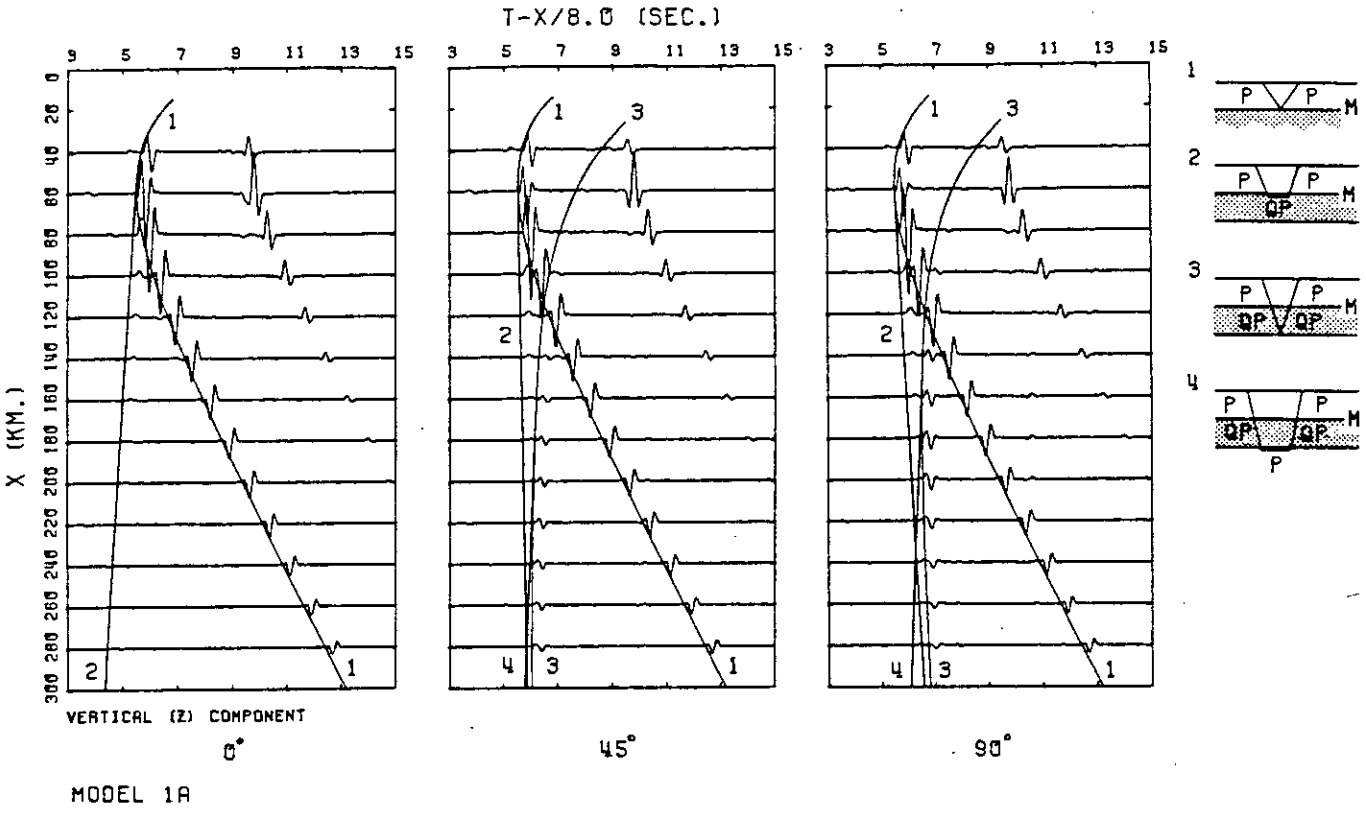
T-X/8.0 (SEC.)
X (KM.)
VERTICAL (Z) COMPONENT
0°
45°
90°
MODEL 1A
1 P P M
2 P P QP M
3 P P QP QP M
4 P P QP QP M P

(a)

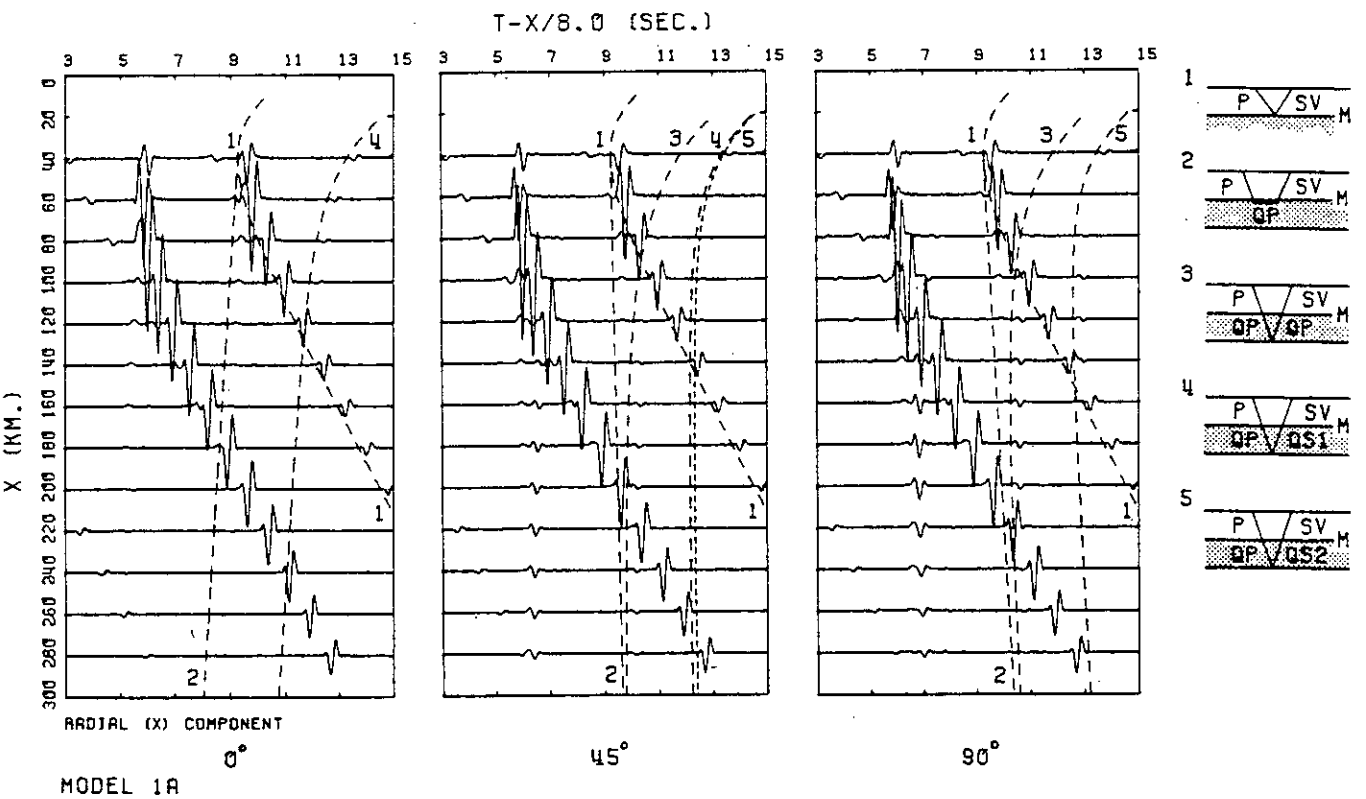
T-X/8.0 (SEC.)
X (KM.)
RADIAL (X) COMPONENT
0°
45°
90°
MODEL 1A
1 P SV M
2 P SV QP M
3 P SV QP QP M
4 P SV QP QS1 M
5 P SV QP QS2 M

(b)

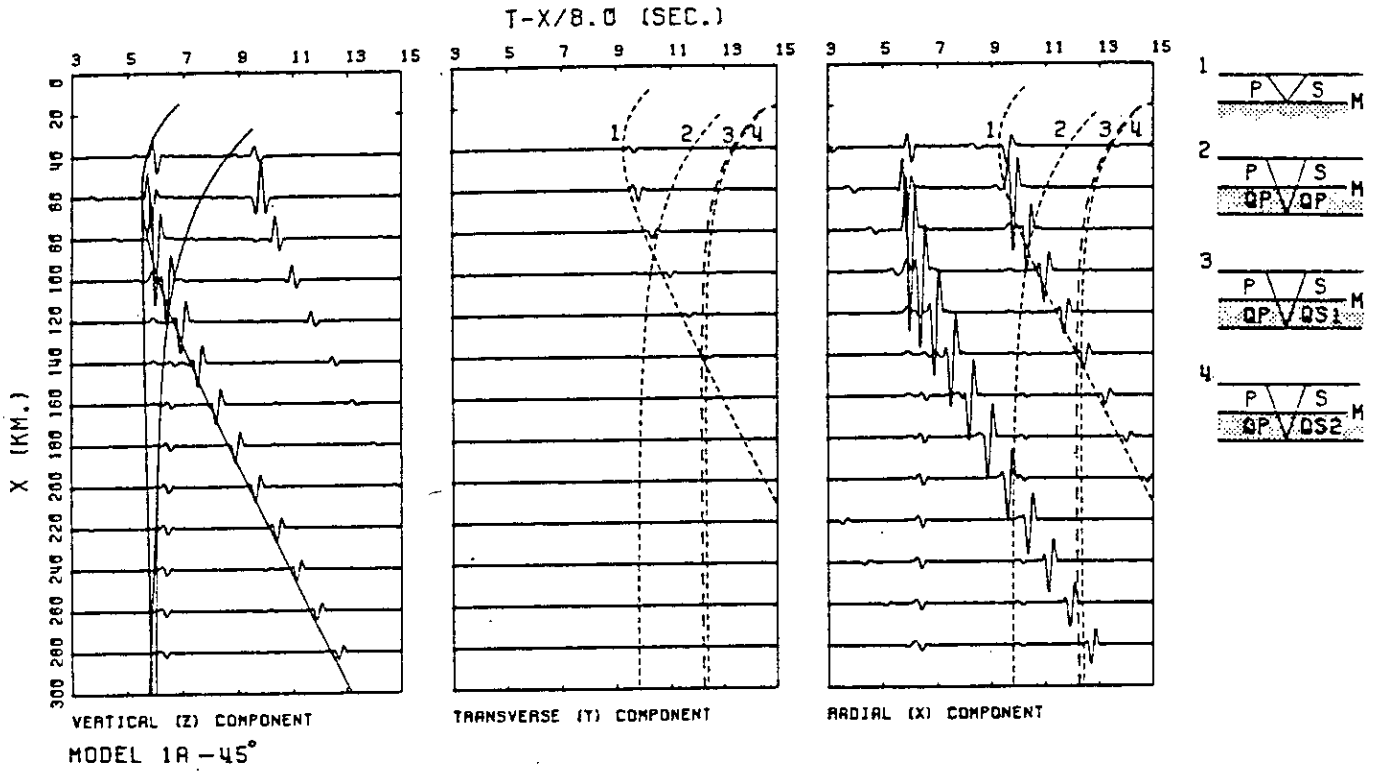

Figure 5.4 Three-component synthetic-seismogram sections from an explosive source for model 1A at azimuth 45°. The principal anomalous phases appear on the transverse component.

of this reflected phase is a maximum at approximately 60 km from the source. This distance is about 20 km beyond the critical distance for the propagation of compressional head-waves in the anisotropic sub-Moho layer. The energy of transmitted qS1- and qS2-waves reaches a maximum at or beyond this critical distance, whereas the energy of transmitted qP-waves becomes zero just beyond the critical distance. This confirms that it is the quasi-shear waves rather than the quasi-P waves which possess most energy in the transverse component (Keith & Crampin 1977). Arrivals 3 and 4 represent small-amplitude converted wave arrivals which show shear-wave splitting.

The amplitude of the anomalous PSH arrival is very small when compared to the amplitude of the simultaneously-arriving PSV arrival on the radial and vertical components, and the PSH arrival would be difficult to identify reliably in a heterogeneous Earth.

The anomalous phases are not necessarily largest at 45°. Transverse component seismograms were also constructed with model 1A for azimuths of 22.5° and 67.5°, and they are compared with those for azimuth 45° in Fig.5.5. However the amplitudes of the anomalous arrivals on these seismograms did not indicate that other azimuths would give significantly greater anomalous arrivals. In an experimental situation with model 1A, the anomalous arrivals would certainly be lost in the seismic noise, especially the signal-generated noise caused by the simultaneously-arriving, large-amplitude PSV converted phases.

In practice, PSV reflected waves from the Moho have rarely been observed on continental refraction-profiles (Fuchs 1975), which confirms that model 1A is over-simplistic. Fuchs (1975) showed that a transition zone just over 1 km thick at the Moho would render PSV reflections unobservable. Thus PSV reflections at the Moho are only observed where it is a first-order discontinuity (Fuchs 1975), and their observation usually

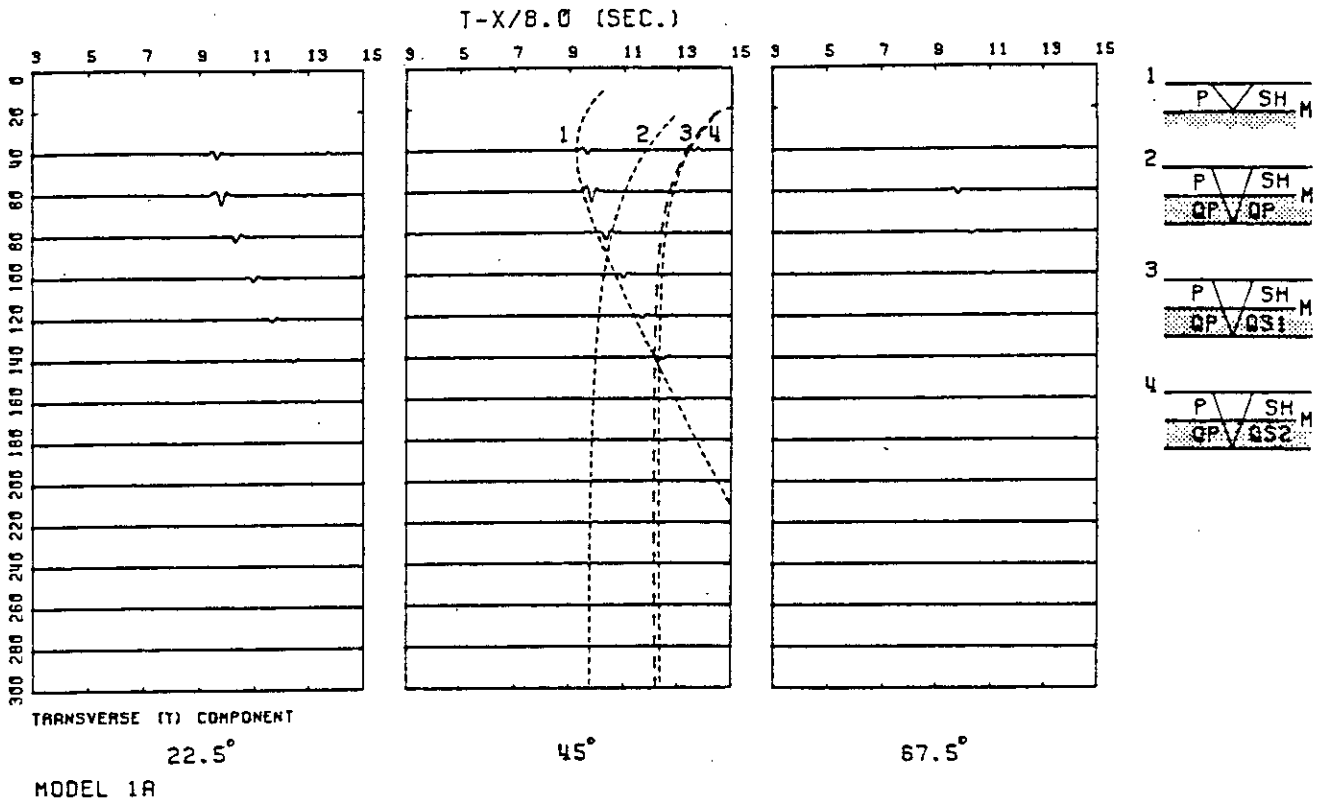

Figure 5.5 Transverse component synthetic-seismogram sections from an explosive source for model 1A at azimuths 22.5°, 45°, and 67.5°.

requires the use of three component data (Jacob & Booth 1977; Assumpção 1980).

In a first approximation to a more gradual transition between crust and mantle, a three layer model was used - model 2A. It incorporates a thin lower crustal layer with thickness and velocity values based on approximate values for the transition zone between crust and upper-mantle under Western Germany, from the results of Edel et al.(1975). Three-component synthetic seismogram sections are presented in Fig.5.6(a) for model 2A at 45° azimuth. The relative amplitude of the anomalous PSH Moho reflection (arrival 2 on the transverse component) is now much larger than the simultaneously-arriving PSV reflection (arrival 2 on the radial component). However the absolute amplitude of the anomalous PSH phase is even smaller than for model 1A.

The velocity contrast between the upper and lower crustal layers is still quite sharp in model 2A, and the additional model 2B illustrates the effect of a more gradual transition zone. The synthetic seismograms for model 2B are shown in Fig.5.6(b). The anomalous PSH Moho reflections are now of the same order of magnitude as the PSV reflections on the radial and vertical components, and also the same order as the PP reflections over a limited distance range (60 - 80 km). However their absolute amplitude, and therefore their detectability, remains very small.

5.7 Anomalous reflected arrivals from incident SV-waves

We use the double-couple source illustrated in Fig.5.1(a), which generates SV-waves polarised in the sagittal plane, and we expect to observe shear-wave splitting at off-symmetry azimuths, as explained in section 3.3. Synthetic seismograms are calculated only for the shear-wave arrivals: P-wave arrivals are ignored. We shall discuss the seismograms obtained by

Figure 5.6 Three-component synthetic-seismogram sections from an explosive source at azimuth 45°, for

(a) model 2A, and

(b) model 2B.

Reflected P-waves from the base of layers 1,2, and 3 are denoted by 1',2', and 3', respectively.

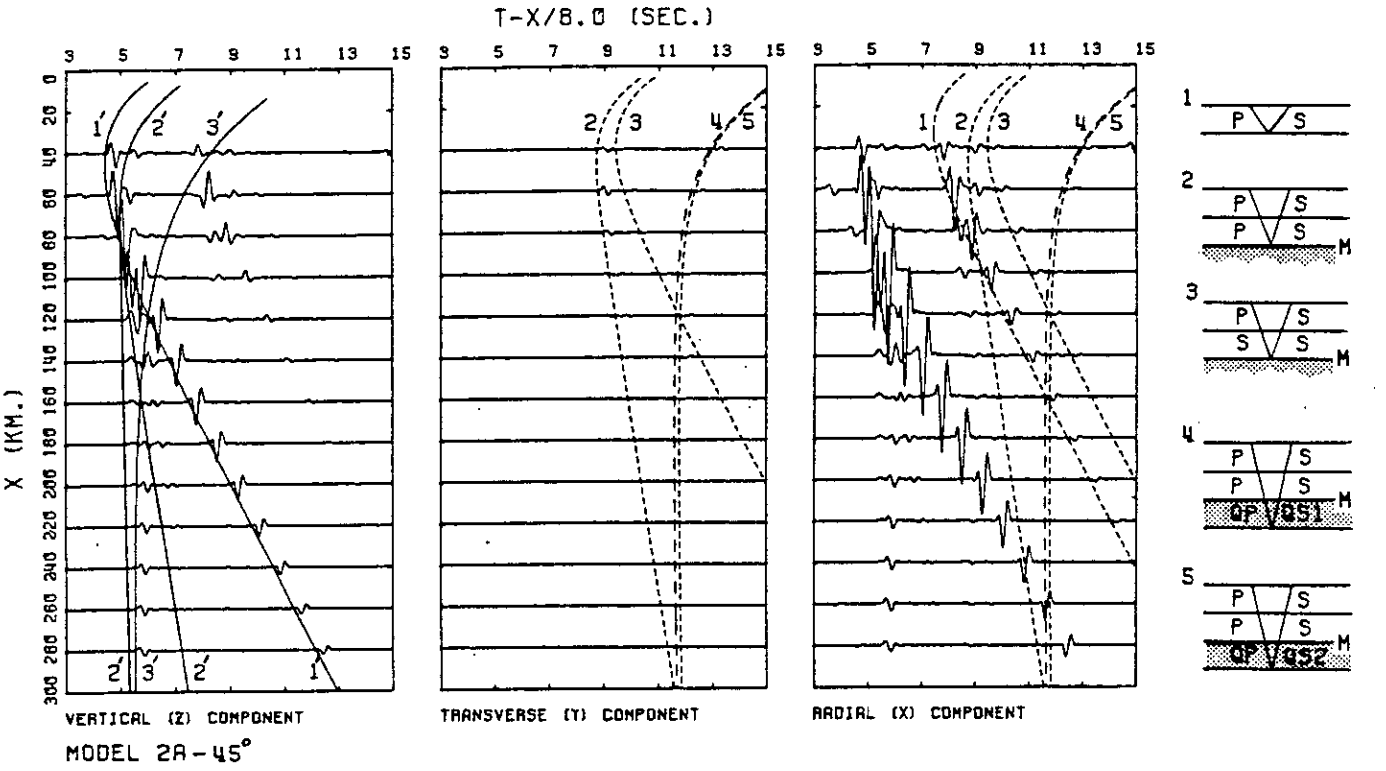
T-X/8.0 (SEC.)
X (KM.)
VERTICAL (Z) COMPONENT
TRANSVERSE (T) COMPONENT
RADIAL (X) COMPONENT
MODEL 2A-45°
1
2
3
4
5
P
S
M
QP
QS1
QS2

(a)

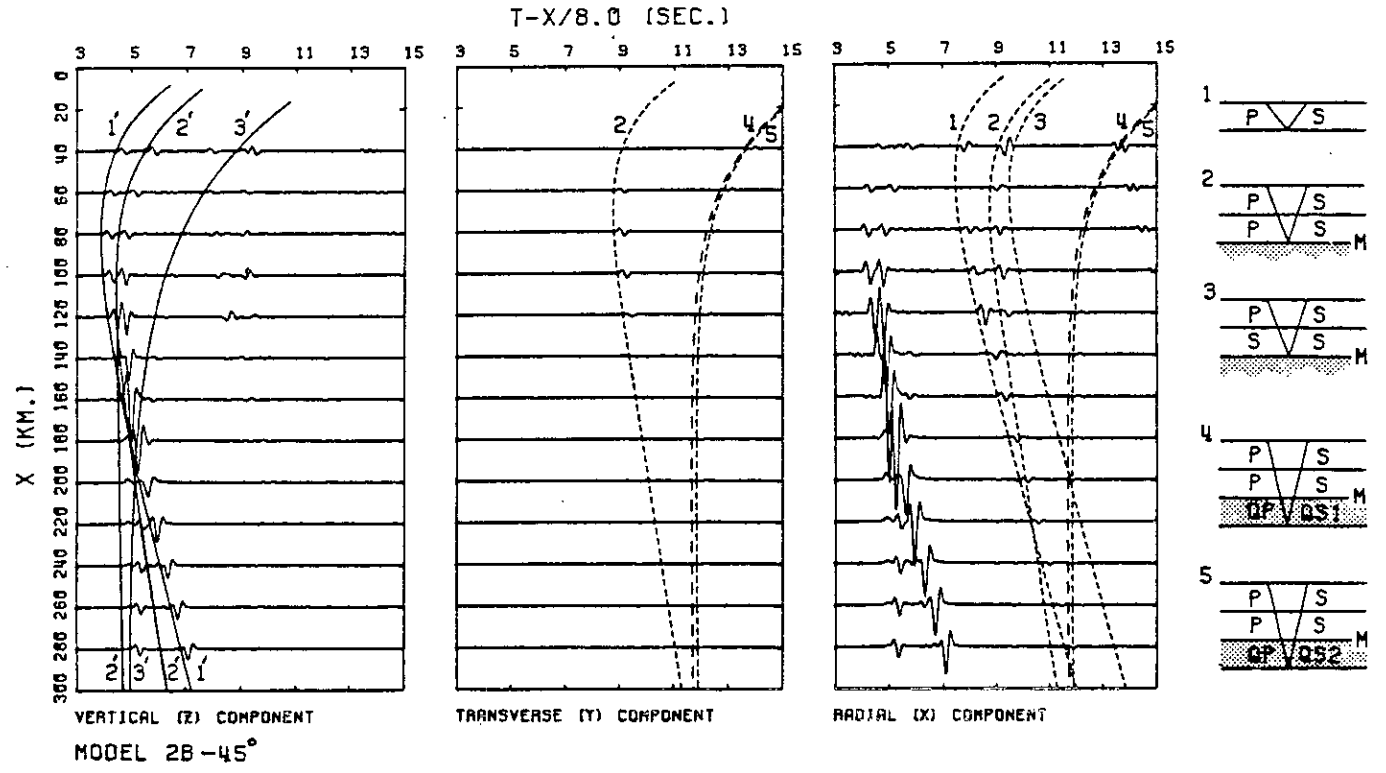
T-X/8.0 (SEC.)
X (KM.)
VERTICAL (Z) COMPONENT
TRANSVERSE (T) COMPONENT
RADIAL (X) COMPONENT
MODEL 2B-45°
1
2
3
4
5
P
S
M
QP
QS1
QS2

(b)

using models 1A, 1B, and 2C. Schematic descriptions of the wave-paths of the principal arrivals, which are numbered on the seismograms, are given in Fig.5.7.

Profiles of vertical component seismograms for model 1A at five different azimuths are shown in Fig.5.8. The principal arrival 1' is the reflected SV-wave from the top of the anisotropic layer. The arrivals 1 and 2 represent the shear-wave reflections at the base of the anisotropic layer which have travelled through it as qS1- and qS2-waves, respectively. These are the most likely anomalous arrivals to be observed experimentally. The velocity of the qS1-wave is always greater than the velocity of the qS2-wave, except along the radial axis at azimuth 0°, where the velocities are equal. Arrivals 5 and 6 correspond to single reverberations of qS1- and qS2-waves respectively in the anisotropic layer. For clarity, we identify only phases 1 and 2 at off-symmetry azimuths, although reverberations are also observed at these azimuths.

At the symmetry azimuths of 0° and 90° only one quasi-shear wave propagates in the anisotropic layer and there is no anomalous wave-energy in the transverse component. The particular type of quasi-shear wave which propagates is that which possesses the polarization of the incident SV-wave. Thus at azimuth 0°, qS1-waves propagate in the anisotropic layer, and at azimuth 90°, qS2-waves propagate. A description of the polarizations of the quasi-shear waves in a material with hexagonal symmetry has been given in section 5.4. At off-symmetry azimuths, two quasi-shear waves are generated by each incident SV-wave and both of them possess anomalous wave-energy in the transverse component. The transverse component seismograms for model 1A at off-symmetry azimuths are shown in Fig.5.9. The radial component seismograms are not shown, since the anomalous shear-waves possess neglible wave-energy in this component.

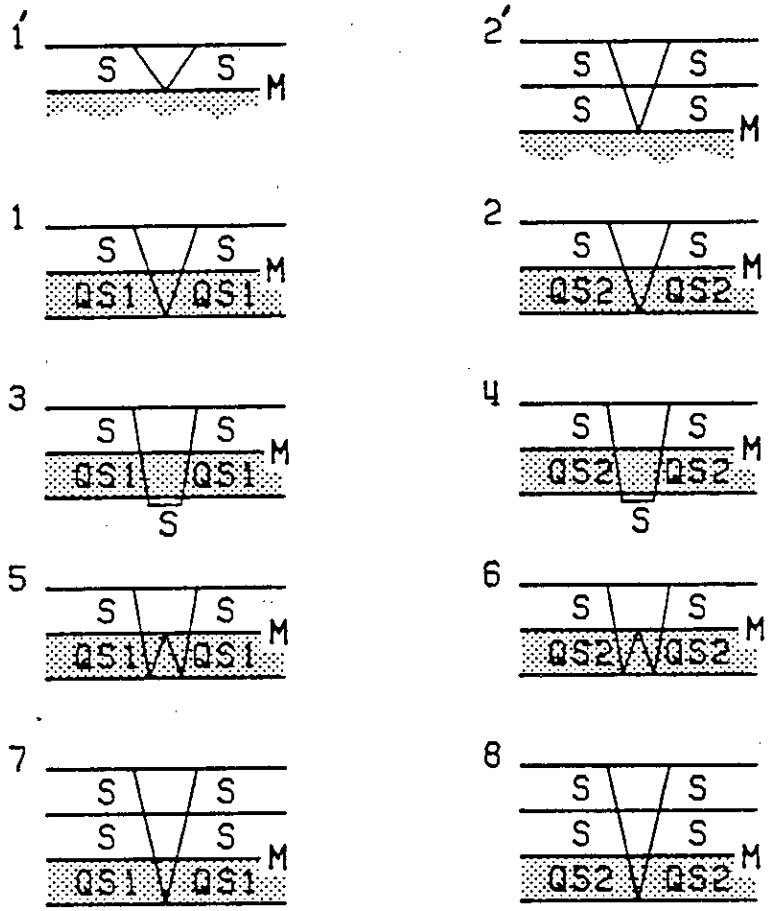

Figure 5.7 Schematic descriptions of the principal shear-wave arrivals which are identified on the synthetic seismogram sections for models 1A, 1B and 2C in Figs.5.8 - 5.11, and 5.13.

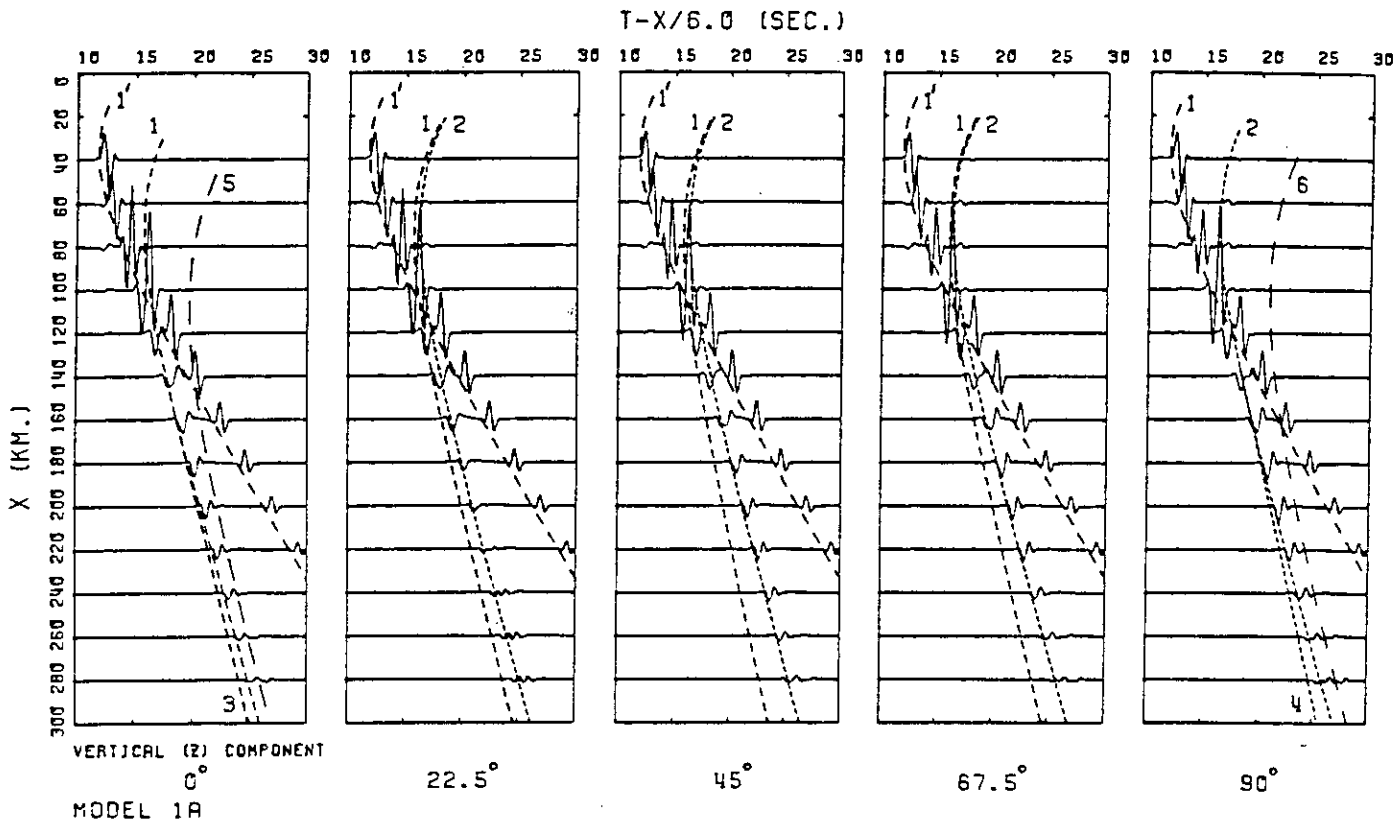

Figure 5.8 Vertical-component synthetic-seismogram sections of shear-waves generated by the SV-source in Fig.5.1(a) for model 1A at different azimuths. The arrivals which correspond to the numbered travel-time curves are described in Fig.5.7.

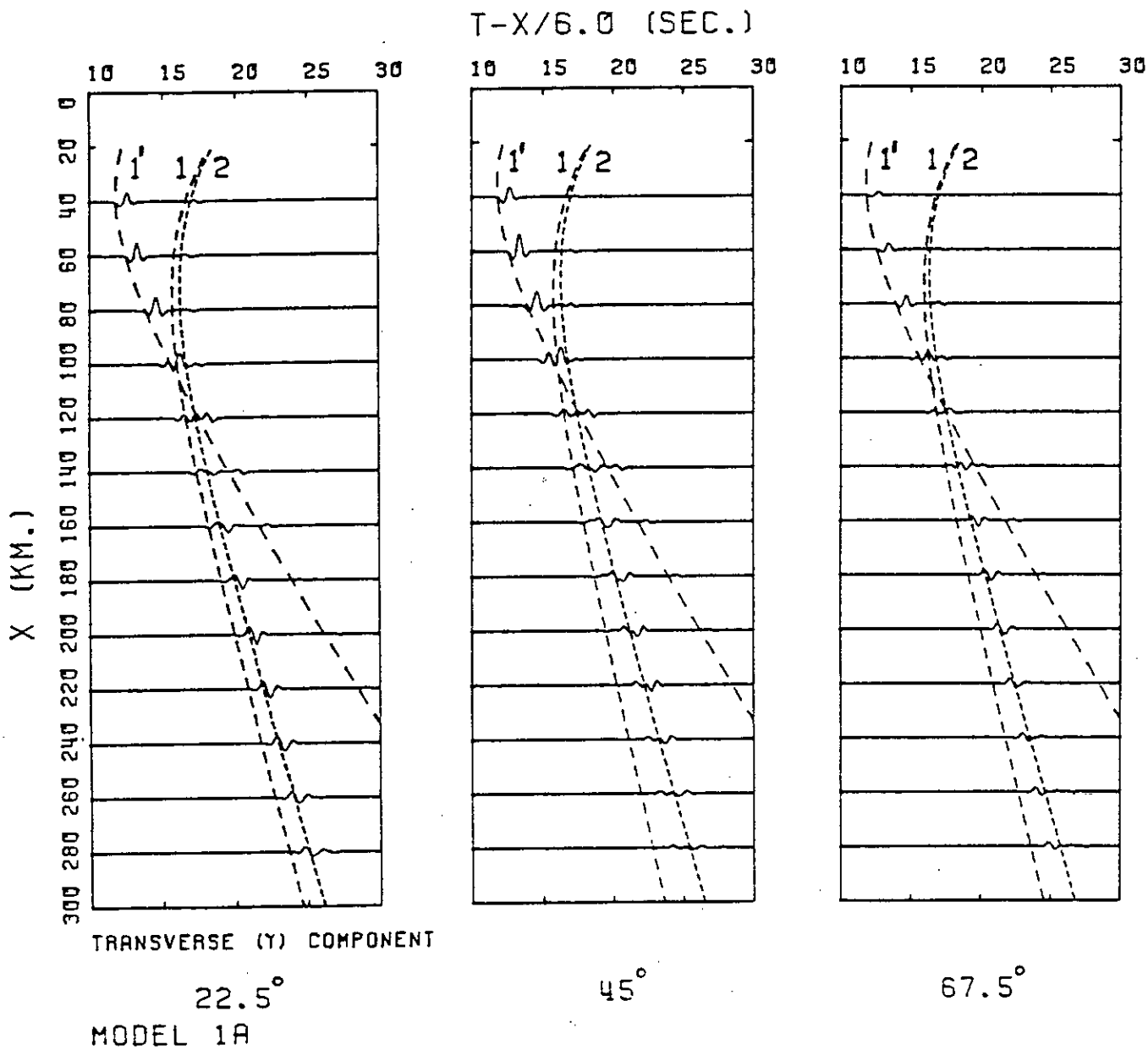

Figure 5.9 Transverse-component synthetic-seismogram sections of shear-waves generated by the SV-source in Fig.5.1(a) for model 1A at different azimuths. The arrivals which correspond to the numbered travel-time curves are described in Fig.5.7. There is no anomalous shear-wave energy in the transverse component at the symmetry azimuths of 0° and 90°.

All the phases appearing on the transverse component are anomalous. The first arrival in the distance range 40 - 100 km is an SVSH reflected wave from the top of the anisotropic layer. Its amplitude is relatively small when compared to the amplitude of the amplitude of the SVSV reflected wave which arrives simultaneously on the vertical component. The split shear-wave arrivals are seen by comparing arrivals 1 and 2 on the vertical and transverse components. For the three off-symmetry azimuths, a predominantly transversely polarized phase 1 is seen to arrive shortly before the predominantly vertically polarized phase 2.

The amplitudes of these split shear-waves which are generated with model 1A are seen to be quite small, and the amplitude of the qS1 reflected wave (phase 1) at 45° is nearly zero. The relatively weak S-wave velocity contrast between the anisotropic layer and the lower halfspace provides the reason for the low amplitude reflected wave-energy. In particular, for propagation at 45° to the symmetry axis, the velocity contrast at this interface with the lower halfspace of shear-wave velocity 4.73 km/s is virtually zero (see Fig.5.1(c)). Thus for this particular velocity structure, shear-wave splitting is not easily observed.

In order to examine the effect of a higher velocity contrast at the base of the anisotropic layer, seismograms were calculated for model 1B in Fig.5.1(a). In this model, the P- and S-wave velocities in the lower halfspace are 8.5 and 4.9 km/s respectively. These velocities are high, but not unrealistic. Ansorge et al.(1979) have detected P-wave velocities of 8.5 - 8.6 km/s at depths of 35 km and greater under Western Germany. Profiles of vertical and transverse component seismograms for model 1B, at the same range of azimuths as for model 1A, are shown in Figs.5.10 and 5.11 respectively.

By comparing Figs.5.8 and 5.10, and Figs.5.9 and 5.11, it may be seen that both split shear-wave arrivals 1 and 2 are now visible on the vertical

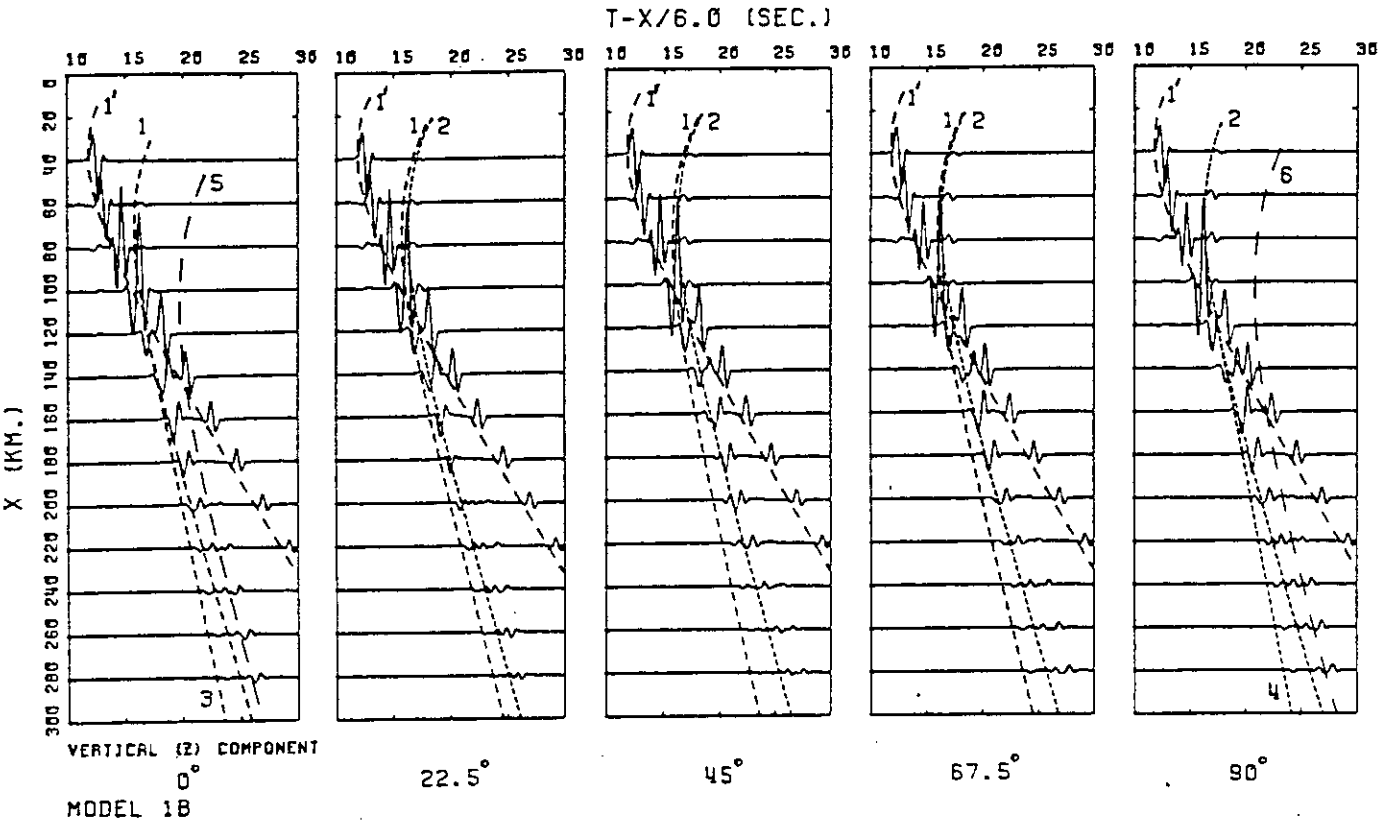

Figure 5.10 Vertical-component synthetic-seismogram sections of shear-waves generated by the SV-source in Fig.5.1(a) for model 1B at different azimuths. The arrivals which correspond to the numbered travel-time curves are described in Fig.5.7.

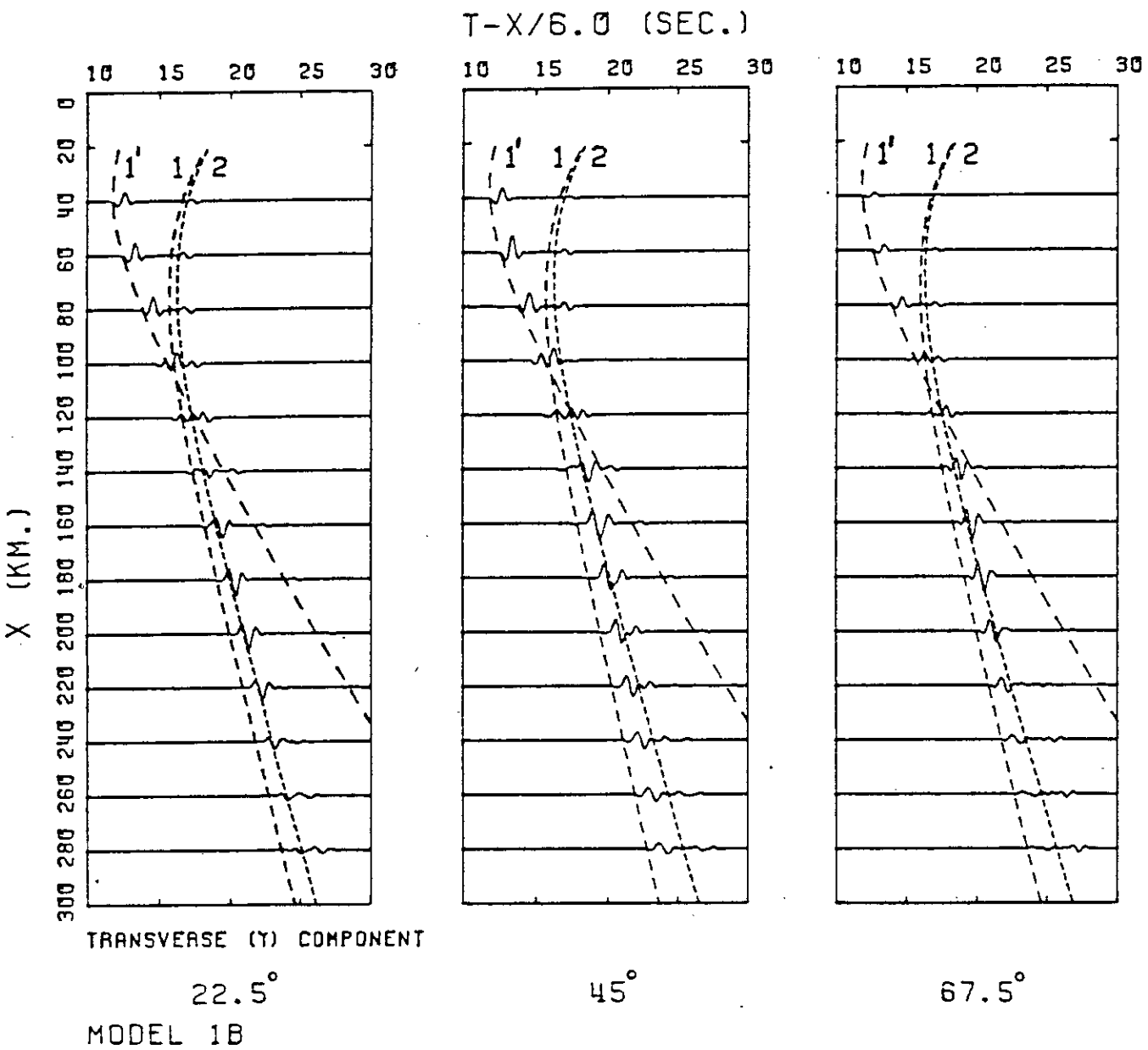

Figure 5.11 Transverse-component synthetic-seismogram sections of shear-waves generated by the SV-source in Fig.5.1(a) for model 1B at different azimuths. The arrivals which correspond to the numbered travel-time curves are described in Fig.5.7. There is no anomalous shear-wave energy in the transverse component at the symmetry azimuths of 0° and 90°.

and transverse components. These arrivals are followed by multiple reflections of the type 5 and 6 in Fig.5.7.

The near-orthogonality of the split shear-waves is verified by forming polarization diagrams from the three-component synthetic seismograms. In Fig.5.12 we show polarization diagrams of the split shear-waves at three distance ranges, for an azimuth of 45°. The principal part of the wave-energy lies in the plane formed by the vertical and transverse components, and the particle motion for this plane is given in the uppermost row of diagrams for each distance range. The orthogonal change in polarization of the shear-wave energy may be seen in the diagrams corresponding to time windows 1, 2, and 3. It is most obvious in the cruciform character of the polarizations in time window 2 for distance ranges 200 and 220 km.

In order to show that shear-wave splitting in the anisotropic layer is observable for a model crust consisting of more than one layer, in Fig.5.13 we show transverse component seismograms for the model 2C in Fig.5.1(b). The reduced velocity contrast between the crustal layers and the upper mantle allows the transmission of more shear-wave energy into the anisotropic layer. The amplitude of each of the anomalous arrivals is thus increased slightly, with respect to model 1B.

5.8 Conclusions

We have constructed synthetic seismogram profiles for compressional and shear wave point-sources, using simple models of an anisotropic, continental upper lithosphere. In these models, the anisotropy was confined to a single moderately thick (15 km) layer between a one-layer or two-layer crust and an isotropic lower halfspace. The degree of anisotropy was low, but it is probably realistic for that part of the subcrustal lithosphere. Various azimuthal profiles were computed in order to examine

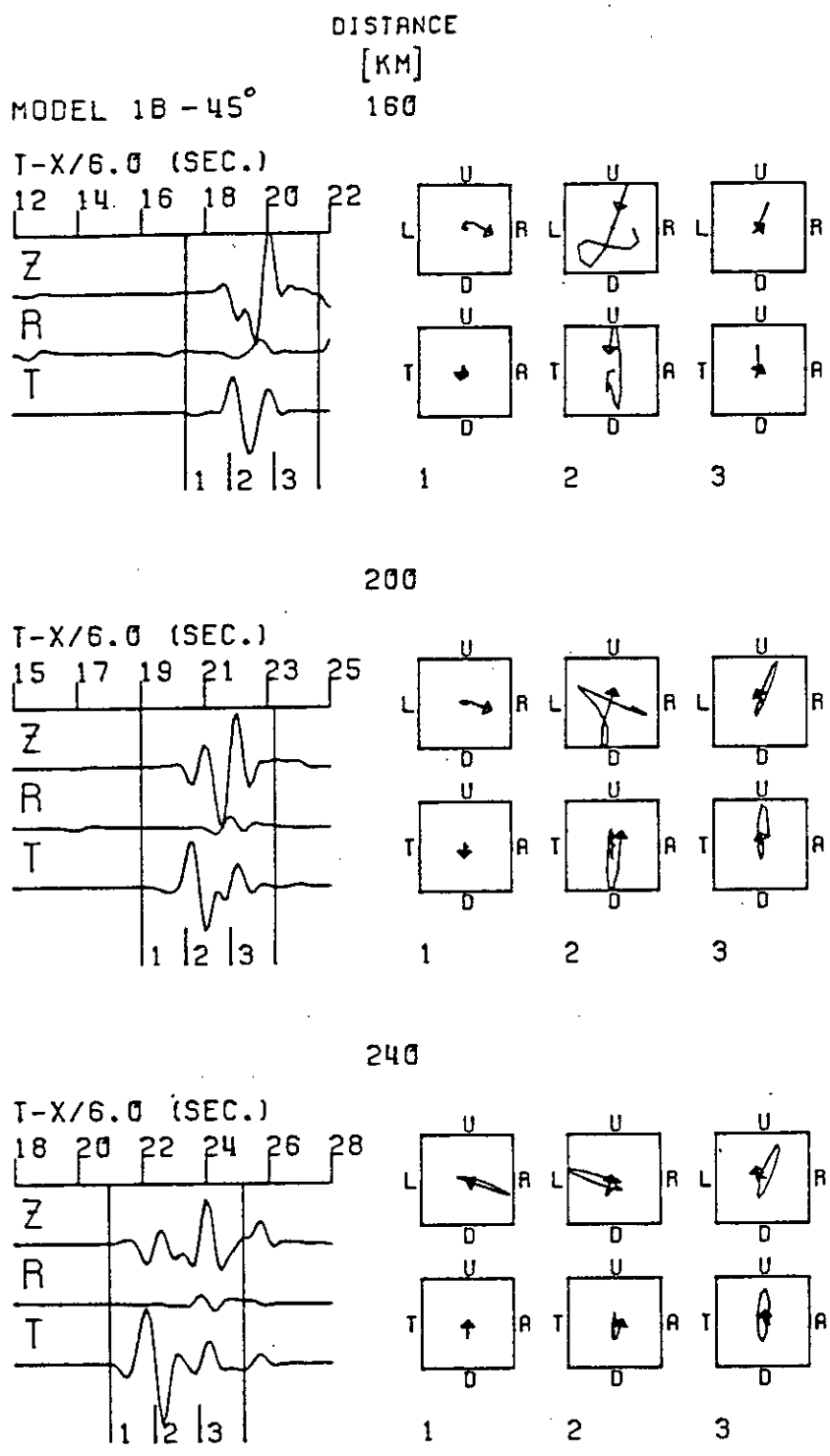

Figure 5.12 Polarization diagrams of split shear-waves at three different distances for model 1B at azimuth 45°. The labels on the polarization diagrams denote Up, Down, Towards, and Away from the source, Left and Right from the receiver. The particle motions in two of the three orthogonal planes which are formed by the component directions are plotted for the three consecutive time windows indicated on each of the three-component records.

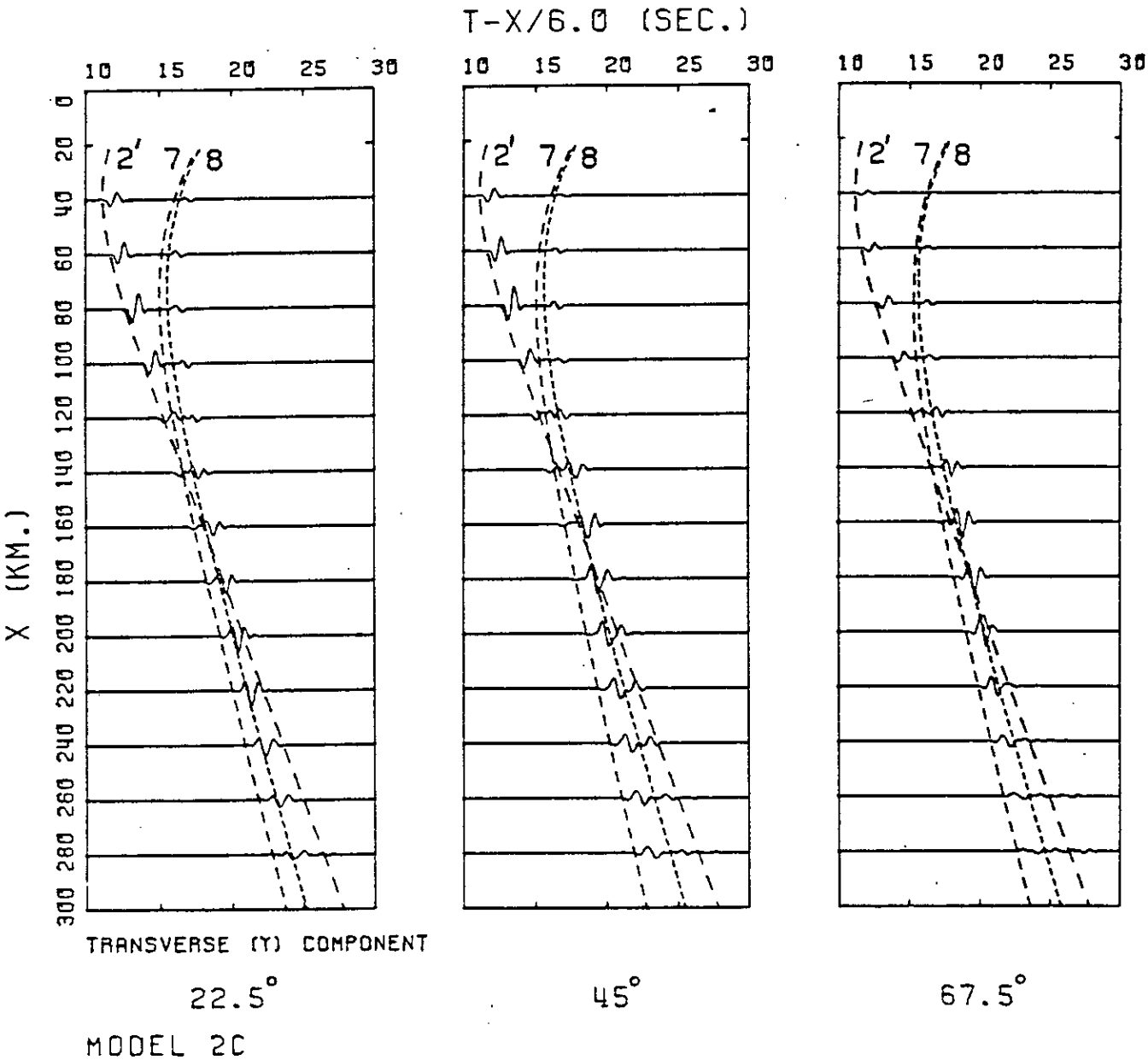

Figure 5.13 Sections of transverse component synthetic-seismograms of shear-waves generated by the SV-source in Fig.5.1(a) for the four-layer model 2C at different azimuths.

the amplitude of the anomalous arrivals which are generated when the propagation vector lies outwith a plane of sagittal symmetry in the anisotropic material.

The anomalous phases which are most likely to be generated by an explosive source are PSH converted waves. For the simple models which have been used in the present work, the largest anomalous phase is the PSH Moho reflection. The amplitude and detectability of this phase is assessed by comparing it with the amplitude of the simultaneously-arriving PSV reflection. PSV reflections at the Moho have been observed with difficulty on lithospheric refraction profiles, and only in regions where the Moho is a first order discontinuity. In such regions, for the degree of anisotropy used above, the amplitude of the largest anomalous arrival on the transverse component is likely to be one fourth of the corresponding PSV-wave amplitude. Where the Moho is a transition zone, the amplitude of the anomalous arrivals is smaller. Thus anomalous PSH reflected waves are not likely to be detected for the degree of anisotropy found by Bamford (1973,1977) under Western Germany.

Where the Moho is not a first order discontinuity but a transition zone, the amplitude of the anomalous arrivals can be of the same order of magnitude as the non-anomalous arrivals. However, this occurs only over a limited distance range, and in any case the absolute amplitude of the anomalous arrivals is very small. It is not likely that the anomalous arrivals could be identified unambiguously, particularly for azimuths which are close to symmetry axes.

The unexpectedly high P-wave velocities sometimes found in the lower lithosphere (Ansorge et al.1979) may indicate the presence of a stronger degree of anisotropy, due to an increase in the preferred alignment of olivine at depth. It is difficult to be optimistic about the use of anomalous PSH converted waves to detect anisotropy from individual

three-component seismograms, even if stronger anisotropy is present. However, profiles of transverse records might enable the largest anomalous phases to be correlated, and thus supplement information gained from any observation of azimuthal velocity-variations.

The presence of split shear-waves with orthogonal polarizations is likely to be a more reliable indicator of anisotropy. The principal split shear-waves for a local source will be reflections from the base of the anisotropic layer at off-symmetry azimuths. The amplitude of each reflected quasi-shear wave depends critically on the velocity contrast at this interface. It has been shown that one of the anomalous reflected quasi-shear waves may vanish at an off-symmetry azimuth, if the corresponding velocity contrast becomes zero. Thus shear-wave splitting could easily remain undetected, even for an anisotropy which is stronger than that used for the models in Fig.5.1.

The amplitude of the split shear-wave arrivals which were generated from models 1A and 1B in Fig.5.1(a) are rather small. This is due to a large amount of the incident SV energy being reflected from, rather than transmitted into, the anisotropic layer. The results obtained with model 2C suggest that a transition zone above the anisotropic layer with a high velocity contrast below it would increase the amplitude of the reflected quasi-shear waves. The observational results of Edel et al.(1975) and Ansorge et al.(1979) support the existence of such a structure under Western Germany, but we have not investigated such a structure in this preliminary study. At present it is expensive to model such multilayered structures adequately with the anisotropic reflectivity technique.

The same constraint applies to an analysis of fine structure in the lithosphere, in terms of a multilayered model comprised of anisotropic media with varying orientations. This structure has been proposed by Meissner & Flüh (1979) as an explanation of the lithospheric fine

structure which has been deduced from several long-range refraction profiles. The identification and analysis of anomalous arrivals would be very difficult for such a structure.

Additional complications include the extent to which the anomalous shear-wave arrivals are immersed in seismic noise generated by the P-coda, and the radiation pattern of the source. Explosive sources generate extremely small amounts of shear-wave energy. Hirn (1977) has found some evidence of shear-wave splitting on long-range profiles from two explosions at sea. However, his results are not sufficiently conclusive to indicate that analysis of shear-wave splitting with explosive sources is likely to be profitable.

Earthquake sources generate very much larger amounts of shear-wave energy, and offer much more promise for diagnosing shear-wave splitting. However, nodes in the radiation patterns will affect the observations. The orientation of the double-couple source which was used to generate the shear-wave seismograms in section 5.7 was favourable for the generation of SV-wave energy at appropriate angles of incidence for the distance range. However, if the source and its SV-wave radiation pattern were rotated by a further 45° about the transverse axis, then the amount of SV-wave energy incident at these angles would be very much less.

If the double-couple was oriented at some angle to the sagittal plane, then SH-wave energy as well as SV-wave energy would be radiated in the sagittal plane. Thus the relative proportions of qS1- and qS2-wave energy generated in the anisotropic layer will vary according to the orientation of the source as well as the orentation of the anisotropic material. The velocity contrast at the base of the anisotropic layer is still crucial in determining the amount of reflected qS1- and qS2-wave energy.

The principal difficulty associated with the use of earthquakes as shear-wave sources is that their location and origin-time are not

controlled. It is difficult and expensive to maintain an adequate azimuthal station coverage, even for a known seismic area. Digital or digitisable networks of short-period three-component seismometers are required, and these are scarce. Thus although the presence of shear-wave splitting is not dependent on the degree of anisotropy, this advantage is offset by the restrictions associated with the shear-wave sources, and by the recording requirements.

The analysis of subcrustal lithospheric anisotropy by the observation of shear-wave splitting on individual three-component seismograms from explosion or earthquake sources is judged to be marginally feasible. However, it appears that it requires careful analysis of a large body of azimuthal data , needs a complete knowledge of crustal inhomogeneities, and is unlikely to be successful except in exceptionally favourable conditions.

CHAPTER 6

A STUDY OF WAVE-MOTION IN A CRACKED CHANNEL

6.1 Introduction

In the previous chapter, we applied the anisotropic reflectivity technique to an upper-mantle model, where both the seismic source and receiver lie above the plane-layered, anisotropic reflection zone. We shall now apply the technique to a model where the receiver lies within the anisotropic reflection zone, and the source is located in an isotropic halfspace outside the reflection zone.

The experimental situation which has provided the motivation for this model is interesting. It arises from a project for the extraction of geothermal energy from hot dry rock at a depth of 2500-3000 metres. Briefly, the project requires the creation of a particular system of major-cracks and micro-cracks in the hot dry rock. The pattern of cracks then forms a circulation path and a heat transfer system for fluid injected from the surface. The project is described in more detail in the next section.

At the depth of the geothermal reservoir, seismic methods are likely to provide the most effective means of mapping the extent and the geometry of the crack system. Acoustic events have been recorded in the course of the project on a three-component downwell geophone, and the seismograms show some unusual features. The nature of the seismograms, and the restricted information which is available on the crack geometry, suggest that a particular stratified theoretical model could be used in an attempt to model the observed seismograms.

The theoretical model consists of a channel between two thin plane water-filled fractures, surrounded by isotropic halfspaces. It is believed that the channel is permeated by aligned water-saturated microcracks caused by thermal contraction, and thus it is anisotropic. The receiver is located within this anisotropic channel. If we can take the seismic source to lie in one of the isotropic halfspaces, then we can use the anisotropic reflectivity technique described in chapter 3 to calculate theoretical seismograms at any receiver depth in the anisotropic channel. The anisotropic reflectivity technique provides the only means of modelling the observed seismograms which allows for anisotropy in the model structure.

The theoretical model, the assumptions which are made in setting it up, and the computational technique are described more fully in two sections immediately after the description of the hot dry rock project. It will be seen that we find it useful in the investigation of P- and SV-wave first arrivals to truncate the complete response in the channel to that of the direct waves and the first multiple reflections, and thus avoid interfering time-aliasing effects. We use truncated seismograms to investigate the polarization of the first P-wave arrivals, converted wave precursors to the direct SV-wave arrival, and the formation of the early part of the SV-wave coda. Truncated SV-wave seismograms are also constructed for two other model structures, in order to examine the effects of making the channel isotropic, and eliminating the liquid layers which simulate the plane water-filled fractures which bound the channel. The study of these effects is continued when we use the complete response in the channel to construct seismograms of SV- and SH-wave reverberations. We examine the wave arrivals at different receiver positions within the channel and compare the shear-wave codas with the distinctive shear-wave codas which are observed experimentally.

6.2 The LASL Hot Dry Rock (HDR) Project

Under many normal continental areas, geothermal energy is present in great quantities at depths which are accessible with modern drilling techniques. The geothermal energy can be extracted if it is possible to establish a circulation of fluid through the hot rocks to the surface.

The hot rock at depth is virtually impermeable, and therefore does not itself contain any fluid for circulation. It is necessary to create an artificial circulation path through the geothermal reservoir and to use fluid pumped in from above to accomplish the transfer of energy from the hot dry rock to the surface.

An experimental project for the extraction of HDR geothermal energy is under way at Fenton Hill, New Mexico, operated by the Los Alamos Scientific Laboratory (LASL). Full details of the project are given in the annual reports of the LASL HDR Geothermal Energy Development Program (eg. Cremer 1981). In this chapter we shall confine ourselves here to a description of the origins and the geometry of the circulation path, which is shown in Fig.6.1.

The borehole EE-1 was driven into the geothermal reservoir to a depth of 3000m, where the rock temperature was 200^{o}C. Hydraulic pressurization of an uncased section of the borehole EE-1 at depth 2750m produced a large plane fracture. The plane of the fracture is nearly vertical, since it will be orthogonal to the minimum component of the ambient tectonic stress, which is expected to be horizontal at this depth. The fracture is believed to be roughly circular in shape, and about 100m in diameter. The borehole GT-2B was driven to a depth of 2705m in an attempt to intercept this fracture. It is believed that GT-2B missed the fracture, but intercepted some non-vertical natural joints which completed a circulation path between GT-2B and the fracture initiated from EE-1. In March 1978 a second,

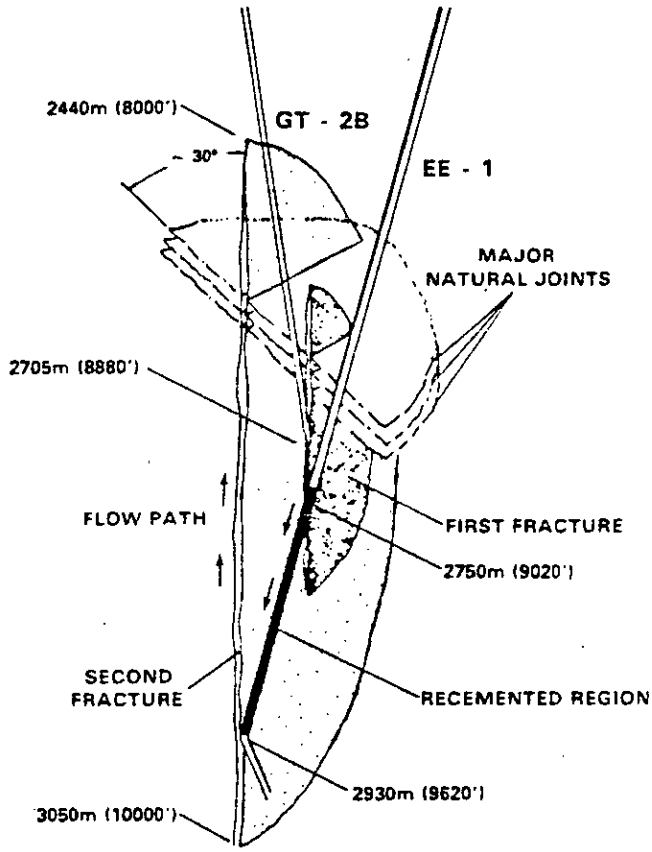

Figure 6.1 The inferred geometry of the circulation path in the geothermal reservoir. The boreholes GT-2B and EE-1 are connected by a system of natural joints and two large parallel fractures. These fractures were created by two separate hydraulic pressurizations of the borehole EE-1. (After Cremer 1981)

larger, fracture was initiated from EE-1 at a depth of 2930m in order to extend the area of contact between the hot rock and the fluid. This second crack also connects with the natural joints, as shown in Fig.6.1, and is orthogonal to the direction of minimum tectonic stress. The diameter of this crack is estimated to be 300m. The thickness of the slab of rock between the two major cracks is estimated to be of the order of 10m, from the results of wellbore surveys carried out in 1977 (Aamodt et al., in LASL HDR Project Staff 1978). The slab is likely to be cracked as the result of thermal contraction on cooling during pressurization of the circulation system.

Fehler (1981) has observed a reduction in the P-wave velocity in the geothermal reservoir after pressurization, and he attributes this to the formation of microcracks by thermally-induced stress as heat is removed from the system. From the hyperbolic form of an observed travel time-distance graph, Fehler (1981) deduces that there is neglible angular variation of velocity, and he does not discuss any possible alignment of the microcracks. However, Crampin & Radovich (1982) have shown that such time-distance graphs will be very close to hyperbolae in weakly anisotropic media. Thus Fehler's observations do not preclude the presence of anisotropy. The geothermal reservoir is likely to be anisotropic because the thermal contraction cracks are unlikely to be randomly aligned.

Further evidence for the existence of small-scale extensive cracking has been presented by Aki et al.(1982). Before the second major fracture was created, a series of experiments were carried out in the geothermal reservoir under pressurized and unpressurized (hydrostatic) conditions. Aki et al. found that the mean square fluctuation of P-wave arrival time and Q^{-1} of coda waves increased by nearly the same amount on pressurization of the reservoir. They attributed this result to a heterogeneity of the volume surrounding the large-scale crack system. In

particular, they concluded that scattering by the heterogeneity due to small-scale cracking is the major cause of attenuation within that volume. The scale-length of these cracks was estimated to be of the order of 3m, from the frequency dependence of the attenuation. However, Aki et al. did not comment on the probable anisotropy of the small-scale crack system.

Before the second major fracture was initiated by hydraulic pressurization in EE-1, a three component geophone package was installed at a depth of 2695m in GT-2B. Many microseismic events were recorded during pressurization, and a sample of the three component records which were obtained from five such events are shown in Fig.6.2. It has been deduced from the S-P travel-time differences that these events occurred at distances of 110-210m from the geophone package. It was not possible to determine the precise position of the geophone, or the orientation of the geophone components with respect to the crack geometry. All that is known is that component V is parallel to the borehole, and therefore it is approximately vertical, and parallel to the planes of the two major cracks.

It is seen from the seismograms in Fig.6.2 that there is a difference in the frequency content of the shear-wave coda between the vertical and horizontal components. However, the principal characteristic of most, but not all of the seismograms is the large amplitude, low frequency wavetrain which begins at, or soon after, the onset of the first shear-waves. The particle motion of this wavetrain, which propagates with no measurable dispersion and suffers very little attenuation, is polarized principally in the vertical direction, and thus approximately parallel to the planes of the major cracks. Crampin (1980, personal communication) suggested that this characteristic wavetrain could be due to the presence of the two closely-spaced, parallel, water-filled cracks, which would form a natural waveguide or channel for shear-waves.

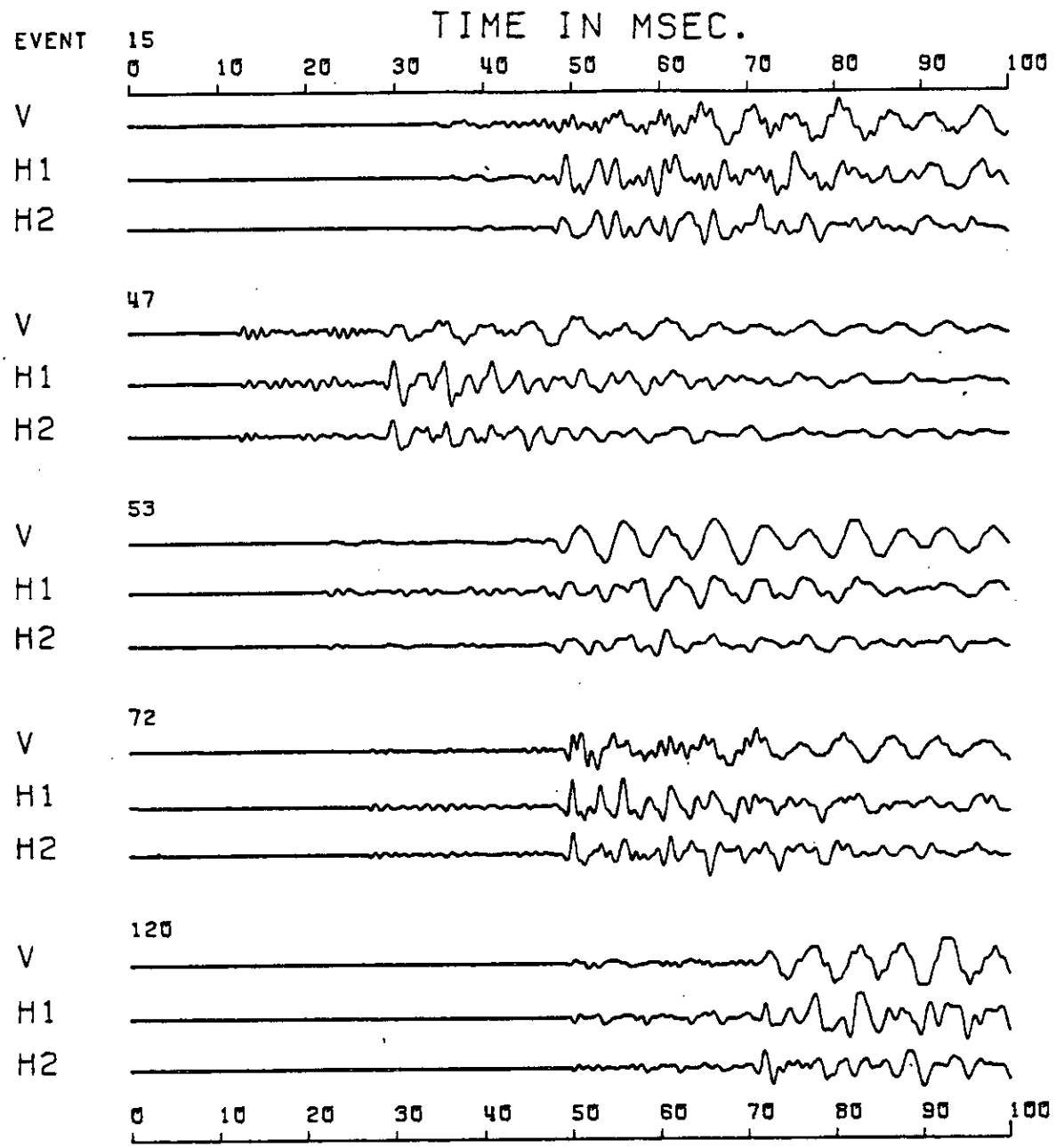

Figure 6.2 A selection of seismograms of microseismic events recorded by a three-component geophone package in GT-2B during pressurization of EE-1. The V component is parallel to the axis of borehole GT-2B. The horizontal components H1 and H2 are orthogonal to V, but their exact orientation is not known.

The effects of such a channel may be investigated by the generation of synthetic seismograms for a suitable model of the structure. The slab of rock between the two large cracks will be cracked by thermal contraction, and thus anisotropic. Provision should be made for this probable anisotropy in the generation of the synthetic seismograms. The anisotropic reflectivity technique which has been formulated in Chapter 3 is suitable for the generation of synthetic seismograms for a receiver in a cracked channel. The model which was used to investigate the effects of a cracked channel is described in the next section.

6.3 A theoretical model of a cracked channel

A simplified model of the water-filled crack structure at Fenton Hill is shown in Fig.6.3(a). Cooling of the major cracks is assumed to cause hexagonal columnar cracks to form between and out from the major crack-faces, and perpendicular to these faces. Thus the slab between the major cracks is an anisotropic medium with hexagonal symmetry. The medium can be modelled by a random distribution of saturated cracks, in an otherwise homogeneous isotropic matrix, with the crack normals parallel to the major crack-faces (Crampin 1978). The axis of symmetry of this system of saturated cracks with coplanar normals is orthogonal to the major crack-faces. The velocity variations with respect to this axis are given in Fig.6.3(b) for a crack density of 0.1 in an isotropic matrix with Vp and Vs equal to 5.8 and 3.35 km/s, respectively, and ρ = 2.6 gm/cc. A crack density of 0.1 is equivalent to one 9mm diameter crack in each cubic centimetre.

We take the origin of the coordinate axes to coincide with the source S on the periphery of the major crack C1. The axes are x_1 radial along the crack C1 towards the geophone G, x_3 normal to the major crack-faces, and x_2

Figure 6.3(a) A simple model of the cracked reservoir. G is a three-component geophone between two major parallel water-filled cracks C1 and C2, and S is the source of an event occurring on the periphery of the crack C1. The co-ordinate axes are x_1 radial towards the geophone, x_2 parallel to the crack, and x_3 normal to the major-crack faces. Columnar saturated cracks with a hexagonal cross-section are assumed to form in the 10 m thick slab between C1 and C2, due to thermal contraction. This cracked medium is modelled by anisotropic hexagonal symmetry with the axis of symmetry normal to the major-crack faces.

(b) Velocity variations in the homogeneous anisotropic material which models the cracked slab. It is modelled by a random distribution of saturated cracks, with coplanar normal vectors (coplanar normal saturated cracks, CPNSACR), in an isotropic matrix. The elastic constants are given in Table 6.1 , for a crack density of $N\underline{a}^3/V = 0.1$, where N is the number of cracks of radius $\underline{a}$ in a volume V.

(c) The model structure: two major 1mm thick water-filled cracks C1 and C2 on either side of a cracked slab which is modelled by an anisotropic medium with hexagonal symmetry, of thickness H m. The geophone position Gd is located at a depth of d metres in the channel. The radiation patterns of P-waves (solid line) and SV-waves (dashed line) are illustrated for the tension crack mechanism which is used to model the source S. Direct contact of the cracked channel and upper isotropic halfspace is assumed for the transmission of SV-wave energy into the cracked channel. The structure which is illustrated is model A; models B, C and D are described in Table 6.3 in terms of simple variations on this structure.

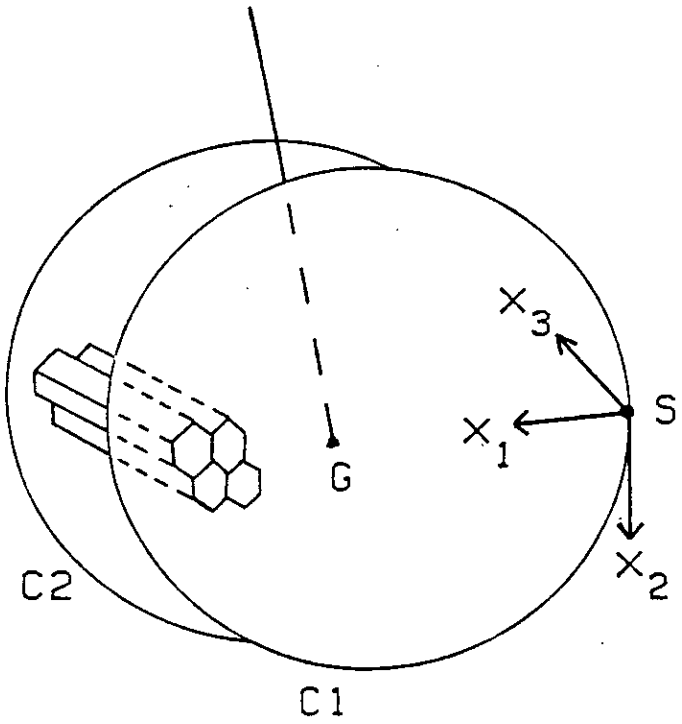
X3
S
X1
G
X2
C2
C1

(a)

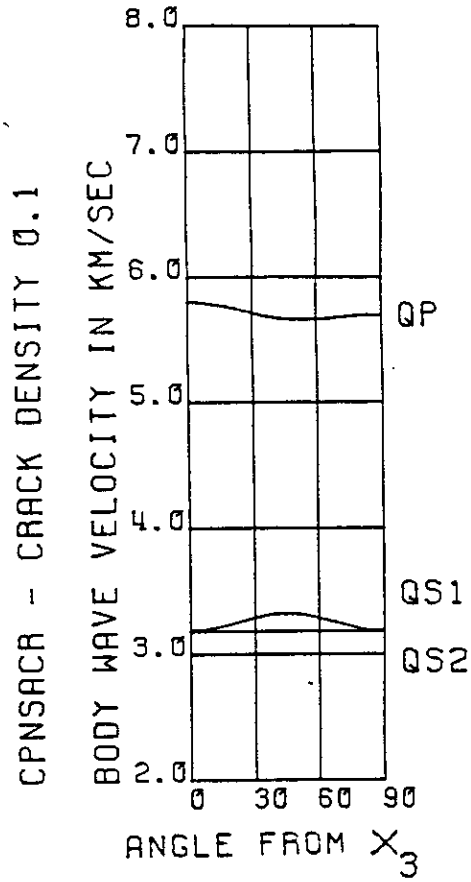
8.0
7.0
6.0
5.0
4.0
3.0
2.0
QP
QS1
QS2
CPNSACR - CRACK DENSITY 0.1
BODY WAVE VELOCITY IN KM/SEC
0
30
60
90
ANGLE FROM X3

(b)

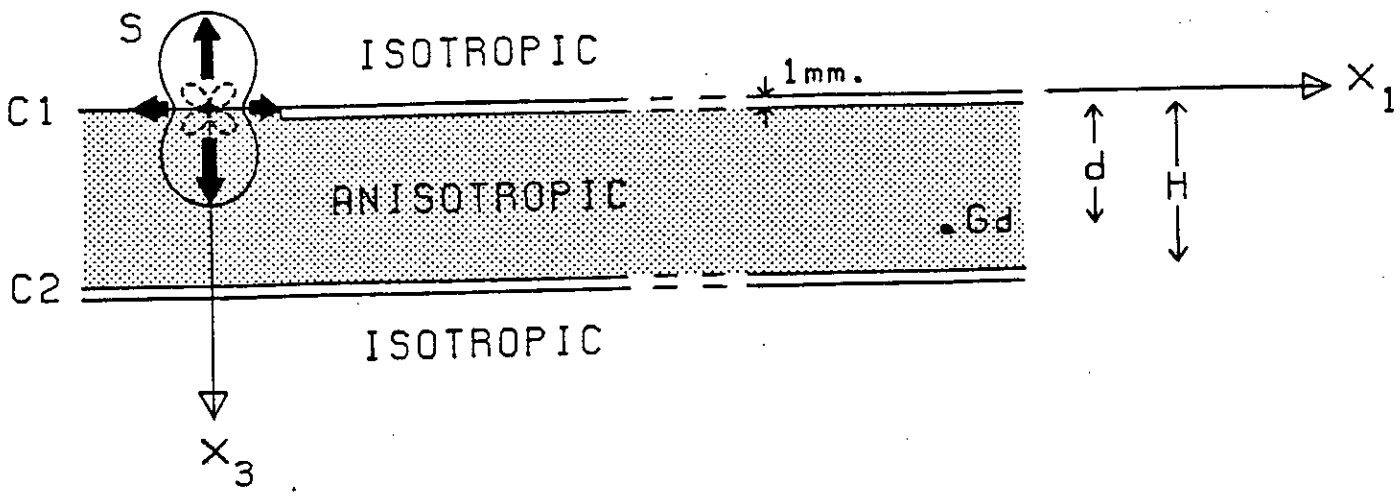
S
ISOTROPIC
1mm.
X1
C1
ANISOTROPIC
Gd
d
H
C2
ISOTROPIC
X3

(c)

orthogonal to x_1 and x_3, and in the plane of crack C2. The axis of symmetry of the anisotropic medium is parallel to the x_3 axis and the elastic constants for this alignment are given in Table 6.1. We shall see in the next section that it is desirable to introduce a small complex part to the elastic constants in order to make the medium slightly attenuative. Thus we add a complex part 0.05i to each elastic constant in Table 6.1, which corresponds to the application of specific dissipation factors $1/Q_\alpha$, $1/Q_\beta \leqslant 1/600$ (Crampin 1981).

The sagittal plane of the theoretical model is a symmetry-plane of the hexagonally anisotropic material. Therefore there will be no coupling of the P- and SV-wave motion with the SH-wave motion, and no anomalous converted phases such as P to SH, or SV to SH, will be generated. However we should expect to see slight differences in seismograms computed for a cracked and an uncracked channel, due to the angular variation of P- and SV-wave velocities in the sagittal plane and the lower velocity of SH-waves in the cracked material.

The liquid layer is represented by an elastic medium with a P-wave velocity of 1.5 km/s, an S-wave velocity of 0.001 km/s, and a density of 1.0 gm/cc. In order to check this approximation to a liquid layer, reflection and transmission coefficients at a solid/liquid interface were calculated using the above parameters, and compared with equivalent coefficients calculated by exact methods (Brekhovskikh 1960). The coefficients were identical to three decimal places. Müller & Kind (1975) used a material with a very low S-wave velocity and a low P-wave velocity to model a gaseous halfspace, and obtained satisfactory results.

In Fig.6.3(c) we show a sectional view of the layered structure which we shall refer to as model A. The structure takes the form of a cracked channel, or waveguide, between two thin, parallel, fluid-filled, cracks C1 and C2. There is every reason to believe that the halfspaces on either

Table 6.1 Elastic constants of the anisotropic material with hexagonal symmetry which models the cracked slab: a random distribution of coplanar normal saturated cracks in an isotropic matrix with $\alpha = 5.8$, $\beta = 3.35$ km/s, and $\rho = 2.6$ gm/cm^3. The crack density is $Na^3/V = 0.1$, where N is the number of cracks of radius a in a volume V. The axis of symmetry is parallel to the x_3 axis.

$c_{1111} = 84.368$	$c_{2222} = 84.368$	$c_{3333} = 87.464$
$c_{2233} = 28.387$	$c_{3311} = 28.387$	$c_{1122} = 31.483$
$c_{2323} = 26.443$	$c_{1313} = 26.443$	$c_{1212} = 26.443$

side of the channel are also cracked and anisotropic in the vicinity of the major fractures C1 and C2. However we have not developed the anisotropic reflectivity technique for the case where the source lies within the layered structure, nor can we give a satisfactory representation of a source in an anisotropic medium. Therefore we locate the source S immediately outside the layered structure, in one of the halfspaces outside the cracked slab. We also assume that the medium comprising this halfspace is the homogeneous isotropic material which is cracked within the channel.

As there are computational advantages in calculating seismograms for a structure which is symmetrical about the layer containing the receiver, we take the halfspace on the other side of the channel to be of the same isotropic material. Direct contact of the cracked channel and the isotropic halfspace is assumed in the immediate region of the source, in order to allow the transmission of shear-wave energy from the source into the cracked channel.

For studies of P- and SV-wave propagation in the channel, we assume that the source is a tension crack in this isotropic matrix. A tension crack may be represented by three orthogonal vector dipoles, with relative amplitudes $1:1:(\lambda + 2\mu)/\lambda$ given in terms of the Lamé constants of the isotropic material (Aki & Richards 1980, p.53). We take the principal vector dipole to be directed along the x_3 axis, and the resulting source radiation pattern for P- and SV-waves is illustrated in Fig.6.3(c). The source function S_j, to be substituted in equation (2.5.2), is given in Table 6.2 for P- and SV-waves emanating from this source.

A tension crack source was chosen at the time the P- and SV-wave studies were made, because the most likely source mechanism was then thought to be that of a flat crack in the plane of the fracture opening against the minimum compressive stress under high pore pressure. Recent work by Pearson (1981) shows that the microseismic events are probably

Table 6.2 Values of S_j for P- and SV-waves for the tension crack point-source in Figure 6.3(c) in terms of the wavenumbers k, k_1, k_2, v_1, and v_2. $f = \lambda/(\lambda + 2\mu)$, where λ and μ are the Lamé constants of the isotropic medium in which the source is located. $D = -1/4\pi\rho\omega^2$

P: j=1	SV: j=2
$\frac{Dkk^3_1}{v_1}\left(\frac{v_1^2 + fk^2}{k_1^2}\right)$	$\frac{-Dkk^3_2}{v_2}\left(\frac{kv}{k_2^2}\right)(1-f)$

caused by shear failure on planes of weakness surrounding the hydraulic fracture, rather than tensile failure at the fracture's expanding edge. However it will be shown that the most interesting features of the synthetic seismograms of P- and SV-waves are not likely to be crucially dependent on the character of the source.

We shall assume that SH-waves are generated by horizontal strike-slip motion along a vertical crack in the plane $x_1=0$. Then the radiation pattern for SH-waves is that of a horizontal single-couple in the plane $x_3=0$, with force vectors parallel to the x_2 axis. The corresponding source function is given by the SH-wave term in Table 2.2 for a single-couple, after a rotation of 90° about the x_3 axis followed by a rotation of 90° about the x_2 axis.

We shall describe the position of the receiver geophone G in terms of its distance in metres from the crack C1 containing the source. Thus the receiver G5 is positioned 5 metres from C1. The thickness of the cracks C1 and C2 is taken to be 1mm and we set the thickness of the cracked slab, H, to be 10m in the case of model A. Synthetic seismograms will also be constructed for other models, labelled B to D, in order to illustrate the effects of slight differences in the model structure. The distinguishing features of the different models are described in Table 6.3, in terms of the sectional model in Fig.6.3(c).

6.4 Computational details

Synthetic seismograms are to be calculated for arrivals at a receiver within a stratified reflection zone, which may be anisotropic, using a point source located in an isotropic medium outside the reflection zone. In chapter 2 we have shown how the component displacement spectra of each wave-type in an anisotropic layer can be expressed as an integral of plane

Table 6.3 Distinguishing features of models of a cracked channel, with respect to Figure 6.3(c).

PARAMETERS	MODEL			
	A	B	C	D
Medium representing cracked slab	anisotropic	isotropic $a = 5.8$	anisotropic	anisotropic
Thickness of major cracks (mm)	1	1	0	1
Thickness H of cracked slab (m)	10	10	10	20

wave displacements as in equation (2.5.2). Expressions for the displacement excitation factors of upward and downward propagating plane waves in the anisotropic layer were given in equation (3.6.9) in chapter 3. The iterative calculation of the three coefficient matrices in equation (3.6.9) would be very time-consuming for a model involving more than two or three layers. However, the model in Fig.6.3(c) is symmetrical about the layer containing the receiver, and we have shown in section 3.8 how the calculation of the excitation factors is then reduced to two iteration procedures.

Further, we assume that the waterfilled crack C1 does not separate the anisotropic layer from the upper halfspace in the immediate region of the source, which lies just within the upper isotropic halfspace in Fig.6.3(c). This assumption is made in order to allow the transmission of shear-wave energy into the channel between the waterfilled cracks. Otherwise, the thin fluid layer would reflect all the shear-wave energy away from the channel. We believe that this assumption is reasonable for events which occur on the periphery of the major cracks. It also allows the matrix of downward transmission coefficients from the source layer into the anisotropic layer to be given by the downward transmission coefficients for a single interface. Thus only one iteration procedure is required during the calculation of the excitation factors in the receiver layer.

When we calculate the excitation factors for model C, where the thin waterfilled cracks are absent, iterative calculations are not required. In that case the interface reflection and transmission coefficients at the boundary of the anisotropic layer may be substituted directly into the equation (3.6.9) for the excitation factors.

In each layer we may truncate the complete response, which includes all multiple reflections and phase conversions, to that of the direct waves, or the direct waves plus first reverberations, as described in

section 3.6. This option is particularly useful when we are considering the type of structure in Fig.6.3(c), with a low-velocity channel. Reverberations invariably extend over a longer time window than is available for calculation, which leads to time-aliasing effects on the synthetic seismograms. The time-aliased arrivals obscure early arrivals, and frequently interfere with the principal arrivals. Thus truncation of the reverberations is very useful when we wish to investigate small, early arrivals. Truncation is enforced when the channel is completely elastic, since otherwise the integral in (2.5.2) could involve integration through poles of the secular function given by the matrix $(I - {}^{m}\mathcal{R}_{U}^{0}\,{}^{m}\mathcal{R}_{D}^{n})$ in equation (3.6.9). In practice, we move the poles of the secular function off the path of integration by making the channel slightly attenuative. This permits the calculation of the complete reflected wave response in the channel, when it is required.

Except where otherwise stated, the seismograms are calculated over a 30ms time-window, with a signal of principal frequency 900Hz, which is the average frequency of the compressional waves on the seismograms recorded by LASL (Fig.6.2).

6.5 P-wave arrivals: direct waves and first reverberations

Synthetic seismograms of the P-wave arrivals which are due to the compressional part of the tension crack radiation pattern are shown in Fig.6.4 for receivers at G1, G5 and G9 in model A. The radial and normal components correspond to the axes x_1 (radial from the source along crack C1) and x_3 (normal to the major-crack faces), which are illustrated in Fig.6.3(c). In forming these seismograms, the response in the cracked channel has been truncated to that of the direct waves, and the first multiples and converted waves. The truncated P-wave response, and the

Figure 6.4 Normal and radial component seismograms of P-waves from a tension crack point-source, for receiver positions G1, G5, and G9 in the cracked channel model A of Table 6.3. The response in the channel has been truncated to that of the direct waves and the first multiple reflections. Travel-time curves with a long dash denote direct or reflected P-wave arrivals: curves with a short dash indicate that conversion to SV-waves has taken place over part of the wavepath. The wavepaths of the labelled arrivals are identified schematically in Fig.6.5. Arrowed arrivals are numerical phases associated with the limits of the integration window.

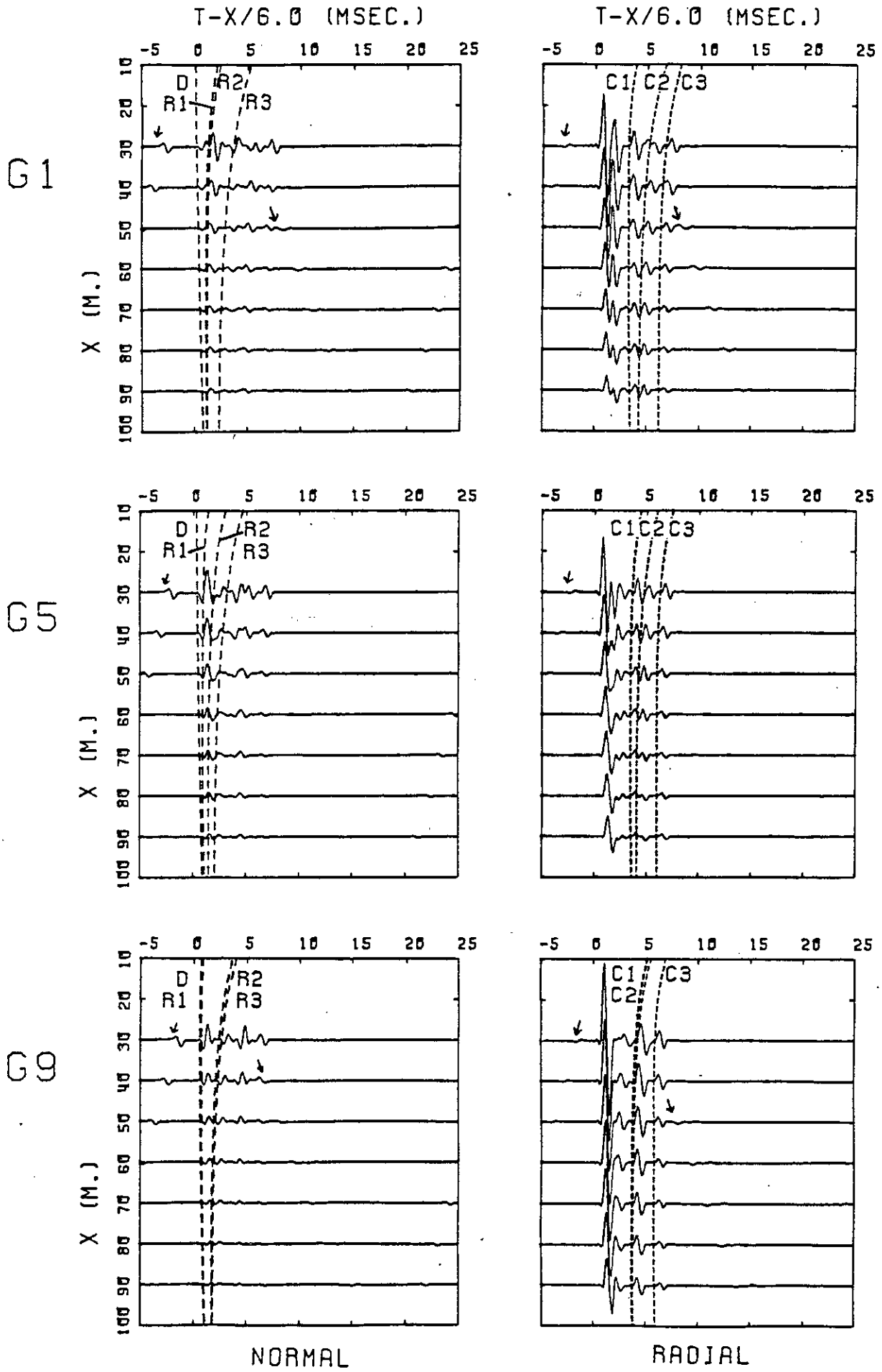
T-X/6.0 (MSEC.)
T-X/6.0 (MSEC.)
G1
G5
G9
X (M.)
D
R1
R2
R3
C1
C2
C3
NORMAL
RADIAL

truncated SV-wave response which is discussed in the next section, have both been integrated over 320 slowness values. The horizontal apparent velocities which correspond to the limits of the integration window have been set at 3.18 and 20 km/s in order to include the principal P and SV arrivals of interest.

The principal phases, which are identified schematically in Fig.6.5, consist of the direct and reflected P-waves, and converted waves of the type PSP, PPSP, PSSP, etc. These waves interfere constructively and destructively at the different receivers to produce the distinctly different P-wave codas shown in Fig.6.4. Small-amplitude numerical phases appear on these seismograms, and also on many of the other seismograms in this chapter. They are easily identified, since they propagate with phase velocities equal to the upper and lower velocity limits of the slowness integration window.

An examination of the particle motion of the first P-wave arrivals for different receiver positions has revealed two interesting features with implications for the field observations in the LASL HDR project. In Figs.6.6(a)-(d) we show polarization diagrams of the compressional wave arrivals at receiver positions G1, G3, G5, G7, and G9 at a distance of 40, 60, 80, and 160m from the source. Since the wave propagation is in a plane of sagittal symmetry in the anisotropic channel, there is no wave-motion in the transverse (x_2) direction, and we show the particle motion in the sagittal plane only. At each distance range, there is evidence of non-linear (elliptical) particle motion of the P-wave arrivals at one or more of the receiver positions.

At distance ranges greater than 40m, the non-linear motion of the first P-wave arrival is confined to receiver positions G5 and G7 at 60 and 80m, and positions G3 and G5 at 160m. The non-linear motion is due to the path difference between the direct wave and successive multiply-reflected

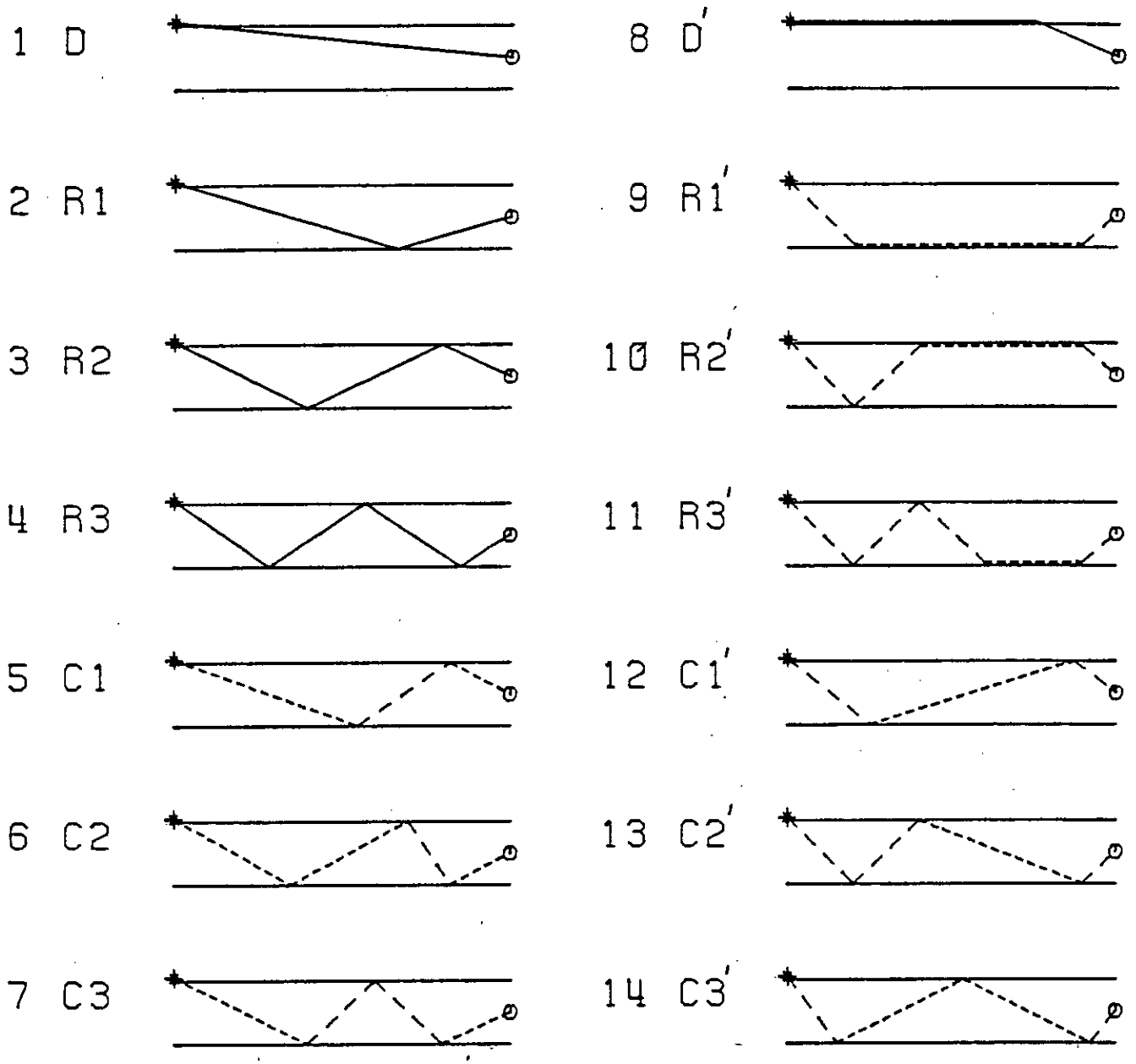

Figure 6.5 Schematic descriptions of the labelled arrivals in Fig.6.4 and Figs.6.7 and 6.8. Short dashes denote P-waves, long dashes denote SV-waves, and straight lines denote a phase of either type which is uniform over the wavepath.

Figure 6.6(a) Polarization diagrams of the first P-wave arrivals at five different receiver positions in model A of Table 6.3, at 40 km from the source. The particle motions in the sagittal plane are plotted for the three consecutive time windows indicated on each of the three-component records. The labels on the diagrams denote Up, Down, Towards, and Away from the source. The arrow in the first time-window indicates the direction of the receiver with respect to the source. Non-linear particle motion of the first P-wave arrival is evident at some of the receiver positions, and the direction of this particle motion at the receiver is not always in the direction of the source.

T-X/6.0 (MSEC.)

G1

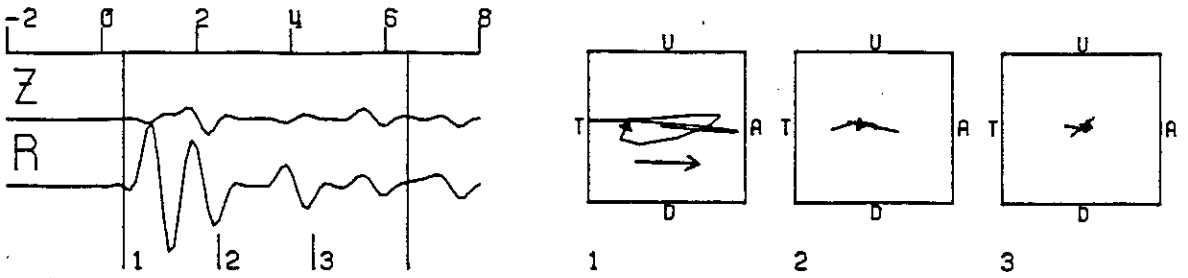

G3

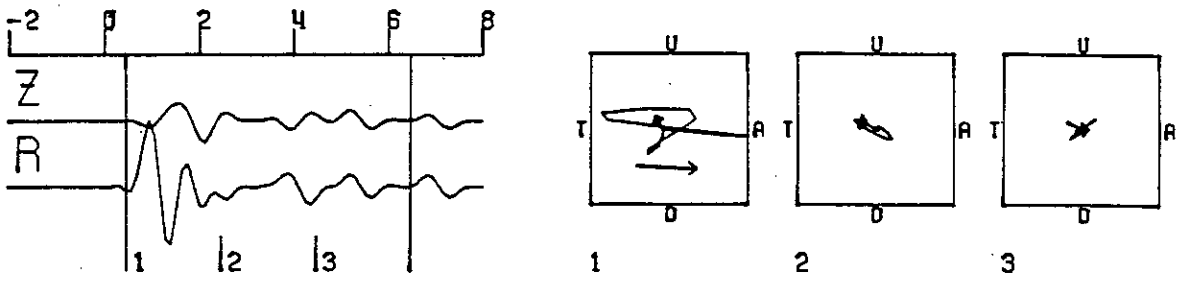

G5

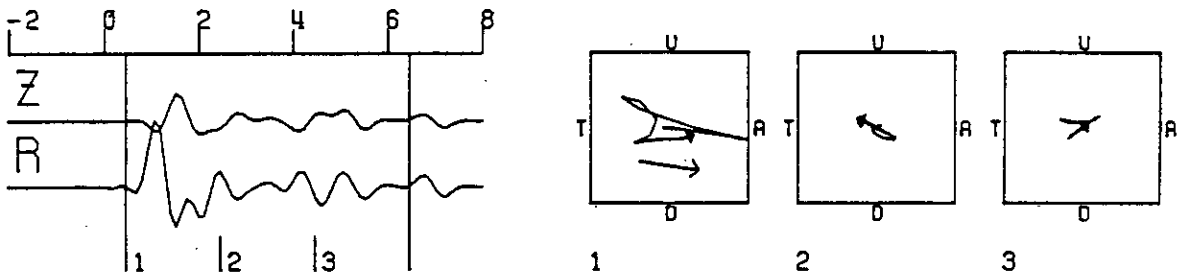

G7

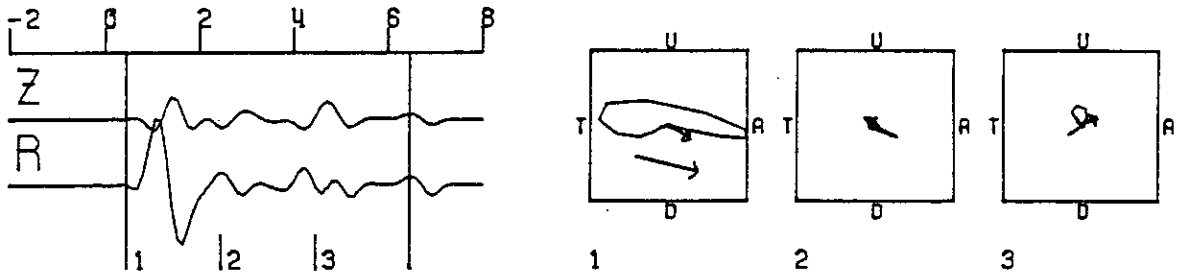

G9

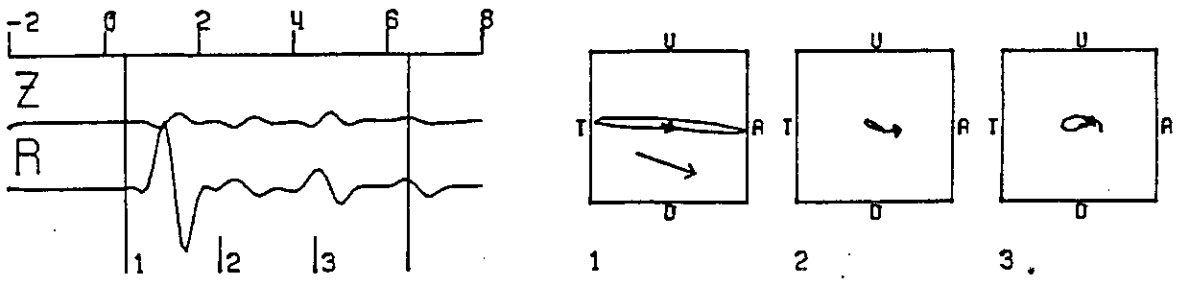

X = 40 M.

Figure 6.6(b) Polarization diagrams of the first P-wave arrivals at five different receiver positions in model A of Table 6.3, at 60 km from the source. The particle motions in the sagittal plane are plotted for the three consecutive time windows indicated on each of the three-component records. The labels on the diagrams denote Up, Down, Towards, and Away from the source. The arrow in the first time-window indicates the direction of the receiver with respect to the source. Non-linear particle motion of the first P-wave arrival is evident at some of the receiver positions, and the direction of this particle motion at the receiver is not always in the direction of the source.

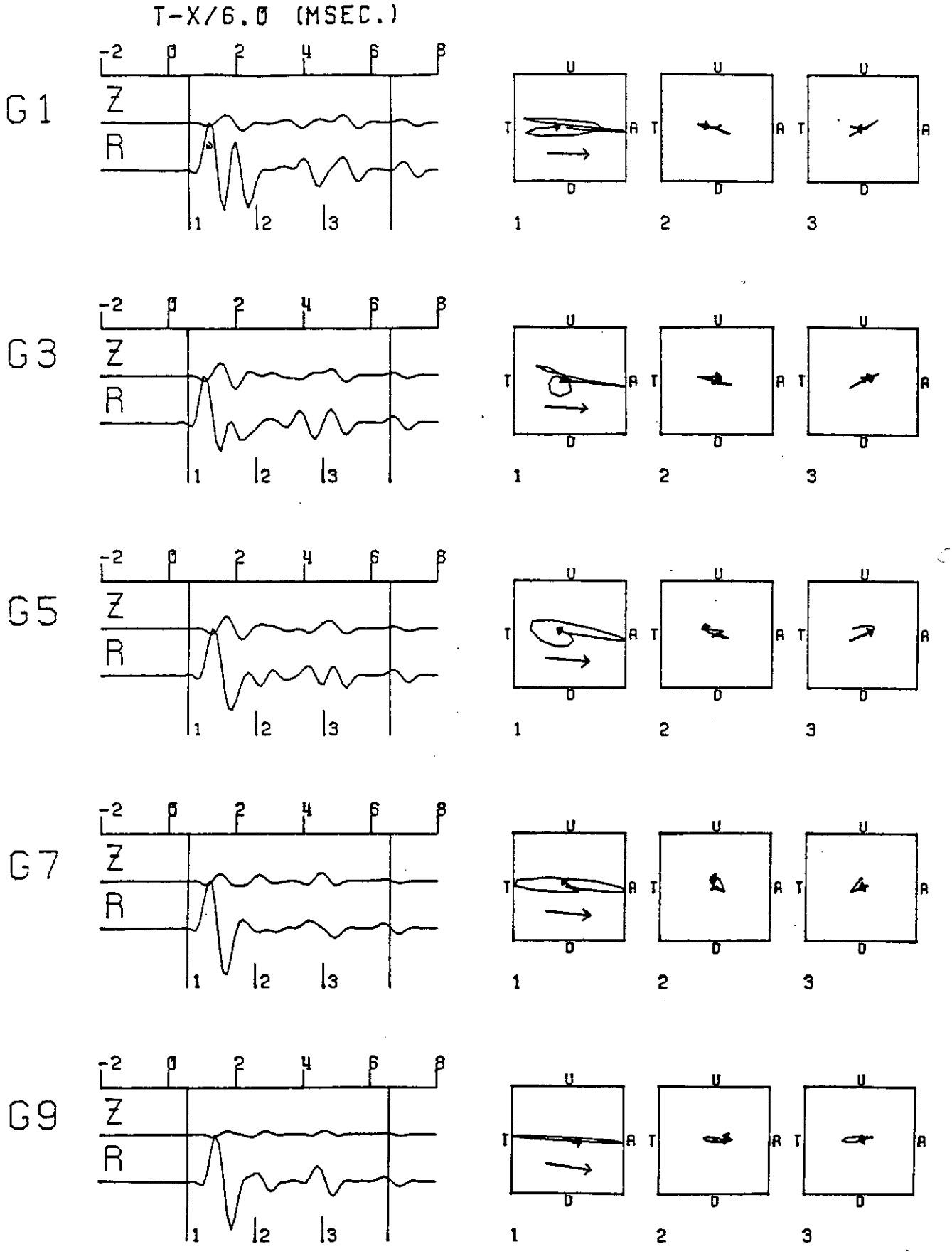

X = 60 M.

Figure 6.6(c) Polarization diagrams of the first P-wave arrivals at five different receiver positions in model A of Table 6.3, at 80 km from the source. The particle motions in the sagittal plane are plotted for the three consecutive time windows indicated on each of the three-component records. The labels on the diagrams denote Up, Down, Towards, and Away from the source. The arrow in the first time-window indicates the direction of the receiver with respect to the source. Non-linear particle motion of the first P-wave arrival is evident at some of the receiver positions, and the direction of this particle motion at the receiver is not always in the direction of the source.

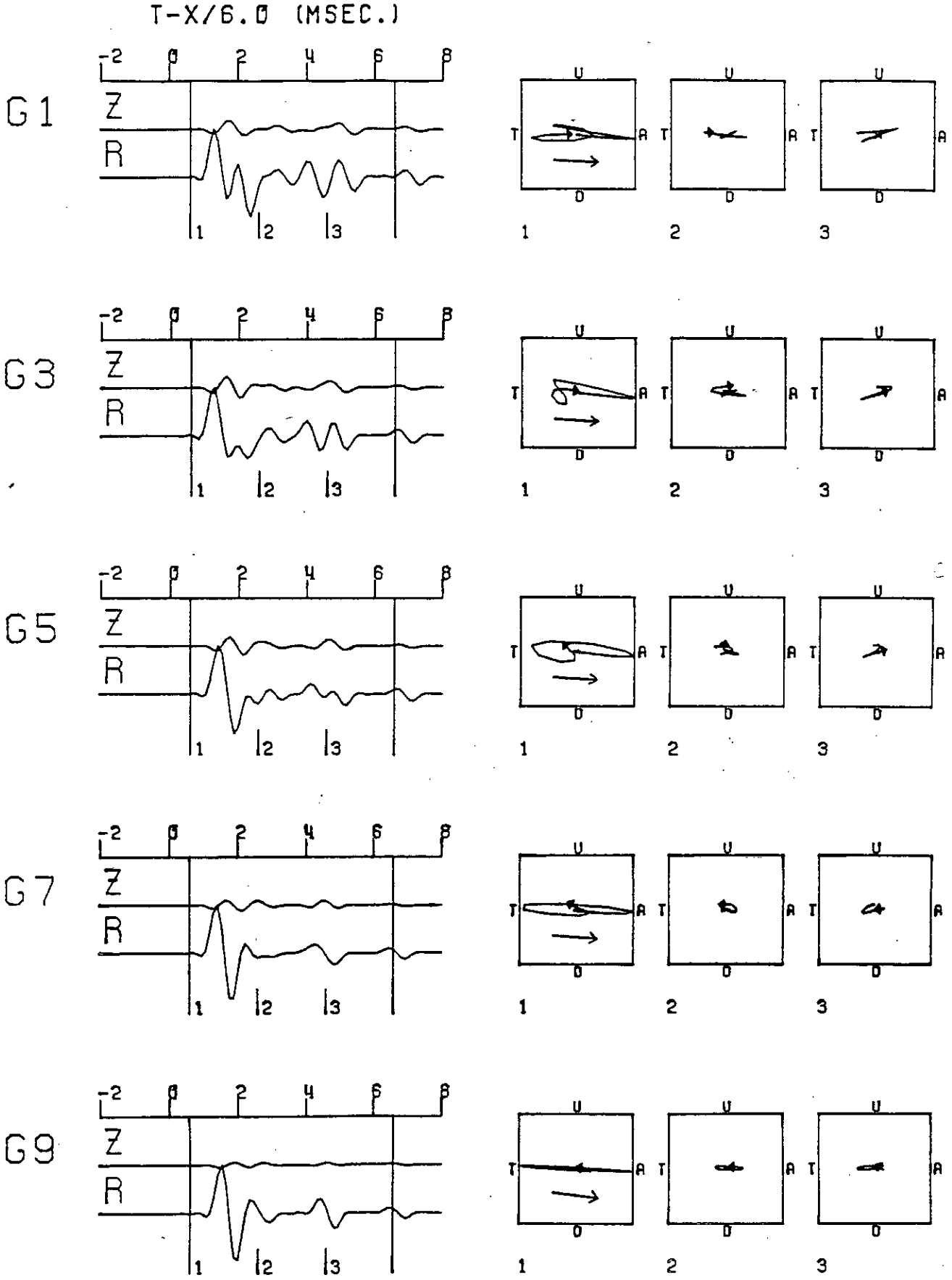

X = 80 M.

Figure 6.6(d) Polarization diagrams of the first P-wave arrivals at five different receiver positions in model A of Table 6.3, at 160 km from the source. The particle motions in the sagittal plane are plotted for the three consecutive time windows indicated on each of the three-component records. The labels on the diagrams denote Up, Down, Towards, and Away from the source. The arrow in the first time-window indicates the direction of the receiver with respect to the source. Non-linear particle motion of the first P-wave arrival is evident at some of the receiver positions, and the direction of this particle motion at the receiver is not always in the direction of the source.

T-X/6.0 (MSEC.)

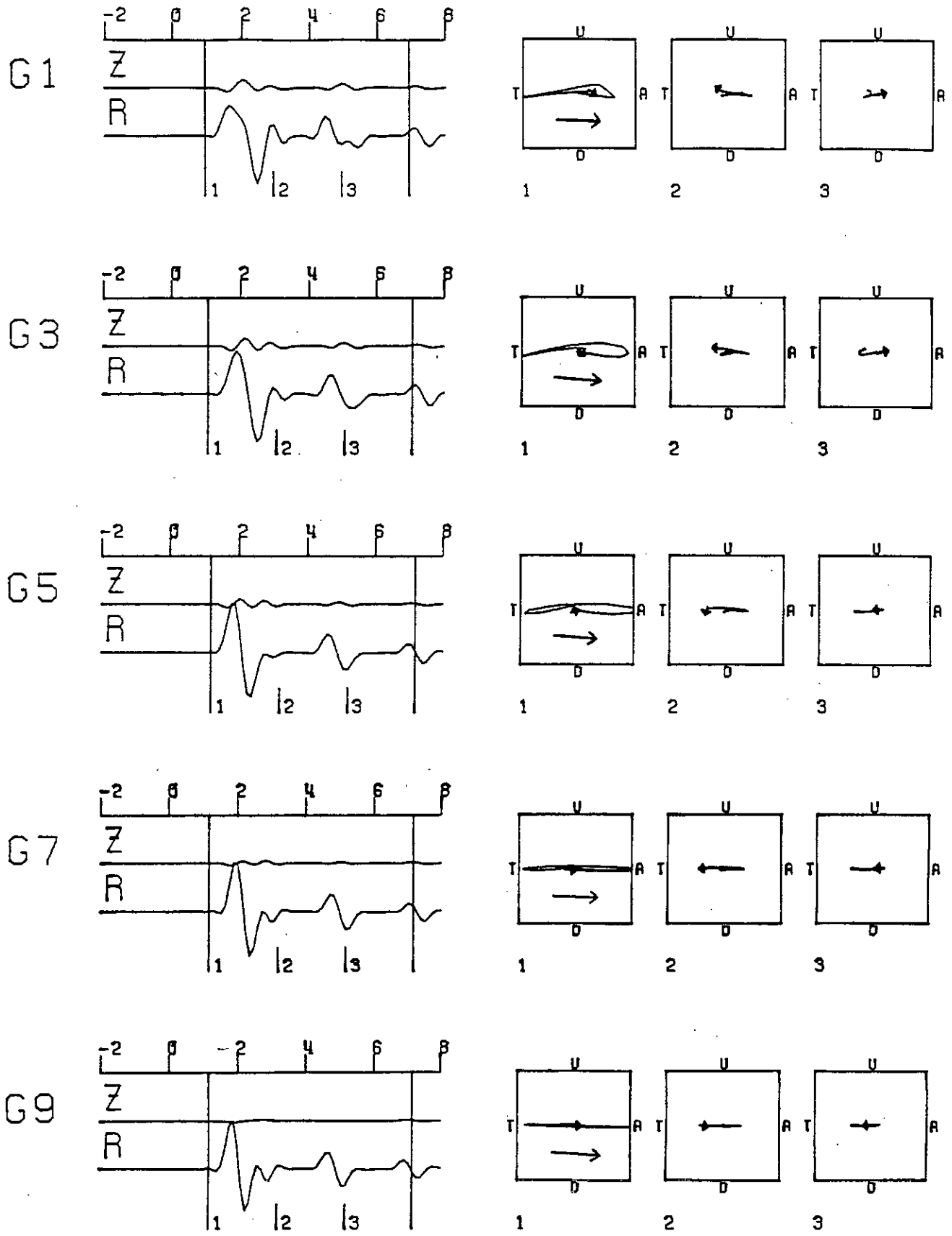

X = 160 M.

P-wave arrivals being a fraction of a wavelength of the source pulse.

Non-linear P-wave particle motion has been noted by Aamodt et al. (Brown et al. 1979) in the downwell recordings of microseismic events at Fenton Hill. They assume linear ground motion in a homogeneous isotropic medium, and they attribute the observed elliptical motion to coupling between the different components in the geophone package. However, the results obtained from the synthetic records indicate that the non-linear particle-motion could alternatively be explained in terms of the location of the receiver in the cracked structure and the wavelength of the source pulse.

The second feature which may be observed on the particle-motion plots is that the polarization of the first half-cycle of the P-wave motion does not reliably indicate the direction of the source. If the location of the source was based on the S-P time and the direction of the polarization of the first P-wave arrival, then the source would be located well outside the cracked channel, from the P-wave polarization directions at receiver positions G1, G3, and G5, at all distance ranges. Similarly, from the direction of the P-wave polarizations at G9, the source would be located inside the channel. For the polarization diagrams shown in Fig.6.6, the P-wave polarization direction appears to be consistent with the actual position of the source on the boundary of the cracked channel at receiver position G7 only.

Pearson (1981) uses S-P times and P-wave polarizations to locate microearthquakes at Fenton Hill which have been caused by hydraulic pressurization of the second, deeper major crack in Fig.6.1. He finds considerable scatter of the locations about the fracture planes, with many events occurring at some distance from the major fracture planes. The observations made above from the polarization diagrams suggest that some events could be re-located nearer the fracture undergoing pressurization.

We have noted in section 6.3 that the seismic source is more likely to be due to shear failure than an opening crack. Thus the P-wave radiation pattern is more likely to be that of a double-couple than a tension crack. However, the non-linear P-wave motion appears to be associated with the path-differences of wave arrivals which are not widely-separated on the focal sphere, and thus the amplitude radiation pattern of the source is not likely to influence this effect. Also, a change in the radiation pattern would not be expected to alter the direction of the particle-motion of an arrival, though it could reverse its polarity. Thus the mislocations of the source would not be changed by a change in the source type.

6.6 SV-wave arrivals: direct waves and first reverberations

In this section we investigate the characteristics of the first shear-wave arrivals in anisotropic and isotropic channels which are bounded by thin liquid layers (models A and B in table 6.3) and in an anisotropic low-velocity channel with no liquid layers (model C). The response in the channel has been truncated to the direct wave plus first multiples and phase conversions in order to avoid time-aliasing effects, as explained in section 6.4 above.

Sections of vertical and horizontal component truncated shear-wave seismograms for the receiver position G1 are shown in Fig.6.7 for the models A, B, and C. The differences between the models are small, but they produce significant changes in the seismograms. Schematic descriptions of the wave arrivals are given in Fig.6.5.

First we consider the seismograms for model A, where an anisotropic channel is separated from two surrounding isotropic halfspaces by thin liquid-filled cracks. The principal arrivals are the direct wave D from the source, the multiple reflections R1, R2, and R3, the converted waves

Figure 6.7 Normal and radial component seismograms of SV-waves from a tension crack source, for receiver position G1 in models A, B, and C of Table 6.3. The response in the channel has been truncated to that of the direct waves and the first multiple reflections. Refracted waves are identified on the normal component seismograms: direct, reflected, and converted waves are identified on the radial component seismograms. Converted waves are denoted by a short dash, and all labelled arrivals are identified schematically in Fig.6.5.

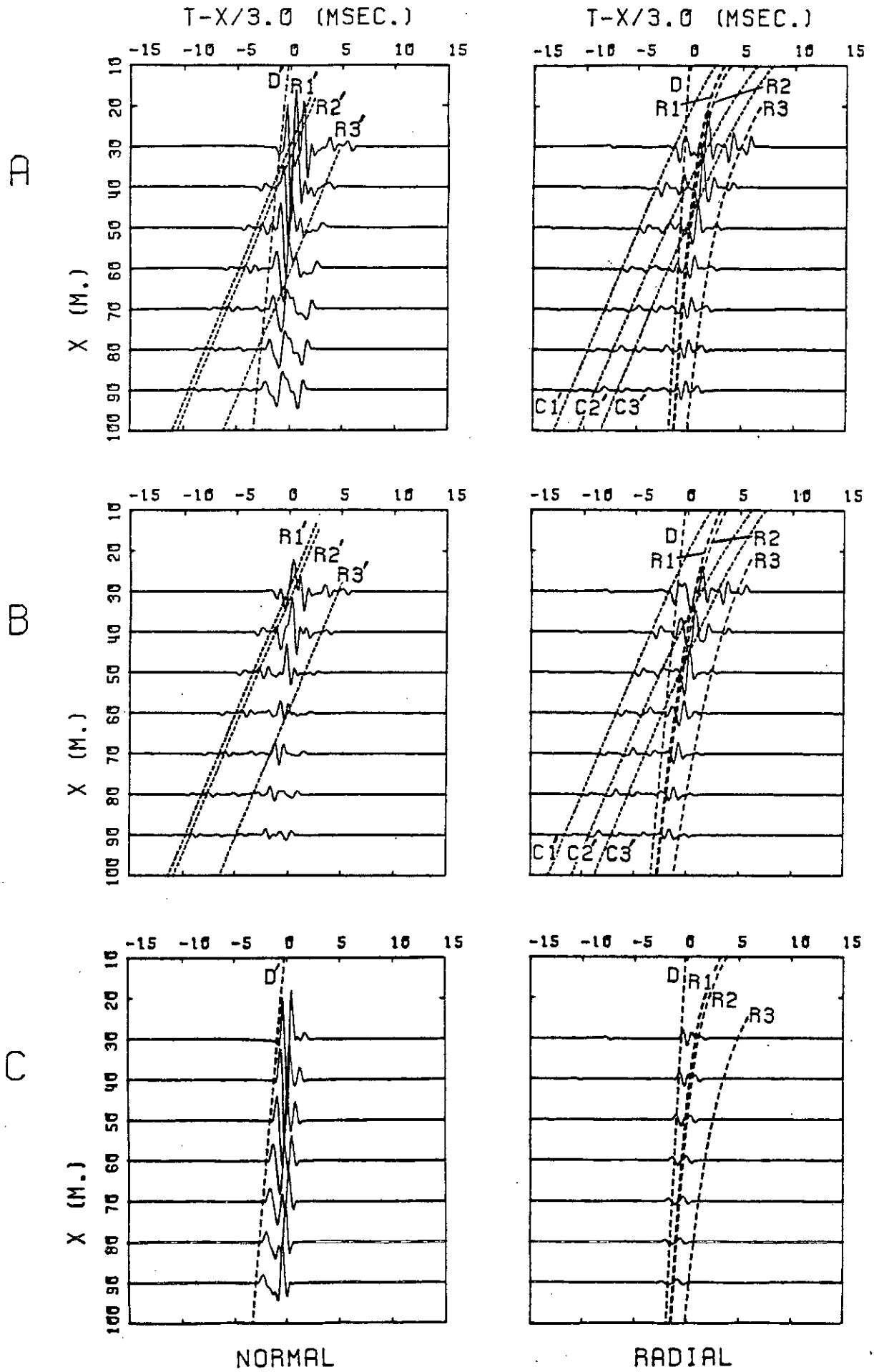
T-X/3.0 (MSEC.)
T-X/3.0 (MSEC.)
-15 -10 -5 0 5 10 15
X (M.)
10 20 30 40 50 60 70 80 90 100
A
B
C
D
R1
R2
R3
C1
C2
C3
NORMAL
RADIAL

C1', C2', and C3', and the refracted waves D', R1', R2' and R3'.

The refracted wave arrivals require some explanation. The refracted wave D' does not pass through the water layer. It results from the assumption that the isotropic layer and the anisotropic layer are in direct contact in the region of the source. The transmission of energy from the isotropic halfspace into the anisotropic layer is regulated at all distances by the transmission coefficients between these two media, while subsequent reflections of the transmitted wave energy in the channel are regulated by the reflection response at the interface with the liquid layer. Thus the above assumption results in wave energy leaking directly into the channel from the head wave which propagates in the halfspace. Although the arrival D' is thus due to the direct contact between channel and halfspace which is assumed for transmission of energy into the channel, it is not necessarily a spurious phase in the cracked channel. The faces of cracks C1 and C2 will be irregular, and there may well be many points of contact between the crack faces, through which shear-wave energy could propagate into the channel.

The refracted waves R1', R2', and R3' are interesting. They are shear-waves which travel as refracted P-waves in the anisotropic channel for most of their path. Ewing, Jardetsky & Press (1957), p.58, and Červený & Ravindra (1971),p.124, have discussed this unusual type of head-wave, which has also been observed on synthetic seismograms by Kind & Müller (1975). The amplitude of this head-wave is much larger for the cracked channel model than for Kind & Müller's crust and mantle model, due to the particular boundary conditions at the channel/liquid-layer interface.

For model B, where the channel between the liquid layers is isotropic and formed of the same material as the enclosing halfspaces, similar phases propagate. However there is no refracted wave of the type D', since the materials forming the channel and the enclosing halfspaces are the same.

It is seen that there are significant differences between the seismograms at receiver position G1 in cracked and uncracked channels, particularly on the vertical component, where the amplitude of the shallow SV-wave reflections is largest. The difference in amplitude between the two models is likely to be due to the differences in velocity contrast between the channel and the surrounding solid halfspaces. This velocity contrast is significant, despite the presence of the liquid layer, because the 1mm thickness of the liquid layer is a very small fraction of the 3.5m wavelength of the SV-waves in the channel. The reflection response at the boundaries of the channel would thus be expected to be dependent on the properties of the solid halfspace as well as the liquid layer.

The seismograms which have been calculated for model C appear to be the simplest. There are no liquid layers in this model to form a waveguide for the SV-waves, nor is the velocity-contrast at the boundaries of the anisotropic channel sufficient to form a good waveguide. Thus the amplitude of the successive shear-wave reverberations decreases very rapidly and the amplitude of the three times reflected wave R3 is almost zero. Thus large-amplitude channel-waves produced by multiply-reflected shear-waves are not expected for this model, which illustrates the importance of the liquid layer in creating a shear-wave channel in homogeneous rock.

In Fig.6.8 we show the effect on the truncated SV-wave response of varying the receiver position within the cracked channel of model A. Synthetic seismograms are shown for the normal and radial components at receiver positions G1, G5, and G9, for a distance range which is comparable with that of the events observed by LASL. Over this distance range, which is longer than that which was used for the seismograms in Fig.6.7, the direct and reflected SV-wave arrivals travel at shallow angles of incidence and thus possess greater wave-energy in the normal component than in the

Figure 6.8 Normal and radial component seismograms of SV-waves from a tension crack source, for receiver positions G1, G5, and G9 in model A. The response in the channel has been truncated to that of the direct waves and the first multiple reflections. The travel-time curves on the normal component seismograms correspond to, from left to right, the direct and reflected SV-waves D, R1, R2, and R3 in Fig.6.5.

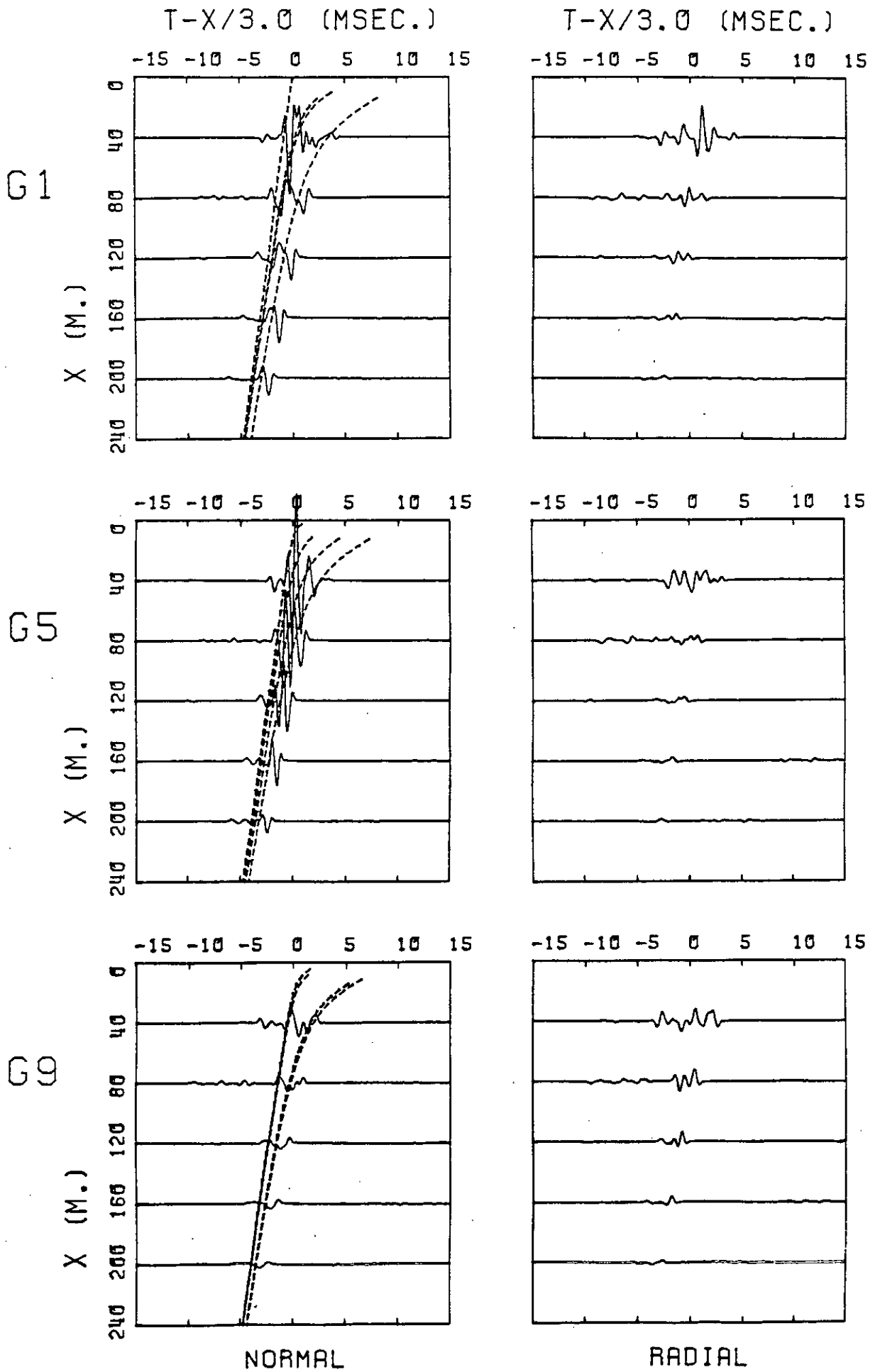
T-X/3.0 (MSEC.)
T-X/3.0 (MSEC.)
-15 -10 -5 0 5 10 15
G1
G5
G9
X (M.)
0
40
80
120
160
200
240
NORMAL
RADIAL

radial component. The small-amplitude fast arrivals which are visible at distances 40-120m before the principal arrivals are the converted and refracted arrivals C1', C2', C3', and R1', R2', R3' respectively, which we have discussed above with respect to Figs.6.4 and 6.7. Since their horizontal apparent velocities are greater than those of the direct and reflected SV-waves, they possess relatively greater wave-energy in the radial component.

The seismic coda of the principal arrivals is seen to differ greatly between different receiver positions. This coda is formed of the direct and reflected SV-wave pulses which arrive at the receiver with time-delays which are proportional to the differences in their path-lengths. These time-delays will differ according to the position of the receiver, as seen from the travel-time curves shown in Fig.6.8, and the wave pulses may interfere constructively or destructively, with allowance for a phase-change of 180^{o} after each reflection from the water-filled crack.

6.7 SV-wave arrivals: the complete response

The response of the reverberating wavetrains in the channel was truncated in the previous section so that small-amplitude first-arrivals could be investigated. We shall now consider shear-wave seismograms which have been computed with the complete plane-wave response of the model structure.

As far as the author is aware, synthetic seismograms for the type of structure shown in Fig.6.3(c) have not been computed before. Unusual wave arrivals such as channel-waves and Stoneley waves might be expected, due to the presence of the liquid layers. Therefore the integration of the complete plane-wave response was performed over a wide range of slownesses, with closely-spaced increments, in order to include a wide range of possible arrivals.

The horizontal apparent velocities which correspond to the limits of the slowness integration were set at 20 km/s and 2.7 km/s. This range of integration has been divided into two sections, and 700 slowness increments have been used to span the integration window for each section. One section covers the range of velocities between 2.7 and 3.5 km/s, and the other section covers the range 3.5 to 20 km/s. Thus the sampling of the displacement response and the oscillatory Bessel function is more closely-spaced at higher slownesses. Kennett (1980) found this to be desirable, when splitting a large integration window into smaller sections. The seismograms are calculated separately for each integration window and then they are summed to produce composite seismograms for the whole integration window. The numerical arrivals which are associated with the break in the overall integration window and appear on the separate seismograms, cancel each other out on summation of the seismograms.

We have calculated seismograms of SV-waves from the SV-wave part of a tension crack source, using the complete response of the cracked channel model A. In Fig.6.9 we present record sections of the normal and radial component seismograms for three different receiver positions in the cracked channel. These may be compared with the equivalent seismograms which were computed with the truncated response, in Fig.6.8.

As in Fig.6.8, most of the SV-wave energy appears on the normal component seismograms since the propagation vectors of the principal multiply-reflected SV-waves are very close to the radial direction in the sagittal plane. However, later SV-wave reverberations are seen to have more energy in the radial component as the angle of reflection at the channel boundaries decreases. This is particularly noticeable in the radial component seismograms for receiver position G5, where the multiply-reflected SV-waves appear to interfere constructively at 40-120 m.

There is a marked difference between the seismograms for the receiver

Figure 6.9 Normal and radial component seismograms of SV-waves from a tension crack source, for receiver positions G1, G5, and G9 in model A. The complete SV-wave response in the structure has been used in the construction of these seismograms.

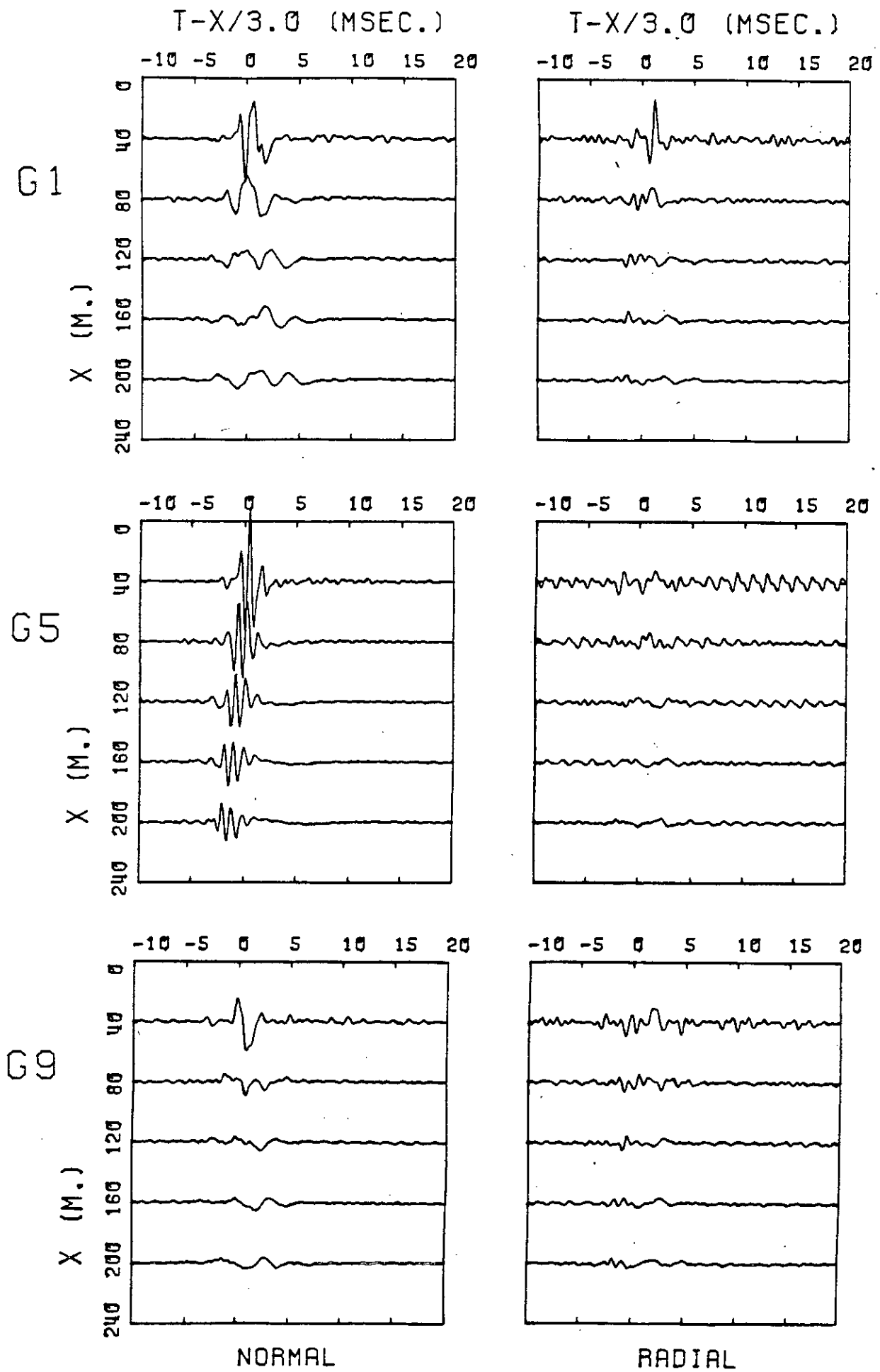
T-X/3.0 (MSEC.)
T-X/3.0 (MSEC.)
-10 -5 0 5 10 15 20
G1
G5
G9
X (M.)
0
40
80
120
160
200
240
NORMAL
RADIAL

position in the centre of the channel, G5, and those for receiver positions near the channel boundaries, G1 and G9. This difference, which was remarked on in the discussion of the truncated seismograms in Fig.6.8, is now more distinct when we consider the complete response. A low-frequency arrival with a period of 2.5 msec is visible on the seismograms for the receiver positions near the channel boundaries. This arrival is absent on the normal component seismograms for the central receiver position G5, but it is perceptible on the radial component seismograms at all receiver positions shown.

This arrival also appears to be dependent on the presence of the liquid layers. In Fig.6.10 we show record sections of seismograms corresponding to the complete SV-wave response at receiver position G1 for the models A, B, and C in Table 6.3. A low-frequency arrival is present in the seismograms for model B, which corresponds to an isotropic channel bounded by thin liquid layers. However, no such arrival is present in the seismograms for model C, which does not incorporate any liquid layers. The absence of any reverberations in the coda of the seismograms for model C shows how quickly the SV-wave energy propagates out of the channel in the absence of a strong velocity-contrast, or a fluid-solid interface. Comparison of the seismograms for models A and B shows that cracking of the channel results in a significant difference in the form of the SV-wave coda.

The phase velocity of the low-frequency arrival is 3.12 ± 0.01 km/s in the case of model A. This is lower than the lowest value of the SV-wave velocity in the cracked channel, and it is possible that the arrival could represent a Stoneley wave propagating along the interface with the liquid layer. However, the theoretical exponential decay of wave amplitude with receiver depth for the observed phase velocity and frequency is not large enough to support this hypothesis.

Figure 6.10 Normal and radial component seismograms of SV-waves from a tension crack source, for receiver position G1 in models A, B, and C of Table 6.3. The complete SV-wave response in the structure has been used in the construction of these seismograms.

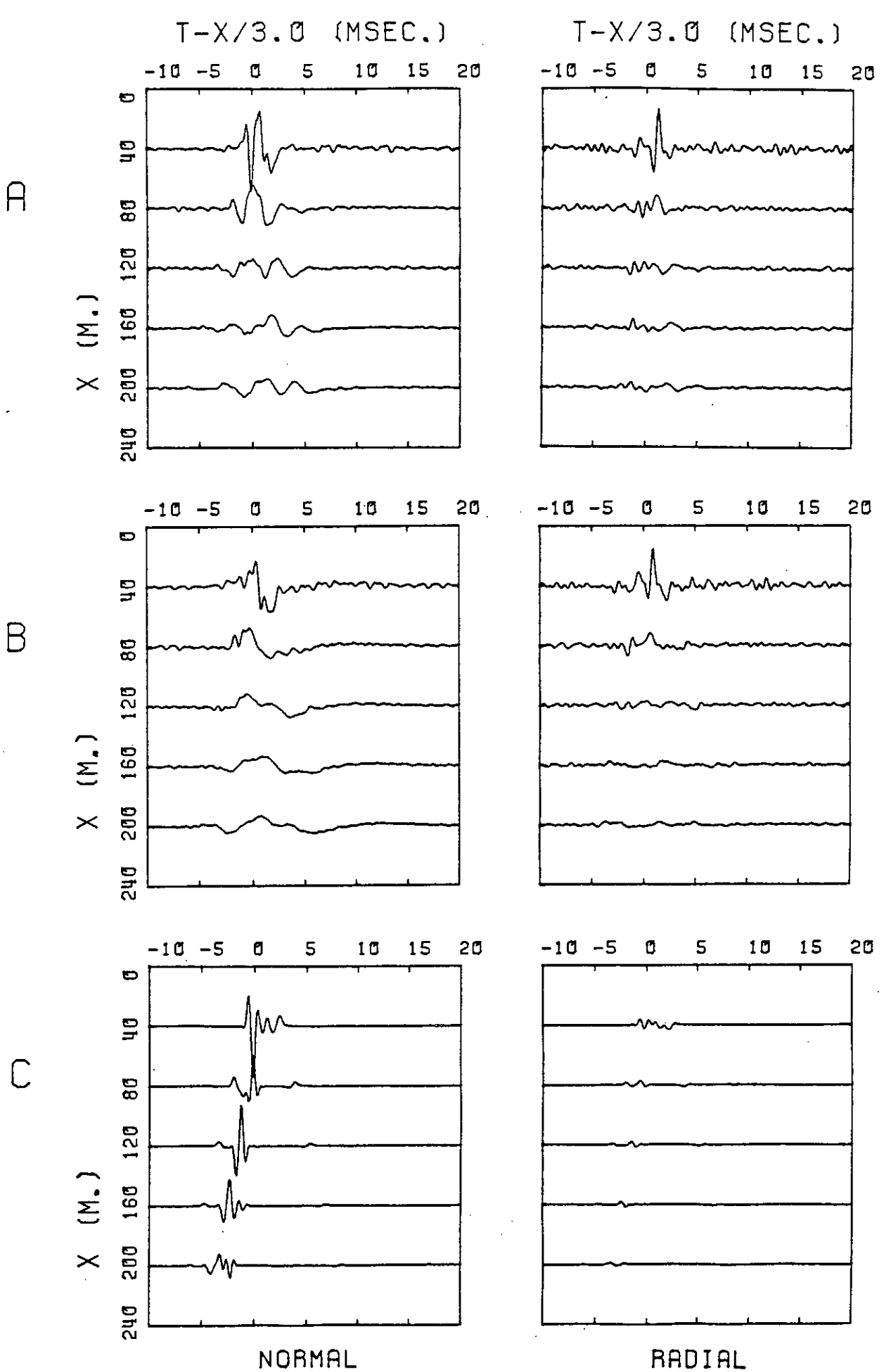
T-X/3.0 (MSEC.)
T-X/3.0 (MSEC.)
-10 -5 0 5 10 15 20
A
B
C
X (M.)
0
40
80
120
160
200
240
NORMAL
RADIAL

It may be observed from Fig.6.9 that the normal component of the low-frequency arrival takes opposite phases on either side of the centre of the channel, and its amplitude is zero in the centre. The phase of the radial component of the arrival is the same at all depths in the channel. These observations suggest that the arrival is a symmetrical mode of a Rayleigh-type channel-wave. A theoretical treatment of such waves has been given by Tolstoy & Usdin (1953). They show that channel-waves in a waveguide can propagate with a phase velocity less than the shear-wave velocity in the channel.

The presence of this type of low-frequency channel-wave also appears to be dependent on the P-wave reverberations in the thin liquid layer, in Fig.6.11 we show SV-wave seismograms for receiver position G1 in model A. These seismograms have been computed using the complete response in the cracked channel, but the response in the liquid layer has been truncated to the direct wave plus first reverberations. They may be compared with the corresponding seismograms for this model and receiver position which were computed by using the complete response in all the layers, in Figs.6.9 or 6.10. The absence of channel-waves in Fig.6.11 shows that the presence of Rayleigh-type channel-waves in this structure is crucially dependent on the constructive interference of multiply-reflected P-waves in the liquid layers.

We have stated in section 6.3 that the events observed at Fenton Hill are more likely to be caused by shear failure on planes of weakness surrounding the hydraulic fracture, rather than tensile failure at the fracture's expanding edge. Accordingly, we use a vertical double-couple source to simulate shear failure on a thermal contraction crack, orthogonal to the major crack. The SV-wave radiation pattern of this source has been illustrated in Fig.2.3. SV-wave record sections which have been constructed using this source for receiver position G1 in model A are

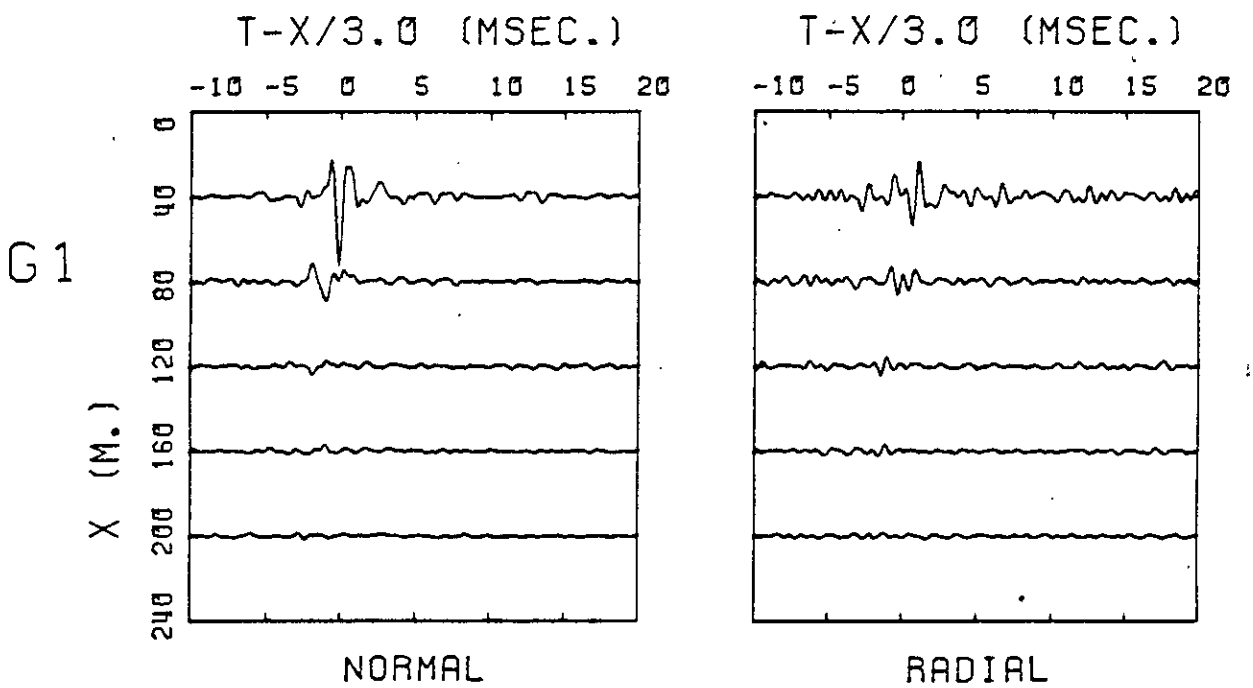

Figure 6.11 Normal and radial component seismograms of SV-waves from a tension crack source, for receiver position G1 in model A. The response has been truncated in the liquid layers to that of the direct and first multiple P-wave reflections.

illustrated in Fig.6.12. On comparing them with corresponding record sections in Figs.6.9 or 6.10, it is seen that the form of the channel wave does not depend on the source type, although there is an increase in the overall amplitude of the wave arrivals.

The Rayleigh-type channel-wave which has been described above, though interesting, cannot account for the low-frequency, extended wavetrain which is observed on the vertical component of the observed seismograms in Fig.6.2. From the record sections in Figs.6.9 and 6.10 for the theoretical models, it is seen that the period of the Rayleigh-type channel-wave is half that of the observed wavetrain, and it extends for little more than one cycle. The most important point is that the particle-motion of the Rayleigh-type channel-wave is principally in a plane orthogonal to that of the major-cracks, whereas the particle-motion of the observed low-frequency wavetrain is parallel to the major-crack plane. Therefore if the low-frequency wavetrain observed on the vertical components of the observed seismograms is a channel-wave phenomenon, the channel-waves forming the wavetrain must be Love-type channel-waves, with particle-motion in the transverse direction. In the next section we investigate the propagation of SH-waves in the channel.

6.8 SH-wave arrivals

SH-waves are the most likely waves to generate a long reverberating wavetrain in a channel which is bounded by liquid cracks. The SH-waves which propagate in such a channel lose wave energy only by geometrical spreading and anelastic attenuation. There is no leakage of SH-wave energy into the liquid layers by conversion to compressional wave energy at the interface, as in the case of SV-waves.

The source mechanism which we have used to generate SH-waves has

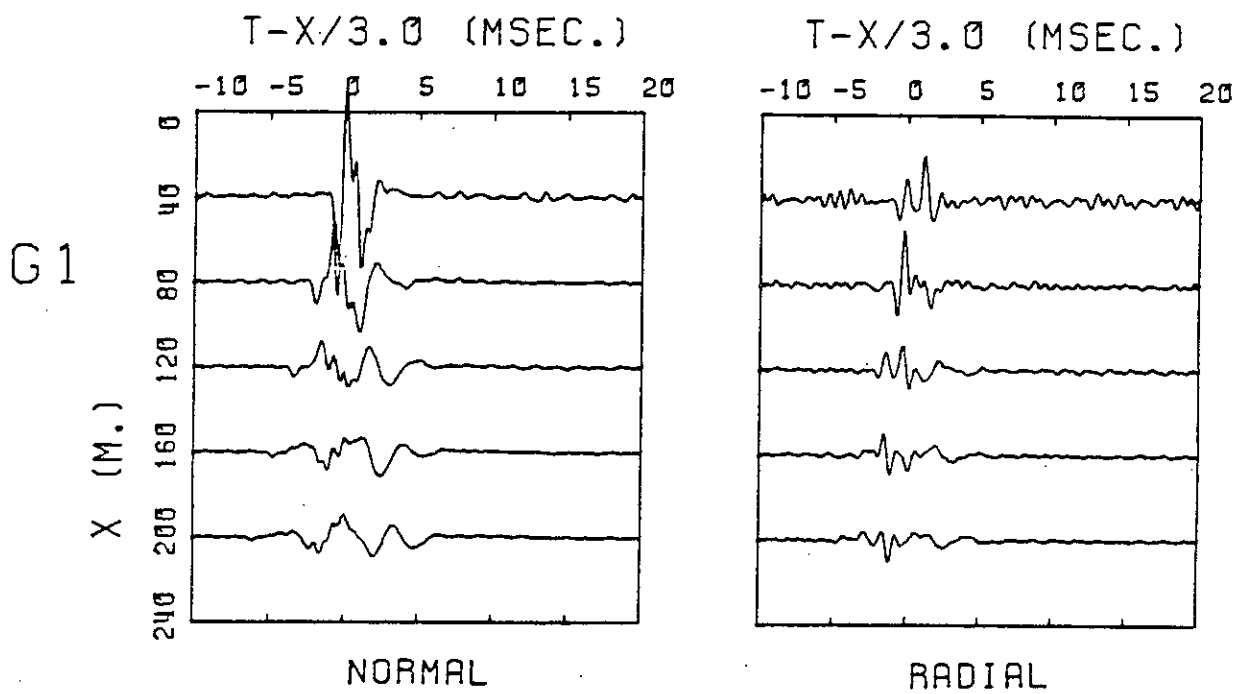

Figure 6.12 Normal and radial component seismograms of SV-waves from a vertical double-couple source, for receiver position G1 in model A. These seismograms have been plotted on an amplitude scale which is four times smaller than that which has been used for previous seismograms in this chapter.

already been described in section 6.3. It may be represented by a horizontal single-couple in the plane $x_3=0$, with force vectors parallel to the x_2 axis. The complete plane wave response in the structure has been used in the computation of the SH-wave seismograms. As in the case of the corresponding SV-wave seismograms, the range of integration over slowness has been divided into two sections, and 700 slowness increments have been used to span each section. The limits of the integration window correspond to horizontal apparent velocities of 2.7 and 20 km/s.

Initially we set the dominant frequency of the source pulse to 900 Hz, the same frequency which was used in the investigation of P- and SV-wave propagation in the channel. Synthetic seismograms of the reverberating SH-waves in the channel of model A are illustrated in Fig.6.13 for receiver positions G1 and G5. The reverberations suffer very little attenuation, and time-aliased arrivals are present before the true first arrivals. The formation of the coda of the seismograms is clearly apparent as a train of SH-wave reverberations with steadily increasing time delays between the successive reflections.

It is obvious that the theoretical seismograms in Fig.6.13 do not replicate either the frequency or the coherency of the low frequency shear-wave coda on the vertical component of the experimentally-observed seismograms in Fig.6.2. In order to generate more wave energy with the same frequency as the observed low-frequency wavetrain, we reduce the frequency of the source pulse. Seismograms of SH-waves at receiver position G1 in models A,B, and C of Table 6.3 have been calculated for a lower source frequency of 200 Hz, which is the same as that of the low-frequency wavetrain. These seismograms are shown in Fig.6.14.

The SH-wave coda has an asymmetrical appearance in the seismograms corresponding to models A and B. This is principally due to the interference effects between the successive reverberating wavelets.

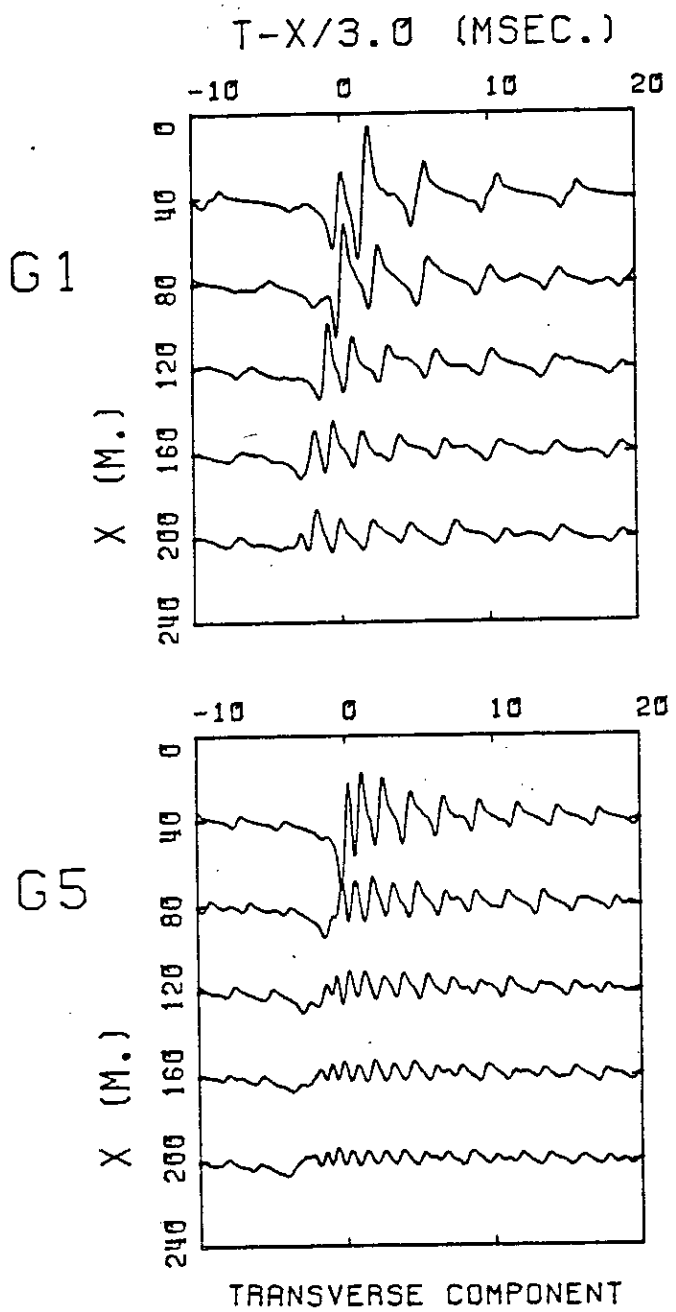

Figure 6.13 Transverse component seismograms of the complete SH-wave response at receiver positions G1 and G5 in model A, using a horizontal single-couple source.

Figure 6.14 Transverse component seismograms of the complete SH-wave response at receiver position G1 in models A, B, and C of Table 6.3, using a horizontal single-couple source. The labelled arrivals are the direct wave D and the refracted wave D', which are described schematically in Fig.6.5. The arrowed arrival on the section corresponding to model C is a numerical arrival associated with the upper limit of the integration window. The dominant frequency of the source pulse which has been used in the computation of the SH-wave seismograms in Figs.6.14-6.16 is 200 Hz.

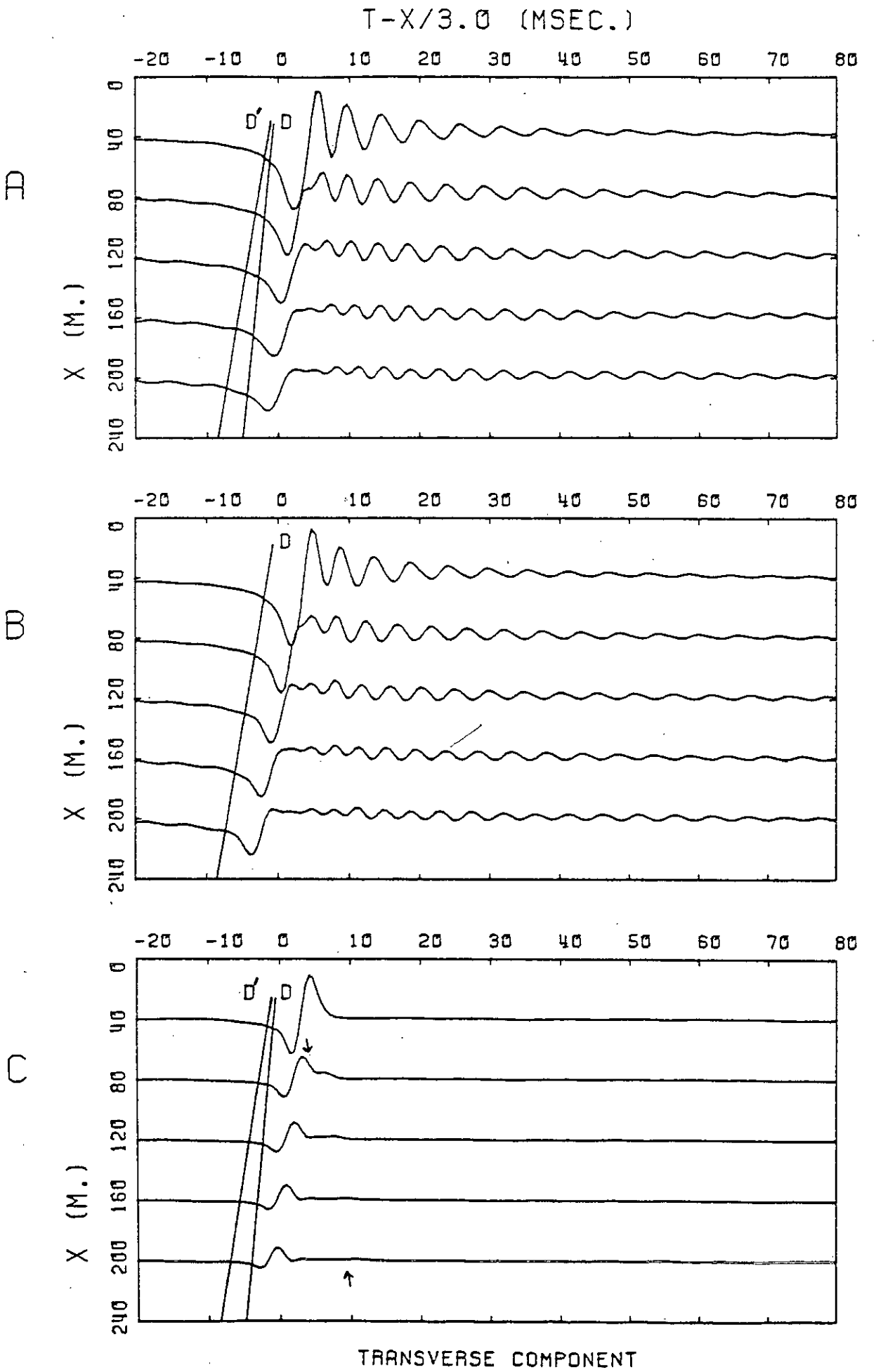
T-X/3.0 (MSEC.)
-20 -10 0 10 20 30 40 50 60 70 80
A
B
C
D'
D
X (M.)
0 40 80 120 160 200 240
TRANSVERSE COMPONENT

However, there also appears to be a long-period acausal arrival of wave-energy before the direct wave D and the refracted arrival D'. This appears to be related to the presence of the fluid layers in these models , since it is very much smaller in the seismograms for model C, where the fluid layers are absent. It is likely that it is a numerical effect, which may be caused by insufficient accuracy of integration over a response which is sharply peaked due to the large velocity contrast at the fluid/solid interfaces.

We state again that the type of anisotropy in the cracked channel models does not give rise to any anomalous wave motion. The cracked channel in model A is effectively isotropic for SH-wave propagation, with an SH-wave velocity of 3.189 km/s, as seen from the velocity-variation graph in Fig.6.3(b). The SH-wave velocity in the uncracked channel of model B is 3.349 km/s. In both models the SH-waves are totally internally reflected within the channel, and the velocity contrast between the channel and the surrounding solid halfspaces does not influence the form of the SH-waves as it did in the case of the SV-waves. As might be expected, the form of the seismograms is the same for the two models, although there are slight differences in the arrival times of the direct and reflected SH-waves.

The importance of the liquid layer in confining shear-wave energy to the channel is demonstrated again by comparing the seismograms for models A and B with those for model C. In the seismograms corresponding to model C, the direct wave from source to receiver is the only significant arrival. (A small numerical arrival associated with the upper limit of integration over slowness is also identified.) The wave-energy contained within the channel by reflection at the boundaries is virtually nil, and almost all the wave-energy is transmitted directly out of the channel.

Seismograms of low-frequency SH-waves at receiver positions G1, G5,

and G9 in model A are shown in Fig.6.15. The wavetrains of the seismograms for receiver positions G1 and G9 are almost identical, though 180° out of phase with each other, while at receiver position G5, the reverberations interfere destructively. The dominant frequency of the theoretical SH-wave coda is approximately the same as that of the observed shear-wave coda, but there is dispersion in the theoretical coda which does not appear to be present in the observed coda. The asymmetrical form of the early part of the seismograms also indicates that these theoretical models do not adequately represent the experimental situation.

Several important parameters which are used to describe the simple theoretical models A, B, and C are poorly determined experimentally. The thickness of the channel between the two major cracks is one example, and in Fig.6.16 we show transverse component seismograms for three different receiver positions in model D of Table 6.3. Model D is similar to model A, but the thickness of the cracked channel has been increased from 10 to 20 metres.

The effect of increasing the thickness of the channel is to alter the reverberating wavetrain by increasing the time interval between successive reverberations. This is seen most clearly by comparing the seismograms at receiver position G1 for models A and D in Figs.6.15 and 6.16 respectively. The spacing between successive reflections in the centre of the channel, at receiver position G10, does not now give rise to the destructive interference encountered at the corresponding position in model A. Also, the asymmetry of the early part of the wavetrain is very much reduced, as seen in the seismograms for receiver positions G1 and G5. However, dispersion is still apparent in the wavetrains of the theoretical seismograms.

The variation in character of the SH wavetrain with receiver position which is observed above is not found in the seismograms of Love-type

Figure 6.15 Transverse component seismograms of the complete SH-wave response at receiver positions G1, G5, and G9 in model A, using a horizontal single-couple source.

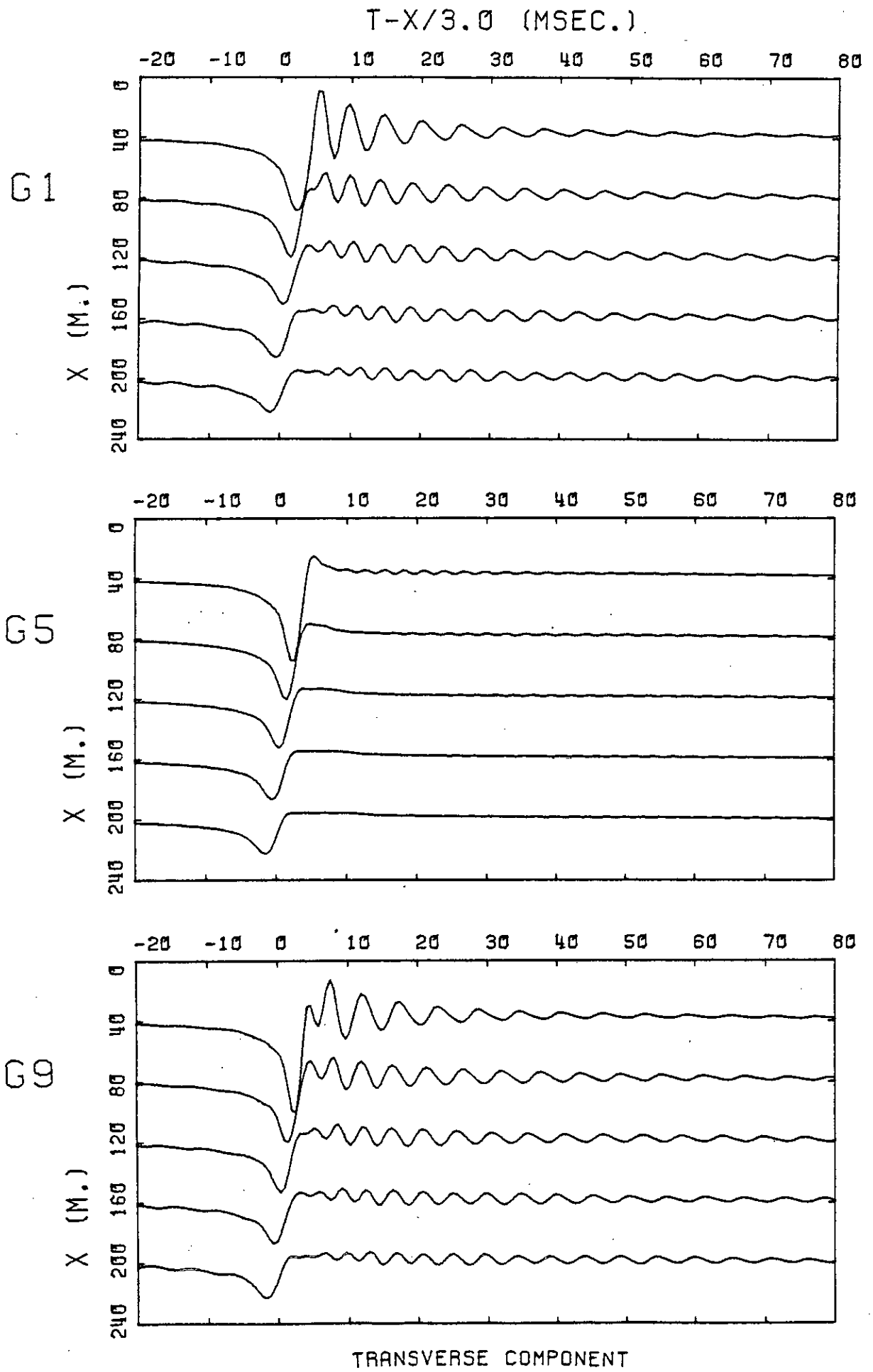
T-X/3.0 (MSEC.)
-20 -10 0 10 20 30 40 50 60 70 80
G1
G5
G9
X (M.)
0 40 80 120 160 200 240
TRANSVERSE COMPONENT

Figure 6.16 Transverse component seismograms of the complete SH-wave response at receiver positions G1, G5, and G10 in the 20m thick cracked channel of model D in Table 6.3, using a horizontal single-couple source.

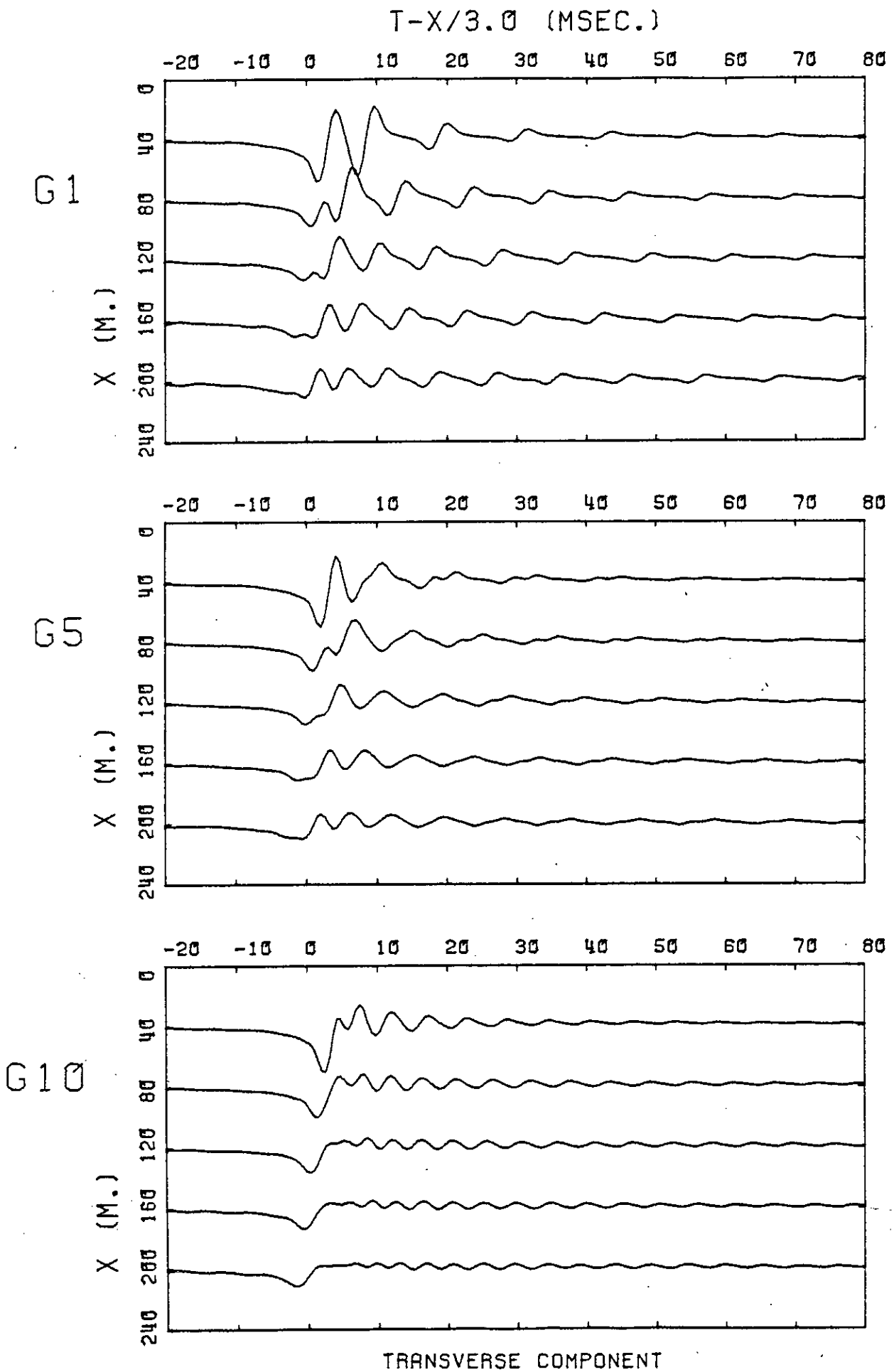
T-X/3.0 (MSEC.)
-20 -10 0 10 20 30 40 50 60 70 80
G1
G5
G10
X (M.)
0 40 80 120 160 200 240
TRANSVERSE COMPONENT

channel-waves which have been observed in coal-seams (Krey 1963). Krey located the seismic source in the middle of the seam and observed a highly coherent wavetrain of symmetric-mode, Love-type channel-waves at ten different receiver positions spanning the 2m thick seam. The waves propagated with very little dispersion and their amplitudes were virtually uniform across the seam. We conclude from these results that the asymmetrical position of the source in our theoretical channel models is unfavourable for the generation of symmetrical Love-type channel waves of the type observed by Krey.

We have not been able to simulate the SH-wave coda of the observed seismograms with the simple model structures described above, using a seismic source located outside the channel. Further work is required, to reformulate the anisotropic reflectivity technique so that the source may be located inside the reflection-zone, and to examine the nature of the acausal arrival which contributes to the asymmetrical appearance of the model seismograms. However, we have demonstrated the importance of a fluid-filled crack structure of the type believed to exist at Fenton Hill, in creating an efficient waveguide for shear-waves.

6.9 Conclusions

Seismograms of microseismic events have been recorded on a three-component geophone in a geothermal reservoir. An unusual characteristic feature of these seismograms is a low-frequency large-amplitude shear-wave arrival which propagates with little attenuation or dispersion and is polarized predominately in one component direction. From the geometry of the fluid-filled fractures in the geothermal reservoir, it is possible that this arrival may be due to shear-wave propagation in a waveguide bounded by two liquid-filled plane fractures. This channel is likely to be permeated by

microcracks which result from the thermal contraction of the hot rock during hydraulic pressurization of the reservoir. These cracks will be aligned with respect to the ambient tectonic stresses. This experimental situation has provided an application for the anisotropic reflectivity technique with the receiver located within the reflection-zone.

We have used the technique to investigate P-, SV-, and SH-wave propagation in a simple structure consisting of a channel separated from two isotropic halfspaces by thin liquid-filled cracks. A theoretical constraint of the anisotropic reflectivity technique as formulated in chapter 3 requires that the seismic source lies outside the channel. In the region of the source, direct contact of the channel with the halfspace containing the source was assumed in order to allow shear-wave energy to propagate into the channel. The parameters which were used to define the model structure were set to correspond as closely as possible to the experimental situation. In the case of SV- and SH-wave propagation, we have used different models to compare the effects which are produced by the presence or absence of anisotropy in the channel, and the presence or absence of liquid-filled cracks.

The reflectivity technique has a facility whereby the response in a layer can be truncated to the direct waves and the first multiple reflections. This facility is very useful in the investigation of wave propagation in a channel, since it permits the generation of seismograms of early wave arrivals which are not contaminated by time-aliased reverberations. We have used the facility in the investigation of non-linear P-wave first arrivals, unusual refracted waves preceding the direct SV-waves, and the formation of the early part of the SV-wave coda.

Non-linear P-wave motion has been observed experimentally, and ascribed to coupling between the geophone components. The above study has shown that the non-linearity can be explained by the existence of a channel

between two liquid-filled plane fractures. The interference of the direct and first reflected P-waves in the channel gives rise to the non-linear wave motion. We have also shown that the polarization direction of the first P-wave arrival does not necessarily indicate the direction of the source. P-wave polarizations and S-P times have been used by Pearson (1981) to locate microearthquakes caused by hydraulic pressurization of one of the fracture planes, and considerable scatter has been found in the locations. If allowance is made for the existence of the type of channel described above, the events could be located much nearer the fracture planes.

Shear-wave propagation in the channel is interesting because of the presence of the liquid layers. We have shown that an unusual SV-wave arrival, which propagates as a P head-wave in the channel over part of its wavepath, is present with larger than normal amplitude for this type of wave. Its amplitude is due to the boundary conditions at the interface with the liquid-filled cracks. The truncated SV-response has also been found to be useful in showing how the shear-wave coda varies according to the receiver position, due to the differing time-delays between successive reverberating wavelets.

The dependence of the form of the SV-wave coda on the receiver position is maintained in seismograms which are constructed with the complete SV-wave response, which includes all reverberations and converted waves. There is a low-frequency arrival, which is most clearly seen on the component which is normal to the fracture planes. The normal component of this arrival has opposite phases on either side of the centre of the channel, and it has zero amplitude in the centre of the channel. It propagates with a phase velocity which is below that of the lowest SV-wave velocity of the channel, and it is interpreted as a Rayleigh-type channel wave. The existence of this phase in the cracked channel has been shown to

depend on the existence of the liquid-filled cracks at the channel boundaries and, surprisingly, on P-wave reverberations in the liquid layers. Two different source types, a tension crack and a double-couple, have been used to generate SV-wave seismograms, and the channel-wave is present in both cases.

The polarization of the long, coherent, low-frequency wavetrain on the observed seismograms, with respect to the fracture geometry of the reservoir, suggests that the wavetrain is due to SH-wave propagation in the channel. SH-waves are most likely to generate a long reverberating wavetrain in a channel with liquid boundaries since they will be totally internally reflected within the channel. Initially, we used an SH-wave source pulse with the same dominant frequency as that which was used to generate the P- and SV-wave seismograms. A reverberating SH wavetrain was generated, but it did not have the frequency or the coherency of the observed wavetrain.

When a source wave pulse with the same frequency as that of the observed low-frequency wavetrain was used to generate the seismograms, a more coherent wavetrain was obtained, but there is asymmetry and dispersion in the SH-wave coda which is not present in the observed seismograms. A model structure with a thicker channel was used with the low-frequency SH-wave source, but again the resulting wavetrain observed at three different positions within the channel did not resemble the observed seismograms.

Thus while the models which have been used in the present study generate a reverberating SH wavetrain, the theoretical seismograms do not have the characteristics of the observed wavetrain, which is believed to be a Love-type channel-wave. Further theoretical work is required to indicate how the parameters of these models may be altered to generate the type of seismograms which have been observed experimentally. In particular, it is

likely that Love-type channel-waves of sufficiently large amplitude can only be generated by a source which is located within the channel.

We have assumed that the anisotropy in the channel has hexagonal symmetry, due to the presence of coplanar-normal water-saturated cracks. With the particular orientation of the microcracks which we have assumed, no anomalous phases are to be expected on the seismograms. Indeed, we have shown that there is little difference between the seismograms which have been generated for cracked and uncracked channels, particularly for SH-wave arrivals (albeit, the crack density of the channel has been set at the relatively low value of 0.1). However, microcracks do exist in the reservoir, as demonstrated by Fehler (1981) and Aki et al.(1982), and since they are likely to be aligned, then the media in the vicinity of the major-cracks will be anisotropic. Thus it is desirable to take account of this anisotropy in the generation of synthetic seismograms by using the anisotropic reflectivity technique.

However, it is difficult to describe a source in an anisotropic layer and at present the anisotropic reflectivity technique has not been extended to handle the case of a source in an anisotropic medium. Since the anisotropy is a second order effect for low crack-densities, channel wave studies of the structure at Fenton Hill could be carried out effectively by using isotropic techniques (Kennett & Kerry 1979), until an anisotropic formulation of the reflectivity technique for a buried source has been devised.

CHAPTER 7

SUGGESTIONS FOR FUTURE WORK

7.1 Theory

Computations involving anisotropic media take considerably more time than equivalent isotropic computations. The reflectivity technique for isotropic media itself requires long computing times which are directly proportional to the number of layers in the reflection-zone. Thus we have only been able to use a limited number of layers to define the reflection-zone when the technique is extended to anisotropic media. In particular, when the receiver was located in the reflection-zone, the models were limited to structures which consisted of five layers only, symmetrical about the layer containing the receiver. Although these configurations appear to be restrictive, practical applications are possible, and two applications have been described in chapters 5 and 6.

The possible extensions of the anisotropic reflectivity technique require widely varying amounts of theoretical effort. We present some possible future developments, in order of increasing complexity.

1. It is possible to increase the number of layers which can be used in creating a model structure. If the receiver is located outside the reflection-zone, all that is needed is an increase in computing capacity. In the case where the receiver is located in the reflection-zone, a reorganisation of the computer program will be required, where provision can be made for possible asymmetry of the structure with respect to the receiver layer.

2. The formulations of Kennett & Kerry (1979), which give the complete response of an isotropic stratified halfspace, are capable of extension to anisotropic media. These formulations include provision for the free surface effect above both source and receiver, and for the source as well as the receiver to be buried in the reflection-zone. Kennett (1980) includes the effect of near-field terms in the displacements and these should also be included in the anisotropic formulation, if synthetic seismograms are to be calculated at short ranges.

   There are theoretical problems associated with the description of the source, when it is located in a anisotropic medium. These problems arise because the direction of energy propagation for a given wave type is not in general parallel to the phase velocity vector. However, it would still be possible to use a source in an isotropic layer until these problems had been overcome. A useful first step towards a description of a general point source in an anisotropic medium, suitable for the reflectivity technique, has been accomplished by Kawasaki & Tanimoto (1981). They have calculated the equivalent body-forces for a dislocation in an anisotropic source medium, from which the body-wave radiation patterns can be obtained.

3. It has been stated in section 3.10 that the reflectivity technique for anisotropic media, as formulated in chapter 3, is an approximation which is applicable to weakly anisotropic media. True seismograms could be obtained by allowing each term in the expression to be a function of a horizontal wavenumber vector. A double integration over the two orthogonal components of this vector would then be required.

The implementation of all these improvements will result in much longer computing times, particularly in the case of (3) above. However, a

recent innovation in computing which should mitigate this effect is the Distributed Array Processor (DAP). In a DAP, arithmetic operations can be performed on arrays with the same efficiency as with single variables. The numerous 3 x 3 matrix manipulations in the anisotropic reflectivity technique makes it particularly well-suited for application to a DAP.

7.2 Upper-mantle studies

In chapter 5 we applied the anisotropic reflectivity technique to simple models of an upper-mantle with a realistic degree of anisotropy in the sub-Moho layer. The object of the study was to examine the feasibility of investigating upper-mantle anisotropy by the detection and analysis of anomalous arrivals which can be generated when wave propagate through, or are reflected from, anisotropic media.

The main conclusion of the present study is that it would only be marginally feasible to detect upper-mantle anisotropy by observation of shear-wave splitting on individual three-component seismograms. This conclusion was based on the study of synthetic seismograms, using very simple model structures in which the anisotropy was located in a layer immediately beneath the Moho. The degree of anisotropy was low, but it is probably realistic for that part of the upper-mantle. It has been recognised that these models are over-simplistic, due to computing restrictions, and that the first-order discontinuities in the model structures should be replaced by velocity gradients. When many more layers can be incorporated in the theoretical models, it will be possible to use more realistic structures to examine the anomalous arrivals.

In particular, it would be possible to study the effect of stronger anisotropy at greater depths than those considered in the present study. The presence of stronger anisotropy at depths of over 50 km is suggested from the high velocities found under many long refraction-profiles (Fuchs

1979). Also, it would be possible to follow the suggestion of Meissner & Flüh (1979) and model fine structure in the P-wave velocity-depth relationship in terms of anisotropic layers with different crystalline alignments. However, the inverse problem of analysing upper-mantle anisotropy by the detection and interpretation of anomalous arrivals is not likely to become more feasible than has been reported in the present study.

Synthetic seismograms are increasingly being used to provide amplitude information to aid the inversion of refraction-profile data in terms of P-wave velocity-depth structures. Whenever an azimuthal coverage of refraction-profiles in a localised area is obtained, and the travel-time observations suggest the presence of anisotropy, then the anisotropic reflectivity technique can assist with the inversion of the amplitude data.

7.3 Wave propagation in anisotropic channels

In chapter 6 we displayed seismograms of micro-earthquakes which were induced by hydraulic pressurization of a geothermal reservoir in hot dry rock. The seismograms show a distinctive shear-wave coda, and the fracture geometry of the reservoir suggests that this may be due to wave propagation in a channel between two extensive plane water-filled fractures. The media surrounding these fractures are likely to be permeated by micro-cracks caused by thermal contraction. These are unlikely to be randomly aligned, and thus the channel will be anisotropic.

We have used the anisotropic reflectivity technique and simple model structures to investigate some aspects of the propagation of P-, SV-, and SH-waves in a cracked channel. The form of the model structures are subject to some restrictions which are imposed by the theoretical formulation of the technique as described in chapter 3, and by the computing capacity available. In particular, the model structures must be

symmetric with respect to the channel, and the source must be located outside the channel and in an isotropic halfspace.

We have shown that experimentally-observed non-linear P-wave motion can be explained in terms of interfering P-waves within the channel. However, we have not explained the observed shear-wave coda satisfactorily with the limited number of models which have been used. Before we can confirm or reject the hypothesis that the form of the observed seismograms is due to the presence of the type of channel described above, further work is required.

The variation in the form of the seismograms with respect to two important parameters has not been adequately examined. We have shown that there are significant changes in the form of the seismograms if the thickness of the channel is increased from 10 to 20m. The results of Aamodt et al. (LASL HDR Staff 1978) show that the positional error in the wellbore surveys is not likely to be as large as 10m. However, it is suggested that synthetic seismograms be calculated for models with a range of channel thicknesses from 5 to 15m, in order to cover the experimental error of the wellbore surveys. Secondly, we have compared shear-wave seismograms for an isotropic channel and a cracked channel with a crack density of 0.1, but we have not used higher crack densities. If the crack density of the anisotropic material used in the present study was increased from 0.1 to 0.5, then the SV-wave velocity in the plane of the channel, and the SH-wave velocity in any direction in the channel, would drop from 3.189 to 2.868 km/s. Therefore the crack density would be expected to have a significant effect on the form of the shear-wave seismograms, and the SV-wave seismograms in particular. The degree of SV-wave anisotropy is 14% for a crack density of 0.5, which is relatively high. However, the anisotropic medium is transversely isotropic with a vertical axis of symmetry in the sagittal plane, and thus the assumption of weak anisotropy

in directions transverse to the sagittal plane, which was made in section 3.4, is not violated.

The polarization of the distinctive low-frequency shear-wave coda on the observed seismograms suggests that the coda is due to Love-type channel waves, which are generated most efficiently when the source is located within the channel. There are problems associated with the description of the source in an anisotropic medium, and considerable theoretical effort would be required to extend the anisotropic reflectivity technique to include a buried source in an anisotropic medium. However, since the cracked material which has been used in the present study is transversely isotropic, the P- and SV-wave motion decouples from the SH-wave motion and the material is effectively isotropic for SH-wave propagation. Thus if the study of the shear-wave coda is confined to that part due to SH-waves, an isotropic version of the reflectivity technique for a buried source (Kind 1978, Kennett & Kerry 1979) can be used to construct the synthetic seismograms. Alternatively, the Love-type channel wave seismograms could be constructed by the technique of mode summation, which Kerry (1981) has used to synthesise Rayleigh-wave seismograms for two Earth models.

To calculate the dispersion curves for his models, Kerry uses a technique which is based on the expression derived by Kennett & Kerry (1979) for the response of a stratified medium. This technique could be extended to anisotropic stratified media in the same way as Kennett's (1974) iterative algorithm was extended to anisotropic media in section 3.6. Dispersion curves of channel-wave modes could then be calculated not only for the transversely isotropic channel which has been discussed above, but for channels with more general types of anisotropy. In the general case, the channel-wave motion will not degenerate into separate Rayleigh-type and Love-type modes. The Rayleigh- and Love-type modes will be coupled in a manner similar to the generalised surface waves described by

Crampin (1977a).

A coal seam is a good example of a channel which is likely to possess general anisotropic symmetry. The pressure of the overburden will induce transverse isotropy, and the one or more cleavage planes which will be present perpendicular to the bedding plane will give a parallel or biplanar system of cracks (Jackson, Buchanan & Davis 1982). Channel-waves have been used effectively for the detection of faults in coal seams (Buchanan et al. 1981), and the misplacement of reflecting horizons due to anisotropy has been demonstrated by Jackson et al. (1982). It is not possible to use synthetic seismograms to investigate channel-waves generated by a source in an anisotropic coal seam with the present formulation of the anisotropic reflectivity technique. However, dispersion curves could be calculated for the generalised channel-waves to aid their interpretation on observed seismograms.

REFERENCES

Ahrens, T.J.,1972. The state of mantle minerals, Tectonophys., 13, 189-220.

Aki,K., Fehler,M., Aamodt,R.L., Albright,J.N., Potter,R.M., Pearson,C.M., & Tester,J.W.,1982. Interpretation of seismic data from hydraulic fracturing experiments at the Fenton Hill, New Mexico, hot dry rock geothermal site, J.geophys.Res., 87, 936-944.

Aki,K., & Richards,P.G.,1980. Quantitative seismology, W.H.Freeman, San Francisco, 932pp.

Ando,M., Ishikawa,Y. & Wada,H.,1980. S-wave anisotropy in the upper mantle under a volcanic area in Japan, Nature, 286, 43-46.

Ansorge,J., Bonjer,K.P., & Emter,D.,1979. Structure of the uppermost mantle from long range seismic observations in Southern Germany and the Rhinegraben area, Tectonophys., 56, 31-48.

Asada,T., & Shimamura,H.,1979. Long range refraction experimemts in deep ocean, Tectonophys., 56, 67-82.

Assumpção,M.,1980. Determination of Moho dip using PS reflections, Geophys.J.R.astr.Soc., 60, 77-84.

Ave'Lallemant,H.G., & Carter,N.L.,1970. Syntectonic recrystallisation of olivine and modes of flow in the upper mantle, Geol.Soc.Am.Bull., 81, 2203-2220.

Backus,G.E.,1962. Long-wave elastic anisotropy produced by horizontal layering, J.geophys.Res., 67, 4427-4440.

Backus,G.E.,1965. Possible forms of seismic anisotropy of the uppermost mantle under oceans, J.geophys.Res., 70, 3429-3439.

Bamford,D.,1973. Refraction data in Western Germany - a time-term interpretation, Z.Geophys., 39, 907-927.

Bamford,D.,1977. Pn velocity anisotropy in a continental upper mantle, Geophys.J.R.astr.Soc., 49, 29-48.

Bamford,D., & Crampin,S.,1977. Seismic anisotropy - the state of the art. Geophys.J.R.astr.Soc., 49, 1-8.

Bamford,D., Jentsch,M., & Prodehl,C.,1979. Pn anisotropy studies in northern Britain and the eastern and western United States, Geophys.J.R.astr.Soc., 57, 397-429.

Bamford,D., & Nunn,K.R.,1979. In situ seismic measurements of crack anisotropy in the Carboniferous limestone of Northwest England, Geophys.Prosp., 27, 322-338.

Birch,F.,1960. Velocity of compressional waves in rocks to ten kilobars, Part I, J.geophys.Res., 65, 1083-1102.

Birch,F.,1961. Velocity of compressional waves in rocks to ten kilobars, Part II, J.geophys.Res., 66, 2199-2224.

Braille,L.W., & Smith,R.B.,1975. Guide to the interpretation of crustal refraction profiles, Geophys.J.R.astr.Soc., 40, 145-176.

Brekhovskikh,L.M.,1960. Waves in layered media, Academic Press, New York.

Brown,M.C., Duffield,R.B., Siciliano,C.L.B., & Smith,M.C.(editors),1979. Hot dry rock geothermal energy development program: annual report: fiscal year 1978, University of California, Los Alamos National Laboratory, (LA-7807-HDR. UC-66a).

Buchanan,D.J., Davis,R., Jackson,P.J., & Taylor,P.M.,1981. Fault location by channel wave seismology in United Kingdom coal seams, Geophys., 46, 994-1002.

Červený,V., & Ravindra,R.,1971. Theory of seismic head waves, Univ.Toronto Press., Toronto.

Christensen,N.I.,1982. In Carmichael,R.S.(ed.), Handbook of physical properties of rocks Vol.II, CRC Press, Boca Raton, USA.

Crampin,S.,1966. Higher modes of seismic surface waves: propagation in Eurasia, Bull.seism.Soc.Am., 56, 1227-1339.

Crampin,S.,1967. Coupled Rayleigh-Love second modes, Geophys.J.R.astr.Soc., 12, 229-235.

Crampin,S.,1970. The dispersion of surface waves in multilayered anisotropic structures, Geophys.J.R.astr.Soc., 21, 387-402.

Crampin,S.,1975. Distinctive particle motion of surface waves as a diagnostic of anisotropic layering, Geophys.J.R.astr.Soc., 40, 177-186.

Crampin,S.,1976. A comment on 'The early structural evolution and anis of the oceanic upper mantle', Geophys.J.R.astr.Soc., 46, 193-197.

Crampin,S.,1977a. A review of the effects of anisotropic layering on the propagation of body waves, Geophys.J.R.astr.Soc., 49, 9-27.

Crampin,S.,1977b. Paleoanisotropy in the upper mantle, Nature, 270, 162-163.

Crampin,S.,1978. Seismic wave propagation through a cracked solid: polarization as a possible dilatancy diagnostic, Geophys.J.R.astr. Soc., 53, 467-496.

Crampin,S.,1981. A review of wave motion in anisotropic and cracked elastic-media, Wave Motion, 3, 343-391.

Crampin,S., & Bamford,D.,1977. Inversion of P-wave velocity anisotropy, Geophys.J.R.astr.Soc., 49, 123-132.

Crampin,S., Evans,R., Üçer,B., Doyle,M., Davis,J.P., Yegorkina,G.V. & Miller,A.,1980. Observations of dilatancy-induced polarization anomalies and earthquake prediction, Nature, 286, 874-877.

Crampin,S., Evans,R., & Atkinson,B.K.,1982. Earthquake prediction: a new physical basis, Nature, submitted.

Crampin,S., & King,D.W.,1977. Evidence for anisotropy in the upper mantle beneath Eurasia from the polarization of higher mode seismic surface waves, Geophys.J.R.astr.Soc., 49, 59-85.

Crampin,S., & Kirkwood,S.C.,1981. Velocity variations in systems of anisotropic symmetry, J.geophys., 49, 35-42.

Crampin,S., & McGonigle,R.,1981. The variation of delays in stress-induced anisotropic polarization anomalies, Geophys.J.R.astr.Soc., 64, 115-131.

Crampin,S., McGonigle,R., & Bamford,D.,1980. Estimating crack parameters from observations of P-wave velocity anisotropy, Geophys., 45, 345-360.

Crampin,S., & Radovich,B.J.,1981. Interpretation of synthetic common-depth-point gathers for a single anisotropic layer, Geophys., 47, 323-335.

Crampin,S., Stephen,R.A, & McGonigle,R.,1982. The polarization of P waves in anisotropic media, Geophys.J.R.astr.Soc., 68, 477-485.

Crampin,S., & Yedlin,M.,1981. Shear-wave singularities of wave propagation in anisotropic media, J.geophys., 49, 43-46.

Cremer,G.M.(editor),1981. Hot dry rock geothermal energy development program: annual report: fiscal year 1980, University of California, Los Alamos National Laboratory, (LA-8855-HDR. UC-66a,.

Dunkin,J.W.,1965. Computation of modal solutions in layered media at high frequencies, Bull.seism.Soc.Am., 55, 335-358.

Edel,J.B., Fuchs,K., Gelbke,C., & Prodehl,C.,1975. Deep structure of the southern Rhinegraben area from seismic refraction investigations, J.Geophys., 41, 333-356.

Ewing,M., Jardetsky,W.S., & Press,F.,1957. Elastic waves in layered media, McGraw-Hill, New York, 380pp.

Faber,S.,1978. Refraktionsseismiche Untersucherung der Lithosphäre unter den britischen Inseln, Ph.D.thesis, Univ. Karlsruhe, 132pp.

Fertig,J., & Müller,G.,1978. Computations of synthetic seismograms for coal seams with the reflectivity method, Geophys.Prosp., 26, 868-883.

Forsyth,D.W.,1975. The early structural evolution and anisotropy of the oceanic upper mantle, Geophys.J.R.astr.Soc., 43, 103-162.

Francis,T.J.G.,1969. Generation of seismic anisotropy in the Upper Mantle along the mid-oceanic ridges, Nature, 221, 162-165.

Fryer,G.J.,1980. A slowness approach to the reflectivity method of seismogram synthesis, Geophys.J.R.astr.Soc., 63, 747-758.

Fuchs,K.,1968a. The reflection of spherical waves from transition zones with arbitrary depth-dependent elastic moduli and density, J.Phys.Earth, 16, special issue, 27-41.

Fuchs,K.,1968b. Das Reflexions- und transmissionsvermögen eines geschichteten Mediums mit beliebiger Tiefen-Verteilung der elastischen Moduln und der Dichte für schrägen Einfall ebener Wellen, Z.Geophys., 34, 389-413.

Fuchs,K.,1970. On the determination of velocity-depth distributions of elastic waves from the dynamic characteristics of the reflected wave field, Z.Geophys., 36, 531-547.

Fuchs,K.,1971. The method of stationary phase applied to the reflection of spherical waves from transition zones with arbitrary depth-dependent elastic moduli and density, Z.Geophys., 37, 89-117.

Fuchs,K.,1975. Synthetic seismograms of PS-reflections from transition zones computed using the reflectivity method, J.Geophys., 41, 445-462.

Fuchs,K.,1977. Seismic anisotropy of the subcrustal lithosphere as evidence for dynamical processes in the upper-mantle, Geophys.J.R.astr.Soc., 49, 167-179.

Fuchs,K.,1979. Structure, physical properties and lateral heterogeneities of the subcrustal lithosphere from long-range deep seismic sounding observations on continents, Tectonophys., 56, 1-15.

Fuchs,K., & Müller,G.,1971. Computation of synthetic seismograms with the reflectivity method and comparison with observations, Geophys.J.R. astr.Soc., 23, 417-433.

Garbin,H.D., & Knopoff,L.,1973. The compressional modulus of a material permeated by a random distribution of free circular cracks, Q.Appl. Math., 30, 453-464.

Garbin,H.D., & Knopoff,L.,1975a. The shear modulus of a material permeated by a random distribution of free circular cracks, Q.Appl.Math., 33, 296-300.

Garbin,H.D., & Knopoff,L.,1975b. Elastic moduli of a medium with liquid-filled cracks, Q.Appl.Math., 33, 301-303.

Graham,E.K., & Barsch,G.R.,1969. Elastic constants of single-crystal fosterite as a function of temperature and pressure, J.geophys.Res., 74, 5949-5960.

Gilbert,F., & Backus,G.E.,1966. Propagator matrices in elastic wave and vibration problems, Geophys., 31, 326-332.

Haskell,N.A.,1953. The dispersion of surface waves in multilayered media, Bull.seism.Soc.Am., 43, 17-34.

Hess,H.,1964. Seismic anisotropy of the uppermost mantle under oceans, Nature, 203, 629-631.

Hirn,A.,1977. Anisotropy in the continental upper mantle: possible evidence from explosion seismology, Geophys.J.R.astr.Soc., 49, 49-58.

Hirn,A., Steinmetz,L., Kind,R., & Fuchs,K.,1973. Long range profiles in Western Europe: II. Fine structure of the lower lithosphere in France (Southern Bretagne), Z.geophys., 39, 363-384.

Hron,F., & Kanasewich,E.R.,1971. Synthetic seismograms for deep sounding studies using asymptotic ray theory. Bull.seism.Soc.Am., 61, 1169-1200.

Hron,F., Kanasewich,E.R., & Alpaslan,T.,1974. Partial ray expansion required to suitably approximate the exact wave solution, Geophys. J.R.astr.Soc., 36, 607-625.

Hudson,J.A.,1969. A quantitative evaluation of seismic signals at teleseismic distances: I. - radiation from a point source, Geophys. J.R.astr.Soc., 18, 233-249.

Jackson,P.J., Buchanan,D.J., & Davis,R.,1982. Attenuation and anisotropy of channel waves in coal seams, Geophys., submitted.

Jacob,A.W.B., & Booth,D.C.,1977. Observations of PS reflections from the Moho, J.geophys., 43, 687-692.

Kaarsberg,E.A.,1968. Elasticity studies of isotropic and anisotropic rock samples, Trans.Soc.Min.Eng., 241, 470-475.

Kawasaki,I., & Tanimoto,T.,1981. Radiation patterns of body waves due to the seismic dislocation occurring in an anisotropic source medium, Bull.seism.Soc.Am., 71, 37-50.

Keith,C.M.,1975. Propagation of seismic body waves in layered anisotropic structures, Ph.D.thesis, University of Edinburgh.

Keith,C.M. & Crampin,S.,1977a. Seismic body waves in anisotropic media: reflection and refraction at a plane interface, Geophys.J.R.astr.Soc., 49, 181-208.

Keith,C.M. & Crampin,S.,1977b. Seismic body waves in anisotropic media: propagation through a layer, Geophys.J.R.astr,Soc., 49, 209-223.

Keith,C.M. & Crampin,S.,1977c. Seismic body waves in anisotropic media: synthetic seismograms, Geophys.J.R.astr,Soc., 49, 225-243.

Kennedy,G.C., & Higgins,G.H.,1972. Melting temperatures in the Earth's mantle, Tectonophys, 13, 221-232.

Kennett,B.L.N.,1974. Reflections,rays, and reverberations, Bull.seism. Soc.Am., 64, 1685-1696.

Kennett,B.L.N.,1975a. Theoretical seismogram calculation for laterally varying crustal structures, Geophys.J.R.astr.Soc., 42, 579-589.

Kennett,B.L.N.,1975b. The effects of attenuation on seismograms, Bull.seism. Soc.Am., 65, 1643-1651.

Kennett,B.L.N.,1979. Theoretical reflection seismograms for elastic media, Geophys.Prosp., 27, 301-321.

Kennett,B.L.N.,1980. Seismic waves in a stratified halfspace - II. Theoretical seismograms, Geophys.J.R.astr.Soc., 61, 1-10.

Kennett,B.L.N., & Kerry,N.J.,1979. Seismic waves in a stratified halfspace, Geophys.J.R.astr.Soc., 57, 557-583.

Kerry,N.J.,1981. Synthesis of seismic surface waves, Geophys.J.R.astr.Soc., 64, 425-446.

Kind,R.,1974. Long range propagation of seismic energy in the lower lithosphere, J.geophys., 40, 189-202.

Kind,R.,1976. Computation of reflection coefficients for layered media, J.geophys., 42, 191-200.

Kind,R.,1978. The reflectivity method for a buried source, J.geophys., 44, 603-612.

Kind,R.,1979. Extensions of the reflectivity method, J.geophys., 45, 373-380.

Kind,R., & Müller,G.,1975. Computations of SV waves in realistic earth models, J.geophys., 41, 149-172.

Kirkwood,S.C.,1978. Seismic surface-waves and anisotropic alignments in the oceanic upper-mantle, Ph.D.thesis, University of Edinburgh.

Kirkwood,S.C., & Crampin,S.,1980a. Surface-wave propagation in an ocean basin with an anisotropic upper mantle: numerical modelling, Geophys.J.R.astr.Soc., 64, 463-485.

Kirkwood,S.C., & Crampin,S.,1980b. Surface-wave propagation in an ocean basin with an anisotropic upper mantle: observations of polarization anomalies, Geophys.J.R.astr.Soc., 64, 487-497.

Krey,T.C.,1963. Channel-waves as a tool of applied geophysics in coal mining, Geophys., 28, 701-714.

Krey,T., & Helbig,K.,1956. A theorem concerning anisotropy of stratified media and its significance for reflecting seismics, Geophys.Prosp., 4, 294-302.

Kumazawa,M.,1969. The elastic constants of single-crystal orthopyroxene, J.geophys.Res., 74, 5973-5980.

Kumazawa,M., & Anderson,O.L.,1969. Elastic moduli, pressure derivatives, and temperature derivatives of single-crystal olivine and single-crystal fosterite, J.geophys.Res., 74, 5961-5972.

LASL HDR Project Staff,1978. Hot dry rock geothermal energy development program: annual report: fiscal year 1977, University of California, Los Alamos National Laboratory, (LA-7109-PR, UC-66a).

Leven,J.H., Jackson,I., & Ringwood,A.E.,1981. Upper mantle seismic anisotropy and lithospheric decoupling, Nature, 289, 234-239.

Levin,F.K.,1978. The reflection, refraction, and diffraction of waves in media with an elliptical velocity dependence, Geophys., 43, 528-537.

Levin,F.K.,1979. Seismic velocities in transversely isotropic media, Geophys., 44, 918-936.

Lucas,A.L., O'Brien,P.N.S., & Thomas,J.H.,1980. Velocity analysis in transversely isotropic media, Geophys., 45, 1094-1095.

McGonigle,R., & Crampin,S.,1982. A Fortran program to evaluate the phase and group velocity surface in an anisotropic solid, Computers and Geosciences, in press.

Meissner,R.O., & Flüh,E.R.,1979. Probable relations between seismic anisotropyand a fine structure of the lithosphere, J.geophys., 45, 349-352.

Müller,G.,1968a. Theoretical seismograms for some types of point-sources in layered media, Part I : Theory, Z.geophys., 34, 15-35.

Müller,G.,1968b. Theoretical seismograms for some types of point-sources in layered media, Part II : Numerical calculations, Z.geophys., 34, 147-162.

Müller,G.,1969. Theoretical seismograms for some types of point-source in layered media, Part III : Single force and dipole sources of arbitrary orientation, Z.geophys., 35, 347-371.

Müller,G.,1970. Exact ray theory and its application to the reflection of elastic waves from vertically inhomogeneous media, Geophys.J.R.astr. Soc., 21, 261-283.

Müller,G.,1973. Theoretical body wave seismograms for media with spherical symmetry - discussion and comparison of approximate methods, Z.geophys., 39, 229-246.

Müller,G., & Kind,R.,1975. Observed and computed seismogram sections for the whole Earth, Geophys.J.R.astr.Soc., 44, 699-716.

Pearson,C.,1981. The relationship between microseismicity and high pore pressures during hydraulic stimulation experiments in low permeability granitic rocks, J.geophys.Res., 86, 7855-7864.

Pilant,W.L.,1979. Elastic waves in the Earth, Elsevier, Amsterdam.

Postma,G.W.,1955. Wave propagation in a stratified medium, Geophys., 20, 780-806.

Raitt,R.W., Shor,G.G., Francis,T.J.G., & Morris,G.B.,1969. Anisotropy of the Pacific upper mantle, J.geophys.Res., 74, 3095-3109.

Schlue,J.W., & Knopoff,L.,1976. Shear wave anisotropy in the upper mantle of the Pacific basin, Geophys.Res.Lett., 3, 359-362.

Schlue,J.W., & Knopoff,L.,1977. Shear-wave anisotropy in the Pacific basin, Geophys.J.R.astr.Soc., 49, 145-165.

Singh,J.,1982. The detection of upper-mantle anisotropy from observations of anomalous teleseismic shear-waves, Ph.D.Thesis, University of Edinburgh.

Stephen,R.A.,1977. Synthetic seismograms for the case of the receiver within the reflectivity zone, Geophys.J.R.astr.Soc., 51, 169-181.

Taylor,D.B., & Crampin,S.,1978. Seismic surface waves in anisotropic media: propagation in a homogeneous piezoelectric halfspace, Proc.R.Soc.A., 364, 161-179.

Thomson,W.T.,1950. Transmission of elastic waves through a stratified solid medium, J.Appl.Phys., 21, 89-93.

Todd,T., Simmons,G., & Baldridge,W.S.,1973. Acoustic double refraction in low-porosity rocks, Bull.seism.Soc.Am., 63, 2007-2020.

Tolstoy,I., & Usdin,E.,1953. Dispersive properties of stratified elastic and liquid media: a ray theory, Geophys., 18, 844-870.

Verma,R.K.,1960. Elasticity of some high-density crystals, J.geophys. Res., 65, 757-766.

Waters,K.H.,1978. Reflection seismology : a tool for energy resource exploration, Wiley, 377pp.

Watson,T.H.,1970. Fast computation of Rayleigh wave dispersion in a layered halfspace, Bull.seism.Soc.Am., 60, 161-166.

White,J.E.,1965. Seismic waves : radiation, transmission, and attenuation, McGraw-Hill, New York.

White,J.E. & Sengbush,R.L.,1953. Velocity measurements in near-surface formations, Geophys., 18, 54-69.

Wiggins,R.A., & Helmberger,D.V.,1974. Synthetic seismogram computation by expansion in generalised rays, Geophys.J.R.astr.Soc., 37, 73-90.

Yegorkina,G.V., Rakitov,V.A., Garetovskaya,I.V., & Yegorova,L.M.,1977. Anisotropy of velocities of seismic waves and the stress state of the Earth's crust in the territory of Armenia, Izv. Akad. Naut. SSSR. Fiz. Zemli, No.8, 43-55 (in Russian), 554-562 (AGU, English translation).

APPENDIX 1 The relationship between displacement excitation factors and potential excitation factors in isotropic media.

In order to show how the above relationship may be obtained, we first obtain a relation between the plane wave displacement amplitudes and plane wave potentials for each wave-type in an isotropic layer. The derivation is based on a suggestion by Gerhard Müller (personal communication). It is assumed that there is cylindrical symmetry about the z axis. We follow the notation of chapter 2.

1. P-waves

A simple solution to the appropriate wave equation in (2.3.1) for the potential of a plane P-wave propagating Downwards in the sagittal plane in the isotropic mth layer is given by

$$\Phi^m_{PD}(r,z,\omega) = J_o(kr).\exp[-i\nu^m_1(z-d_m)] , \qquad (A1.1)$$

where $\nu^m_j = \omega q^m_j$, $j = 1,2,3$. The corresponding plane wave displacements are calculated from (A1.1) by using (2.3.2). They are

$$u^m_r = -k.J_1.\exp[-i\nu^m_1(z-d_m)] ,$$
and
$$u^m_z = -i\nu_1.J_o.\exp[-i\nu^m_1(z-d_m)] \qquad (A1.2)$$

We assume that the displacements are to be calculated in the far field, where $J_1 \sim iJ_o$. Then the amplitude of the resultant displacement vector for a Downward P-wave is

$$u^m_{PD} = -ik^m_1.J_o.\exp[-i\nu^m_1(z-d_m)] . \qquad (A1.3)$$

The sign of the amplitude is determined by the requirement that the component displacement amplitudes (A1.2) are given by multiplying (A1.3) by the appropriate components of the polarization vector, which are given in Table (2.1). Similarly the displacement amplitude for an Upward P-wave is

$$u^m_{PU} = -ik^m_1 . J_o . \exp[i\nu^m_1 (z-d_m)] \quad . \tag{A1.4}$$

Thus for upward and downward P-waves the ratio of plane wave displacement amplitude to plane wave potential is, from (A1.1), (A1.3) and (A1.4),

$$(u/\Phi)^m_P = -ik^m_1 \quad . \tag{A1.5}$$

2. SV-waves

We follow a procedure similar to that given up for P-waves. The plane wave potential for a downward SV-wave is

$$\Phi^m_{SVD}(r,z,\omega) = J_o . \exp[-i\nu^m_2 (z-d_m)] \quad . \tag{A1.6}$$

The plane wave displacement components are, from (2.3.2),

$$u_r = i\nu^m_2 k . J_1 . \exp[-i\nu^m_2 (z-d_m)]$$

and (A1.7)

$$u_z = k^2 . J_o . \exp[-i\nu^m_2 (z-d_m)]$$

The far field resultant displacement amplitude is

$$u^m_{SVD} = -kk^m_2 . J_o . \exp[-i\nu^m_2 (z-d_m)] \tag{A1.8}$$

and so for downward SV-waves, the displacement/potential ratio is

$$(u/\Phi)^m_{SVD} = -kk^m_2 \tag{A1.9}$$

Similarly it may be shown that for upward propagating SV-waves

$$(u/\Phi)^m_{SVU} = kk^m_2 \tag{A1.10}$$

3. SH-waves

The plane wave potential of a downward SH-wave is

$$\Phi^m_{SHD}(r,z,\omega) = J_o.\exp[-i\nu^m_2(z-d_m)] \quad , \tag{A1.11}$$

and the far field displacement in the transverse direction is, from (2.3.2),

$$u^m_{SHD} = k.J_1.\exp[-i\nu^m_2(z-d_m)] \tag{A1.12}$$

It is easily shown that for both upward and downward SH-waves,

$$(u/\Phi)^m_{SH} = ik \tag{A1.13}$$

From the above relations (A1.5), (A1.9), (A1.10) and (A1.13) we can derive relationships between the displacement excitation factors and the potential excitation factors in isotropic media.

We shall consider a P-wave in layer 0 incident downwards on the reflection zone. Then the plane wave potential vectors in layers 0 and n are

$$\underline{\Phi}^0 = (1 , 0 , 0 , g^0_1(4) , g^0_1(5) , g^0_1(6))^T J_o \quad ,$$

and

$$\underline{\Phi}^n = (g^n_1(1) , g^n_1(2) , g^n_1(3) , 0 , 0 , 0)^T J_o \tag{A1.14}$$

respectively, from equations (2.4.6) and (2.4.7).

The corresponding displacement vectors in layers 0 and n may be written

$$\underline{u}^0 = (1 , 0 , 0 , f^0_1(4) , f^0_1(5) , f^0_1(6))^T J_o \quad ,$$

and

$$\underline{u}^n = (f^n_1(1) , f^n_1(2) , f^n_1(3) , 0 , 0 , 0)^T J_o \quad . \tag{A1.15}$$

As an example of how the relationships between the potential and

displacement excitation factors may be formed, consider the factors $g_1^0(5)$ and $f_1^0(5)$. From (A1.15) we have

$$u^0(5) = f_1^0(5).u^0(1) \ , \qquad \text{(A1.16)}$$

and by substitution from (A1.5) and (A1.10) it follows that

$$kk_2^0 \, \Phi^0(5) = f_1^0(5).-ik_1^0 \, \Phi^0(1) \qquad \text{(A1.17)}$$

From (A1.14) we have

$$\Phi^0(5) = g_1^0(5). \, \Phi^0(1) \ , \qquad \text{(A1.18)}$$

therefore it follows from (A1.17) and (A1.18) that

$$f_1^0(5) = -(kk_2^0/ik_1^0).g_1^0(5) \ . \qquad \text{(A1.19)}$$

Expressions which relate the other displacement excitation factors to their corresponding potential excitation factors may be derived in a similar way. In particular,

$$f_1^0(4) = g_1^0(4) \qquad \text{(A1.20)}$$

and

$$f_1^0(6) = -(k/k_1^0).g_1^0(6) \ . \qquad \text{(A1.21)}$$

We include the expression (A1.21) although $g_1^0(6)$ is zero for isotropic media, since it becomes non-zero for anisotropic media.

APPENDIX 2 Wave displacements due to a point explosive source, expressed in terms of displacement excitation factors.

We shall write the integral expressions for the displacements in layer 0 due to a point explosive source at the surface, in terms of displacement excitation factors $f_1^0(n)$. We shall use the relations between the displacement and potential excitation factors which were obtained in Appendix 1.

It will be convenient to use the shorthand expressions

$$\nu_1 = -\omega q_4^0, \quad \nu_2 = -\omega q_5^0 = -\omega q_6^0, \quad k_1 = k_1^0, \quad k_2 = k_2^0 ,$$

$$R_{PP} = g_1^0(4), \quad R_{PV} = g_1^0(5), \quad R_{PH} = g_1^0(6) ,$$

$$\Omega_{PP} = \Omega_1^0(4), \quad \Omega_{PV} = \Omega_1^0(5), \text{ and } \quad \Omega_{PH} = \Omega_1^0(6) .$$

From (2.3.4) we have

$$\Omega_{PP} = \int_0^\infty \frac{k}{i\nu_1} . R_{PP} . J_o . \exp(i\nu_1 z) . dk \quad , \tag{A2.1}$$

$$\Omega_{PV} = \int_0^\infty \frac{k}{i\nu_1} . R_{PV} . J_o . \exp(i\nu_2 z) . dk \quad , \text{ and} \tag{A2.2}$$

$$\Omega_{PH} = \int_0^\infty \frac{k}{i\nu_1} . R_{PH} . J_o . \exp(i\nu_2 z) . dk \tag{A2.3}$$

The vertical, radial, and transverse displacements corresponding to equations (A2.1), (A2.2) and (A2.3) are obtained by the application of the equations (2.3.2). They are

$$u_{PP}^z = \int_0^\infty k . R_{PP} . J_o . \exp(i\nu_1 z) . dk ,$$

$$u_{PV}^z = \int_0^\infty \frac{k^3}{i\nu_1} . R_{PV} . J_o . \exp(i\nu_2 z) . dk , \tag{A2.4}$$

$$u_{PP}^r = \int_0^\infty \frac{-k^2}{\nu_1} . R_{PP} . J_o . \exp(i\nu_1 z) . dk ,$$

$$u^r_{PV} = \int_0^\infty \frac{k^2 \nu_2}{i\nu_1} . R_{PV} . J_o . \exp(i\nu_2 z) . dk \quad , \text{ and}$$

$$u^t_{PH} = \int_0^\infty \frac{k^2}{\nu_1} . R_{PH} . J_o . \exp(i\nu_2 z) . dk \quad . \qquad \text{(A2.4) contd.}$$

Each integrand in the above expressions may be rewritten in terms of a source term and the amplitude vector for each wave-type which corresponds to the component:

$$u^z_{PP} = \int_0^\infty \frac{-kk_1}{\nu_1} \left(\frac{-\nu_1}{k_2}\right) R_{PP} . J_o . \exp(i\nu_1 z) . dk \quad ,$$

$$u^z_{PV} = \int_0^\infty \frac{-kk_1}{\nu_1} \left(\frac{k}{k_2}\right) \frac{-kk_2}{ik_1} . R_{PV} . J_o . \exp(i\nu_2 z) . dk \quad ,$$

$$u^r_{PP} = \int_0^\infty \frac{-kk_1}{\nu_1} \left(\frac{k}{k_1}\right) R_{PP} . J_o . \exp(i\nu_1 z) . dk \quad , \qquad \text{(A2.5)}$$

$$u^r_{PV} = \int_0^\infty \frac{-kk_1}{\nu_1} \left(\frac{\nu_2}{k_2}\right) \frac{-kk_2}{ik_1} . R_{PV} . J_o . \exp(i\nu_2 z) . dk \quad , \text{ and}$$

$$u^t_{PH} = \int_0^\infty \frac{-kk_1}{\nu_1} \left(1\right) \frac{-k}{k_1} . R_{PH} . J_o . \exp(i\nu_2 z) . dk \quad .$$

By applying the relations (A1.19-21) which were derived in Appendix 1, it is easily seen that the displacement components u_i, i = 1,2,3 of the upward wave-types p, p = 4,5,6 may be written in cartesian coordinates as

$$u_i = \sum_{p=4}^{6} \int_0^\infty S_1 . f_1^0(p) . a_i^0(p) . J_o(kx_1) . \exp(-i\omega q_p^0 x_3) . dk \qquad \text{(A2.6)}$$

where $a_i^0(p)$ and S_1 (= $-kk_1/\nu_1$) are given in Tables 2.1 and 2.2 respectively.

Thus we have expressed the integral expressions for the displacements in (A2.4) as integrals of plane wave displacements of the type given by (2.5.2), multiplied by a source term S_1 which depends on the source type.

APPENDIX 3 The determination of elastic constants for materials exhibiting crystalline anisotropy and crack-anisotropy.

1. Elastic constants for crystalline anisotropy

Elastic constants have been measured ultrasonically for the crystalline minerals believed to form the major constituents of upper-mantle rocks. The upper-mantle is thought to consist of mainly olivine (60-70%) with ortho- and clinopyroxene (15-20% each) (Ahrens 1972, Kennedy and Higgins 1972). The ultrasonic measurements made by Verma (1960), Kumazawa (1969), Kumazawa and Anderson (1969), Graham and Barsch (1969) show a strong velocity-anisotropy of 15-25% for P-waves. The orthorhombic minerals (ie olivine and orthopyroxene) have maximum P velocity for propagation along the crystallographic a-axis, with minimum P velocity for propagation along the b-axis. The P velocity maximum for clinopyroxenes is close to the c-axis (Kumazawa 1969).

The mineral grains in mantle rocks are unlikely to be perfectly or uniformly aligned. It is therefore only to be expected that the observed velocity-anisotropy of the upper-mantle is much smaller than that observed in mineral crystals. For a material displaying a weaker anisotropy than that of mineral crystals, the elastic constants may be obtained by mixing isotropic material with the appropriate crystalline anisotropic material. The elastic constants of the mixed material can be written

$$c^{M}_{jkmn} = (1 - \varepsilon)\, c^{I}_{jkmn} + \varepsilon c^{A}_{jkmn} , \qquad (A3.1)$$

where ε is the percentage of anisotropic material and c^{M}_{jkmn}, c^{I}_{jkmn} and c^{A}_{jkmn} are the elastic constants of mixed, isotropic and anisotropic material, respectively.

Crampin and Bamford (1977) inverted observed azimuthal Pn velocity variations in the Pacific and South Germany in terms of different mixtures of isotropic material and ortho- and transversely isotropic olivine. In modelling the velocity variations, Crampin and Bamford used a relation derived by Crampin (1977a) from work by Backus (1965) for the azimuthal velocity variation for each wave-type.

For a material exhibiting weak anisotropy with a sagittal plane of symmetry, the azimuthal velocity variations of the propagating quasi-P (qP) wave and the two quasi-shear waves (qSV, qSH) may be written in the form of the reduced equations

$$\begin{aligned} V^2_{qP} &= A + B\cos 4\theta + C\cos 4\theta \\ V^2_{qSH} &= D + E\cos 4\theta \\ V^2_{qSV} &= F + G\cos 2\theta \end{aligned} \qquad \text{(A3.2)}$$

(Crampin 1977a). The constants A to G are linear combinations of six independent elastic constants. The qSH-wave is defined as the shear-wave with polarization most nearly parallel to the plane of variations, and the qSV-wave as that most nearly perpendicular. Crampin and Bamford set the observed P-wave velocity variations in the form of the first of the equations (A3.2). An anisotropic material likely to be found in the upper mantle (ortho- or transversely isotropic olivine) was chosen, to be mixed with an isotropic material in modelling the velocity variations. The proportion of isotropic material, and its elastic constants was found by solving equations relating the theoretical velocity variations and the observed variations, for two orthogonal directions along axes of symmetry in the horizontal plane. Suitable proportions of an isotropic material mixed with ortho- or transversely isotropic olivine were found to fit observed velocity variations in the Pacific almost exactly. However, it

was not possible to fit the observed continental velocity variations as well over the whole azimuthal range. The study showed that measurements of Pn-wave velocity variations in one plane can only give very limited information about the anisotropic properties of a refractor, unless a number of assumptions can be made. Nevertheless, Crampin & Bamford's results have provided us with a reasonably realistic set of elastic constants for the anisotropic upper-mantle models in chapter 5.

2. Elastic constants for cracked media

Garbin and Knopoff (1973, 1975a,b) obtained expressions for the velocity variation of body-waves in an isotropic medium containing a weak concentration of dry or liquid-filled parallel penny-shaped cracks. These expressions are similar in form to the reduced equations (A3.2) above for the velocity variations in an anisotropic medium with sagittal symmetry. Crampin (1978) showed that it is possible to obtain a set of effective elastic constants for certain weakly anisotropic systems of aligned cracks by matching the constants A-G in (A3.2) with the corresponding terms obtained by Garbin and Knopoff. Non-uniqueness problems which were encountered by Crampin and Bamford (1977) in trying to obtain elastic constants to match observed Pn-wave velocity variations, do not appear when matching the Garbin and Knopoff expressions, since all three equations in (A3.2) are used. Elastic constants of a medium containing a mixture of dry and saturated cracks can be found in the same way as for mixtures of isotropic and anisotropic material, using equation (3.2.3).

Crampin et al.(1980) used the above techniques with some success in interpreting P-wave velocity variations observed by Bamford and Nunn (1979) in cracked limestone.